REFERENCE ONLY

UNIVERSITY OF LONDON THESIS

Degree PhD Year 2005 Name of Author LESLIE, D.E.

Positronium Beam Production and Scattering Cross-Sections

A thesis submitted to University College London for the degree of

Doctor of Philosophy

Dawn Elizabeth Leslie

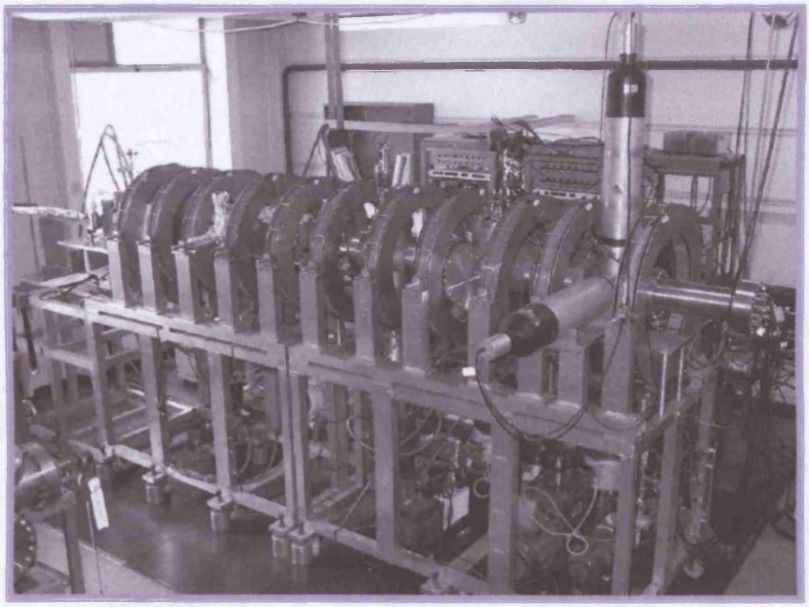

June 2005

ProQuest LLC
789 East Eisenhower Parkway
P.O. Box 1346
Ann Arbor, MI 48106-1346

Acknowledgments

There are many people I would like to thank for their support during my PhD studies at UCL. Firstly, I am indebted to my supervisor, Prof. Nella Laricchia, for her continuous support, understanding and encouragement. For their technical advice and expertise, I would like to thank Mr Ted Oldfield and Mr John Dumper, without whom many problems would have remained unresolved for much longer. I thank Dr Simon Armitage for introducing me to the workings and the idiosyncrasies of the positronium beam. To both Simon and Dr Marta Szłuińska, I would like to say how much I appreciate their friendship and assistance during my time in the positron group. I would also like to take this opportunity to thank my close friend Dugan for his intellectual distractions and for keeping me up to date with the world of astrophysics. Lastly, but by no means of least importance, I would like to express my thanks to my Mum and Dad for their unconditional love and support throughout my studies; to my brother for keeping me in touch with the outside world; and to Jason for his never-ending patience.

Abstract

In this work, the efficiency for the production of a monoenergetic positronium beam via the charge-exchange reaction of a positron beam in a gaseous target has been determined for molecular hydrogen and molecular nitrogen. In the case of molecular nitrogen, it has been found that the energy range over which a useful intensity of collimated positronium may be produced can be extended to 250eV, ~100eV higher than previously achieved. This should enable measurements of the total and partial positronium cross-sections at correspondingly higher energies, where target inelastic effects are expected to be significant.

A recent measurement of the integrated positronium formation cross-section for xenon found a larger yield of positronium atoms compared to the other noble gases. A shoulder was also seen ~10eV above the peak and it was suggested that this might be due to the production of positronium in an excited state. These findings have provided an incentive to investigate the collimated positronium production efficiency from xenon, which has been found to be surprisingly low. The quantum state of the beam atoms has also been found to be dominantly ground state. Possible reasons for these findings are discussed.

Total cross-sections for positronium-gas scattering have been extracted from the measurements of the positronium beam production efficiency for both molecular nitrogen and xenon. These quantities have also been determined directly by measuring the intensity of the positronium beam transmitted through a gas cell via the Beer-Lambert Law. A good consistency is found between the values obtained using this method and those determined indirectly.

Recently, measurements have been made of the absolute integrated cross-section for the fragmentation of positronium in collision with helium atoms, along with the longitudinal energy distributions of the residual positrons in the energy range E_{Ps}=13-33eV. Measurements of the latter indicate a peak close to half the residual positronium energy, suggesting that they continue to move in a correlated fashion with the emitted electrons. In the present work, these results have been confirmed using a different method, which enables the energy range of investigation to be extended both to higher and lower values. Preliminary results have also been obtained at E_{Ps}=60eV for the ejected positrons and for the ejected electrons at E_{Ps}=33eV.

Contents

Figure Captions

Chapter 1

Figure 1.1 One of the cloud chamber photographs which revealed the existence of the positron.

Figure 1.2 Feynman diagrams of one, two, three and four photon decay modes.

Figure 1.3 Energy spectrum of photons emitted from ortho-Ps annihilation.

Figure 1.4 Comparison of the energy level diagrams for hydrogen and positronium.

Figure 1.5 Decay mode of ^{22}Na.

Figure 1.6 Energy distribution of positrons emitted from a ^{58}Co source and a W(110) moderator.

Figure 1.7 Simplified illustration of the interaction of positrons at a metal surface (from Mills, 1983).

Figure 1.8 The single-particle potential for a thermalised positron near a metal surface. V_{corr} is due to correlation with the conduction electrons and V_0 is due to the ion cores.

Figure 1.9 Configuration of the source and moderator.

Figure 1.10 Schematic illustration of the behaviour of the e^+-He and e^--He total scattering cross-section.

Figure 1.11 Energy dependence of the relative contributions from Ps^* to the total positronium formation cross-section.

Figure 1.12 Scaled positronium formation cross-section $\sigma_{Ps}/(\sigma_{Ps})_{max}$ versus E/E_{th} for the noble gases. Here E_{th} is the positronium formation threshold energy.

Figure 1.13 Positronium formation cross-section for xenon. A comparison is shown between the data of Marler *et al* (2005) [● and —] and those of Laricchia *et al* (2002) [--□--].

Chapter 2

Chapter 3

Chapter 4

Chapter 5

Figure 5.4 An example of positron measurements with gas in the production cell: a) detailed measurements; b) larger energy range and step.

Figure 5.5 An example of positron measurements with gas in both cells: a) detailed measurements; b) larger energy range and step.

Figure 5.6 An example of the net signal from residual positrons in the case of both a) detailed and b) coarse energy step measurements.

Figure 5.7 Results of $\left(\frac{dN_+(E_+)}{dE_+}\right)^c$ for E_{Ps}=18, 33 and 60eV.

Figure 5.8 Summary of the net positron signals shown previously in Figure 5.6.

Figure 5.9 Experimentally determined values of the positronium-helium total cross-section along with the corresponding calculation of Blackwood *et al* (1999).

Figure 5.10 Geometry of the scattering cell and graphical representation of the fraction of positronium atoms which survive in-flight annihilation from the centre of the production cell to the detector.

Figure 5.11 Experimentally determined values of the detection efficiency of CEMA2 to positrons and positronium atoms versus incident energy (Armitage, 2002).

Figure 5.12 Experimental and theoretical values of the break-up cross-section of positronium in collision with helium atoms: experimental values obtained by detection of positrons.

Figure 5.13 Experimentally and theoretically determined values of the absolute differential cross-sections of positrons ejected from the break-up of 18, 33 and 60eV positronium.

Figure 5.14 Investigation of the electron background.

Figure 5.15 Schematic and photographic representations of the developed RFA.

Figure 5.16 Potentials applied to electrostatic elements during electron measurements.

Figure 5.17 An example of electron measurements with gas in the production cell: a) detailed measurements; b) larger energy range and step.

Figure 5.18 An example of electron measurements with gas in both cells: a) detailed measurements; b) larger energy range and step.

Figure 5.19 An example of the net electron signal obtained from a) detailed and b) coarse measurements.

Figure 5.20 Net electron signal from detailed and coarse energy step measurements.

Figure 5.21 Experimental and theoretical values of the break-up cross-section of positronium in collision with helium atoms: red data points obtained from positron detection; blue data point obtained from electron detection.

Figure 5.22 Results of $\left(\frac{dN_{-}(E_{-})}{dE_{-}}\right)^{c}$ for E_{Ps}=33eV.

Figure 5.23 Energy distribution of electrons from 33eV positronium in collision with helium. Experimental data have been scaled to allow shape comparison.

Figure 5.24 Comparison of energy distributions of residual positrons and electrons for E_{Ps}=33eV.

Table Captions

Chapter 1

Chapter 3

Chapter 5

Chapter 1
Introduction

1.1 Historical Background

An investigation of cosmic radiation by Anderson (1932a and b, 1933) provided the first experimental evidence of pair production and of the existence of the positron (e^+), the antimatter counterpart of the electron (e^-). Anderson's experimental apparatus comprised a cloud chamber containing a thin lead plate placed in a magnetic field. Whilst surveying the cosmic radiation, he observed tracks such as those shown in Figure 1.1. From the investigation of these tracks, it was concluded that they were due to particles with charge equal to the electronic charge but of opposite sign. Blackett and Occhialini (1933) confirmed that the charge-to-mass ratio of the positron is of the same order of magnitude as that of the electron, as predicted by Weyl (1931).

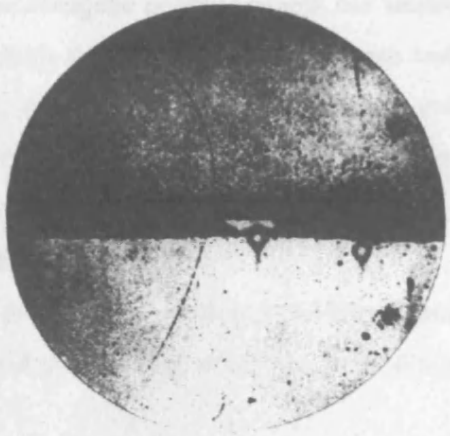

Figure 1.1 One of the cloud chamber photographs which revealed the existence of the positron.

The primary importance of Anderson's experiment was the confirmation of a theory by Dirac (1930a) which, through the negative energy solutions to the relativistic wave equation describing the motion of electrons in free space, predicted the existence of the positron. In his 'hole theory' Dirac proposed that the vacuum be considered as an infinite sea of electrons occupying negative energy levels (from $-m_0c^2$ to $-\infty$) in accordance with the Pauli Exclusion Principle. If an electron from the 'negative energy sea' were excited to a positive energy level, it would leave a hole behind, which would act just like a positively charged electron with a positive energy.

The existence of a bound state of a positron and an electron, called positronium (Ps), was first predicted by Mohorovicic (1934). The structure of positronium was described quantum mechanically by Ruark (1945) and calculations of its binding energy and lifetimes were reported by Wheeler (1946). The first observation of positronium was made by Deutsch (1951) through the measurement of the lifetime of positrons in gases.

Since then, positron and positronium physics has become relevant across a number of branches of science. For example, in astronomy and astrophysics, the radiation from positron-

electron annihilation is an important probe of energetic events in our Galaxy providing unique information about the region from which it emanates (Kinzer *et al*, 2001; Fatuzzo *et al*, 2000; Leventhal, 1992); in condensed matter physics, positrons may be used as a non-destructive bulk and surface probe of materials, especially in the detection of structural defects (for a review see Schultz and Lynn, 1988; Coleman, 2002); and in medicine, positron emission tomography (PET) has become a well-established diagnostic technique (Ott, 2003; Czernin and Phelps, 2002). In atomic physics, the development of monoenergetic positron beams has allowed the acquisition of collision data which by comparison with those for electrons, protons and anti-protons provide information on the effects that mass and charge-sign have on collision dynamics (Knudsen and Reading, 1992). The recent production of positronium beams has paved the way for direct measurements of positronium cross-sections in collisions with atoms and molecules (Garner *et al*, 1996; Armitage *et al*, 2002).

In the following sections, the fundamental properties of positrons and positronium are discussed along with recent studies of positron and positronium scattering from atoms and molecules.

1.2 Fundamental Properties of Positrons and Positronium

1.2.1 Positrons

The positron has the same mass and spin as the electron but its charge (and, thus, magnetic moment) is of opposite sign. A positron is stable in vacuum, with a lifetime in excess of 2×10^{22} years (Bellotti *et al*, 1983). Upon encountering an electron, it may annihilate resulting in the production of gamma-ray photons. Energy conservation dictates that the total energy of the emitted photons must equal the rest mass energy, i.e. 1.022MeV, plus any kinetic energy of the annihilating pair. The charge parity, P_C, of the annihilating system must also be conserved. For a system of n photons:

$$P_C = (-1)^n \qquad 1.1$$

and for an electron-positron system:

$$P_C = (-1)^{L+S}, \qquad 1.2$$

where L is the total orbital angular momentum of the system and S is its total spin (Yang, 1950). Thus, through annihilation an odd or even number of photons is released depending on the total angular momentum of the positron-electron pair.

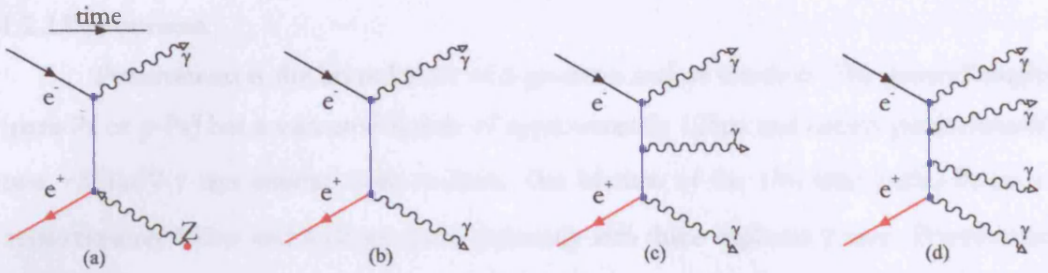

Figure 1.2 Feynman diagrams of one, two, three and four photon decay modes.

The lowest order Feynman diagrams for positron-electron annihilation into one, two, three and four γ-rays are shown in Figure 1.2. The cross-section for a given decay mode is directly proportional to α^m, where α is the fine structure constant, given by:

$$\alpha = \frac{e^2}{2\varepsilon_0 hc} \sim \frac{1}{137} \qquad 1.3$$

and m is the number of vertices in the corresponding Feynman diagram. This renders the two photon decay mode shown in Figure 1.2(b) the most likely, since (a) additionally requires the presence of a third body, Z, in order to conserve momentum and (c) and (d) have three and four vertices, respectively. Each of the decay modes in Figure 1.2 have been first observed by: a) Palathingal *et al* (1991); b) Klemperer *et al* (1934); c) Chang *et al* (1982, 1985); and d) Adachi *et al* (1990).

The cross-section for annihilation of a positron with an electron resulting in the emission of two photons, was given by Dirac (1930b) as:

$$\sigma_{2\gamma} = \frac{\pi r_0^{\,2} c}{v}, \qquad 1.4$$

where c is the speed of light, v, the velocity of the positron with respect to the electron and r_0 is the classical electron radius, given by:

$$r_0 = \frac{e^2}{4\pi\varepsilon_0 m_0 c^2}. \qquad 1.5$$

In the case of positron annihilation in a gas of number density n, equation 1.4 is usually modified according to:

$$\sigma_{2\gamma} = \frac{\pi r_0^{\,2} c n Z_{eff}}{v}, \qquad 1.6$$

where Z_{eff} is the number of electrons per atom or molecule available for annihilation (e.g. Heyland *et al*, 1982). Even at positron energies of millielectronvolts, this quantity is of the order of 10^{-26}m^2 (Bransden, 1969) and direct annihilation is, therefore, usually expected to be negligible compared to other atomic processes.

1.2.2 Positronium

Positronium is the bound state of a positron and an electron. The ground singlet-state (para-Ps or p-Ps) has a vacuum lifetime of approximately 125ps and decays predominantly into two ~511keV γ-rays emitted back-to-back. The lifetime of the 1^3S_1 state (ortho-Ps or o-Ps) is approximately 142ns and it decays predominantly into three coplanar γ-rays. Positronium with total spin S and angular momentum L annihilates into n gamma-rays according to equations 1.1 and 1.2, which yield:

$$(-1)^n = (-1)^{L+S}. \qquad 1.7$$

From spin statistics, positronium is formed in a ratio of ortho- to para- of 3:1, leading to the more abundant occurrence of three photons upon annihilation of ground-state positronium. The characteristics of the two spin states of ground-state positronium are given in Table 1.1.

Name	State	Sub-state	Ground-state decay rates (μs^{-1})		No. and energy of annihilation quanta
			Experiment	Theory	
p-Ps	1^1S_0	m=0	7990.9 ± 1.7 [a]	7989.5 [b]	2 × 511 keV
o-Ps	1^3S_1	m=0, ±1	7.0398 ± 0.0029 [c]	7.0420 [d]	3, 0-511keV

Table 1.1 Ground-state positronium properties ([a]Al-Ramadhan and Gidley, 1994; [b]Khriplovich and Yelkhovsky, 1990; [c] Asai *et al*, 1995; [d] Adkins *et al*, 1992).

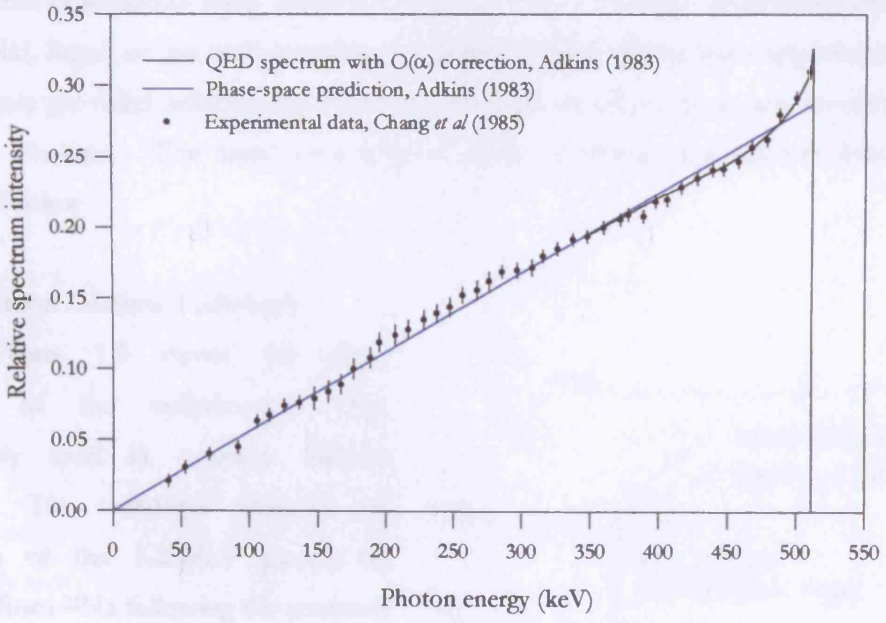

Figure 1.3 Energy spectrum of photons emitted from ortho-Ps annihilation.

In Figure 1.3, the continuous energy distribution of gamma-rays arising from ortho-Ps is shown for the calculations of Adkins (1983) and the experimental measurements of Chang *et al* (1985), with which good agreement is found.

Positronium is structurally hydrogen-like but, with half the reduced mass, its energy levels are decreased by a factor of two (e.g. the binding energy of ground state positronium is 6.8eV) and the Bohr radius is doubled. The energy levels of hydrogen and positronium (Fulton and Martin, 1954) are compared in Figure 1.4.

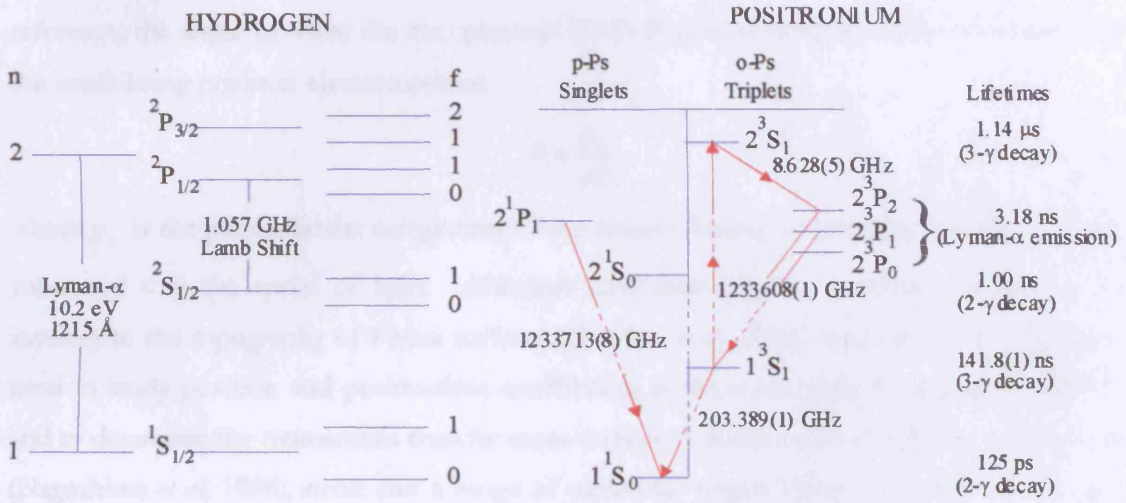

Figure 1.4 Comparison of the energy level diagrams for hydrogen and positronium.

1.3 Early Experiments

The earliest experiments using positrons involved incorporating a positron-emitting isotope into a solid, liquid or gas and detecting the gamma-rays resulting from annihilation. These experiments provided information about the interactions of positrons and positronium with the host medium. The basic principles of three common experimental techniques are described below.

1.3.1 Positron Lifetime Technique

Figure 1.5 shows the decay scheme of the radioisotope ^{22}Na, commonly used in positron lifetime studies. The technique employs the detection of the 1.28MeV gamma-ray released from ^{22}Na following the emission of β^+ particles, in delayed coincidence with an annihilation photon (Shearer and

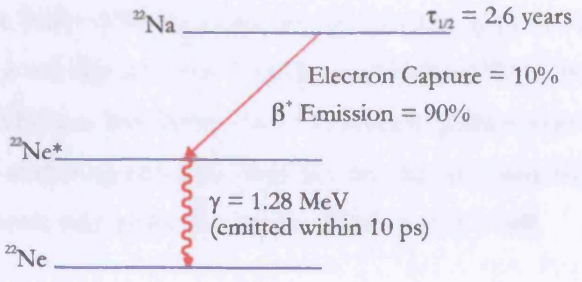

Figure 1.5 Decay mode of ^{22}Na.

Deutsch, 1949). This allows the investigation of positronium formation and quenching, positron and positronium thermalisation (see Charlton, 1985).

1.3.2 ACAR

ACAR (Angular Correlation of Annihilation Radiation) measures the angular deviation from co-linearity of the two gamma-rays released following positron annihilation, an effect documented by DeBenedetti *et al* (1949). Positrons in a sample thermalise quickly and annihilate with an electron, emitting two back-to-back photons. In the laboratory frame of reference, the angle between the two photons ($180°$-θ) gives a measure of the momentum of the annihilating positron-electron pair as:

$$\theta \approx \frac{p_{\perp}}{mc}, \qquad 1.8$$

where $p_{\perp}$ is the perpendicular component of the centre-of-mass momentum, m is the positron mass and c is the speed of light. Although used primarily in condensed matter, e.g. to investigate the topography of Fermi surfaces (Dugdale *et al*, 1994), the method has also been used to study positron and positronium annihilation in the noble gases (Coleman *et al*, 1994) and to determine the momentum transfer cross-section of positronium in collision with helium (Nagashima *et al*, 1998), neon and a range of molecular targets (Saito *et al*, 2003) at energies below the positronium fragmentation threshold.

1.3.3 Doppler Broadening

Whilst the gamma-rays released from annihilation of a positron-electron pair at rest each have an energy of 511keV, a Doppler shift in their energies will arise due to any motion of the centre-of-mass of the annihilating system. This energy shift, ΔE, is given by:

$$\Delta E = mcv_{cm}\cos\phi, \qquad 1.9$$

where v_{cm} is the speed of the centre-of-mass of the positron-electron pair and ϕ is the angle between the direction of motion of the centre-of-mass and that of one of the gamma-rays. The Doppler Broadening technique yields the momentum distribution of the annihilating pair and is often used in the study of lattice defects, as a freely diffusing positron can become trapped in the region of minimum potential created by a missing ion core (Schultz and Lynn, 1988). In addition to this, the Doppler broadening technique has been used to measure positronium thermalisation rates and to determine elastic scattering cross-sections for momentum transfer for positronium collisions with a variety of atomic and molecular targets (Skalsey *et al*, 1998).

1.4 Slow Positron Beam Development

Fast positrons (β^+ particles) may be obtained from the nuclear decay of radioactive isotopes (e.g. ^{58}Co, ^{22}Na, ^{64}Cu, ^{68}Ge, ^{11}C; for their properties see Dupasquier and Zecca, 1985) or from pair production at particle accelerators. As depicted in Figure 1.6 for ^{58}Co, positrons are emitted with a large intrinsic energy distribution, which restricts their use in controlled experimentation. However, as also shown in Figure 1.6, moderation allows a compression of phase space and a higher yield of slow positrons (E~few eV) over that which would be velocity selected from the initial β^+ spectrum. This slowing down process, which results in the emission of positrons with a few eV of energy, is described briefly below.

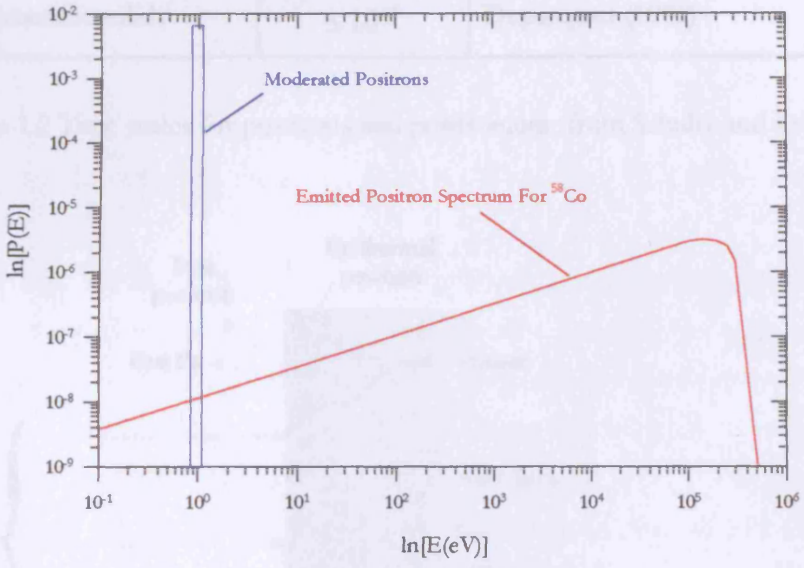

Figure 1.6 Energy distribution of positrons emitted from a ^{58}Co source and a W(110) moderator.

A fast positron, implanted into a solid, loses energy primarily via inelastic collisions until it reaches a state of thermal equilibrium. The implantation depth of β^+ particles in a defect free metallic solid is approximately 0.1mm, compared to the diffusion length of approximately 1000Å for a thermalised positron. Once thermalised, the de Broglie wavelength of the positron (~60Å) is greater than the inter-atomic distance and, therefore, the positron behaves like a propagating wave in a solid. Typical positron timescales for various processes are outlined in Table 1.2 and the likely fates of positrons that have diffused to a metal surface are represented in Figure 1.7. An incident positron, implanted into a solid, may return to the surface as a thermal or epithermal positron or, alternatively, it may annihilate within the bulk of the metal. Thermal positrons that are ejected from a metal surface may contribute to the slow positron beam. The ratio of the number of slow positrons emitted from the surface to the number of fast positrons incident on the moderator is defined as the moderation efficiency.

Process	Time (s)	References
Thermalization	$\sim 10^{-12}$	Perkins and Carbotte (1970)
Trapping (specific rate per atom)	$\sim 10^{-15}$	Hodges (1970)
Positron lifetime		
Freely diffusing	$\sim 1\times10^{-10}$	West (1973)
Monovacancy trapped	$\sim 2\times10^{-10}$	West (1973)
Multivacancy trapped	$\sim 4\times10^{-10}$	Hautojärvi (1979)
Surface state	$\sim 4-6\times10^{-10}$	Lynn *et al* (1984), Kögel *et al* (1988)
Ps lifetimes		
Triplet, in non-metallic solids	$\leq 10^{-9}$	Dupasquier (1981)

Table 1.2 Time scales for positrons and positronium (from Schultz and Lynn, 1988).

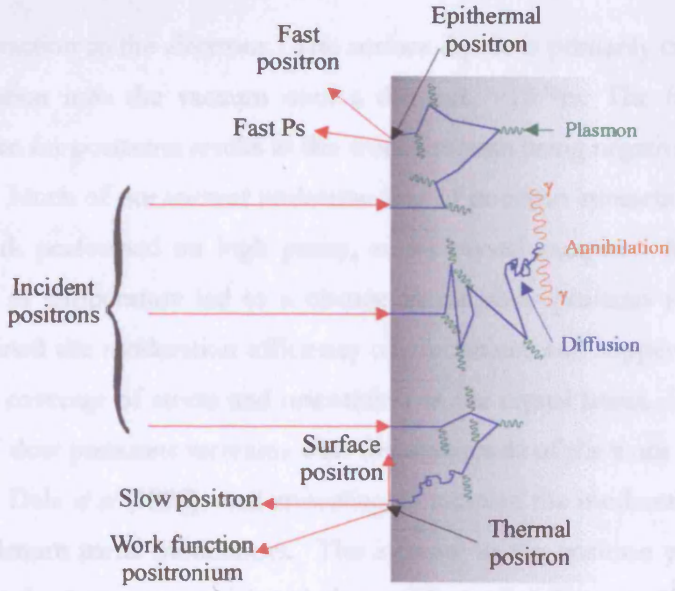

Figure 1.7 Simplified illustration of the interaction of positrons at a metal surface (from Mills, 1983).

In Figure 1.8, a one-dimensional representation of the single-particle potential energy for a positron near a metal surface is shown for the case of a negative positron work function, ϕ_+. In this case, the emission of the thermal positron from a solid into a vacuum is energetically permitted. The work function of a certain surface can be written as $\phi_+ = -\Delta\varphi - \mu_+$ (Tong, 1972), where the contributing factors are the bulk chemical potential, μ_+, and the surface dipole, $\Delta\varphi$. The chemical potential includes repulsion from the ion cores

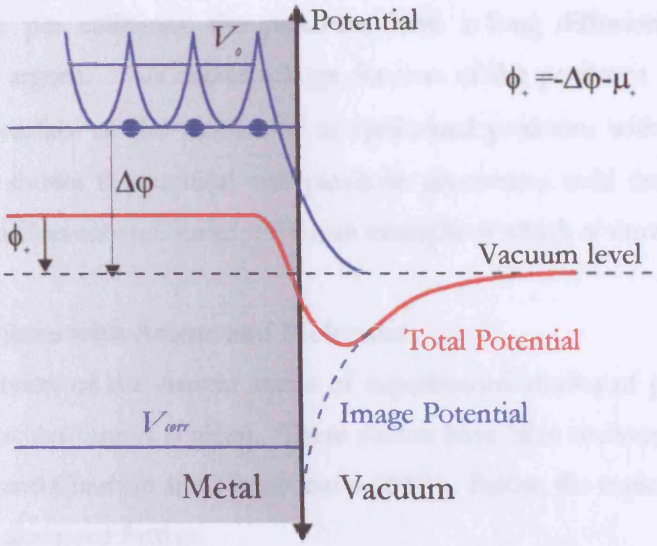

Figure 1.8 The single-particle potential for a thermalised positron near a metal surface. V_{corr} is due to correlation with the conduction electrons and V_0 is due to the ion cores.

and attraction to the electrons. The surface dipole is primarily caused by tailing of the electron distribution into the vacuum over a distance ~10^{-10}m. The fact that the surface dipole is attractive for positrons results in the work function being negative for certain materials.

Much of our current understanding of positron interactions with solids was initiated by the work performed on high purity, single crystal samples. Mills *et al* (1978) found that a change in temperature led to a change in the slow positron yield. Murray and Mills (1980) determined the moderation efficiency of aluminium and copper as a function of temperature, surface coverage of atoms and orientation of the crystal lattice. Their results indicated that the yield of slow positrons increases with the magnitude of the work function.

Dale *et al* (1980) used annealing to increase the moderation efficiency of tungsten and molybdenum metal moderators. The increase in the positron yield was attributed to the fact that the heat treatment reduced the number of defects in the lattice, which tend to trap positrons and, thus, allowed more positrons to diffuse back to the surface.

Gullikson and Mills (1986) determined that wide band gap insulators, namely rare gas solids (RGS), would produce efficient positron moderators. As below the band gap energy, the only mechanism for positron energy loss is phonon excitation (which removes only a

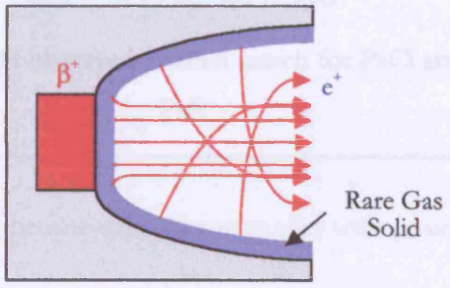

Figure 1.9 Configuration of the source and moderator.

few millielectronvolts per collision), the positrons have a long diffusion length in these materials (5000Å for argon). This allows a large fraction of the positrons emitted from the source to reach the surface of the moderator as epithermal positrons with $E>\phi_+$ (1.7eV in argon). It has been shown that conical and parabolic geometries yield the best efficiencies (Khatri *et al*, 1990 and Greaves and Surko, 1996), an example of which is shown in Figure 1.9.

1.5 Positron Interactions with Atoms and Molecules

In Table 1.3, an overview of the current status of experimental studies of positron collisions with atomic and molecular targets is given. These studies have been recently reviewed by, e.g. Laricchia *et al* (2003) and Charlton and Humberston (2001). Below, the topics most relevant to the present work are discussed further.

Interaction	Experimental status
Total cross-section	σ_T for many atomic and molecular targets including
$e^+ + A \rightarrow all$	H, He, alkali and Mg.
Elastic scattering	Some σ_{el} and $d\sigma_{el}/d\Omega$.
$e^+ + A \rightarrow e^+ + A$	
Positronium formation	σ_{Ps} for $1 < E < 100eV$
$e^+ + A \rightarrow Ps + (m-1)e^- + A^{m+}$	including H, alkali, Mg ; some $d\sigma_{Ps}/d\Omega$.
Target excitation	First state-resolved σ_{ex} for electronic and
$e^+ + A \rightarrow e^+ + A^*$	vibrational excitations.
Direct ionization	σ_i^{z+} for $1 < E < 1000eV$
$e^+ + A \rightarrow e^+ + me^- + A^{m+}$	including H, some $d\sigma_i^+/d\Omega$, $d^2\sigma_i^+/d\Omega_1 dE_i$ and first $d^3\sigma_i^+/d\Omega_1 d\Omega_2 dE_i$.
Annihilation	Energy-resolved measurements for Ar, Xe and a
$e^+ + A \rightarrow 2\gamma + A^+$	variety of molecular targets.
Formation of compounds	Only PsH observed – failed search for PsCl and
$e^+ + A \rightarrow (PsC) + D^+$	PsF.

Table 1.3 Status of experimental collision studies with positrons.

Total cross-sections for positron scattering from atoms and molecules have been studied extensively (e.g. Kauppila and Stein, 1990). The noble gases were investigated initially (Kauppila *et al*, 1976 and 1981; Stein *et al*, 1978; Dababneh *et al*, 1980) due to their existence in atomic form at room temperature. The work was extended to include alkali metals (Stein *et al*, 1987; Kwan *et al*, 1989), atomic hydrogen (Zhou *et al*, 1997) as well as simple and complex molecules (e.g. Hoffman *et al*, 1982; Sueoka and Mori, 1986). Marked differences in the total cross-section, σ_T, from positron and electron impact are often apparent, as in the case of helium, see Figure 1.10. Here, it can be seen that the cross-section for the electron scattering is larger than that for the positron at low energies, due to partial cancellation of the polarisation and the static Coulomb interaction and a smaller impact parameter in the case of the latter. Similar behaviour is found for the other noble gases, although the electron total cross-sections for argon, krypton and xenon show narrow minima at energies below 1eV, where only elastic scattering occurs. The minima in the electron case were first observed by Ramsauer (1921, 1923), Townsend and Bailey (1922) and Ramsauer and Kollath (1929) and referred to as Ramsauer-Townsend effects. They arise from quantum mechanical effects associated with an attractive polarization interaction between the incident projectile and the target atom, whereby the s-wave shift passes through π radians (or its multiple). In the case of positron scattering, the Ramsauer-Townsend minima exist for helium, neon and possibly argon between 1-3eV, however they are due to the s-wave phase shift going through zero value at such low energies. In the case of krypton and xenon, this effect is calculated to appear at greater energies but higher partial waves mask it (Raith, 1997).

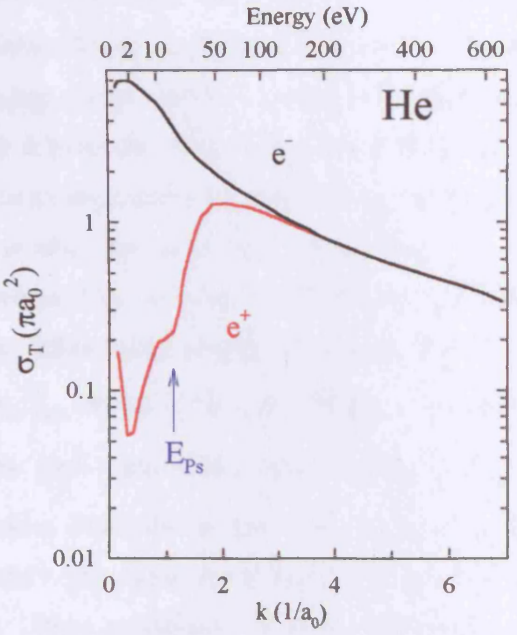

Figure 1.10 Schematic illustration of the behaviour of the e^+-He and e^--He total scattering cross-section.

In general, σ_T^+ reveals a pronounced increase at the positronium formation threshold, E_{Ps}, (indicated by a blue arrow in Figure 1.10) reflecting the significant role of this process in the positron scattering by inert atoms. As the impact energy is increased, the dominance of the static interaction ultimately should lead to merging of total cross-sections for the two projectiles, as illustrated in Figure 1.10 for positron-helium scattering where merging occurs at

around 200eV.

Although various partial cross-sections, as outlined in Table 1.3, provide a wealth of information on the interactions of positrons with atoms and molecules, the process of the utmost relevance in this work is positronium formation. Recently, Laricchia *et al* (2002) measured the energy dependence of total ionisation cross-sections from neon, argon, krypton and xenon by positron impact from threshold to ~1keV. From these data, positronium formation cross-sections were extracted by subtracting the direct ionisation- from the total ionisation cross-sections. A conspicuous feature of the results of Laricchia *et al* (2002) is a double-peak structure in the positronium formation cross-sections for argon, krypton and xenon. The first peaks appear at roughly twice the threshold energy for ground state positronium formation. The maxima of the second peaks appear roughly at twice the value of the threshold energy for excited-state positronium (Ps*) formation and led to the conjecture that they might be due to the formation of Ps*. Prompted by these results, the lower and upper limits for the contribution of the Ps* for these targets were estimated by Laricchia *et al* (2002) and are shown in Figure 1.11. The evaluation of the upper limits followed the finding of Szłuińska *et al* (2002), as shown in Figure 1.12, that plots of $\sigma_{Ps}/(\sigma_{Ps})_{max}$ versus E/E_{th} broadly yield a common curve for a variety of targets ($(\sigma_{Ps})_{max}$ being the peak value of the cross-section and E_{th}, in this case, is the ground-state positronium formation threshold energy). The results presented in Figure 1.11 suggest that the Ps* might occur much more abundantly than previously thought (Van Reeth *et al*, 2000; Humberston *et al*, 2001). More specifically for xenon, the fraction of positronium formed in the excited state is estimated to be (100±13)% and (50±15)% for upper and lower limit, respectively, at 40eV.

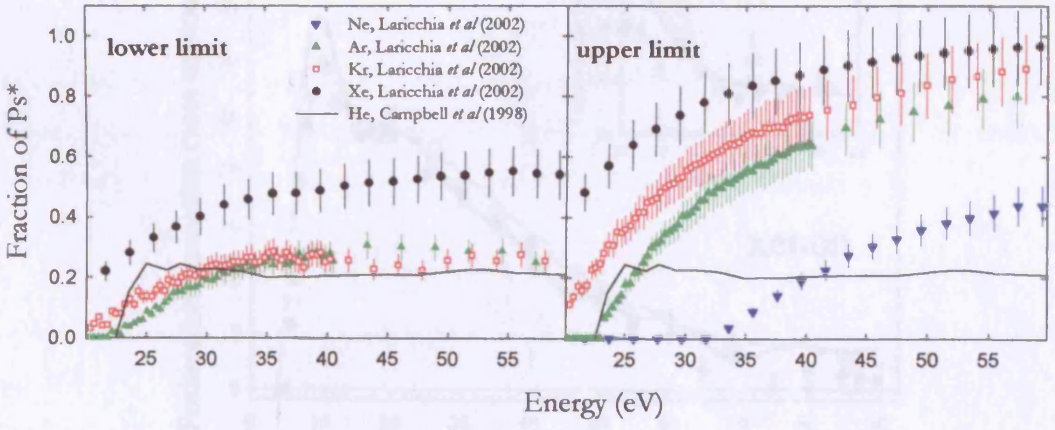

Figure 1.11 Energy dependence of the relative contributions from Ps* to the total positronium formation cross-section.

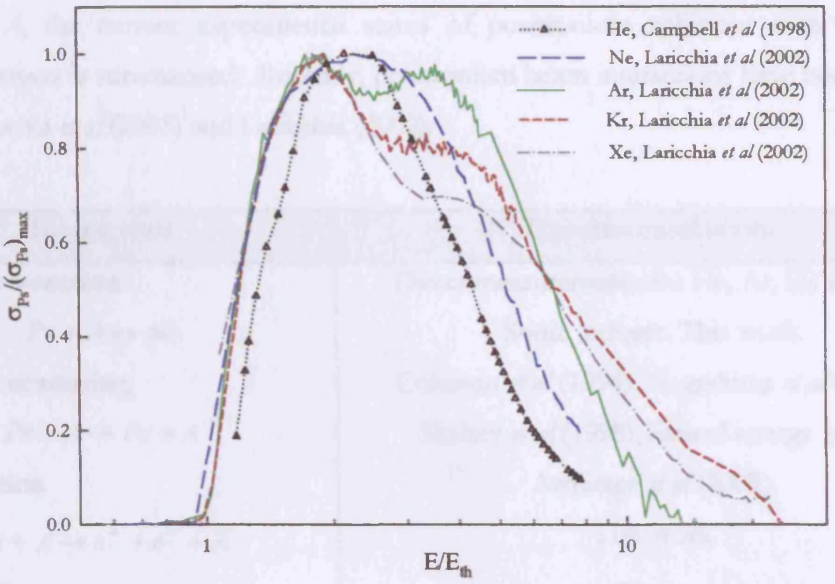

Figure 1.12 Scaled positronium formation cross-section $\sigma_{Ps}/(\sigma_{Ps})_{max}$ versus E/E_{th} for the noble gases. Here E_{th} is the positronium formation threshold energy.

Recently, Marler *et al* (2005) have reported absolute measurements of the positronium formation cross-sections for the noble gases up to 90eV. They employed a trap-based positron beam in conjunction with a frozen neon moderator. In comparison to the results of Laricchia *et al* (2002), discrepancies exist in the results for argon and krypton at higher energies, where Marler *et al* (2005) do not observe the double peak structure. However, there is fair agreement in the positronium formation cross-sections for xenon, as shown in Figure 1.13.

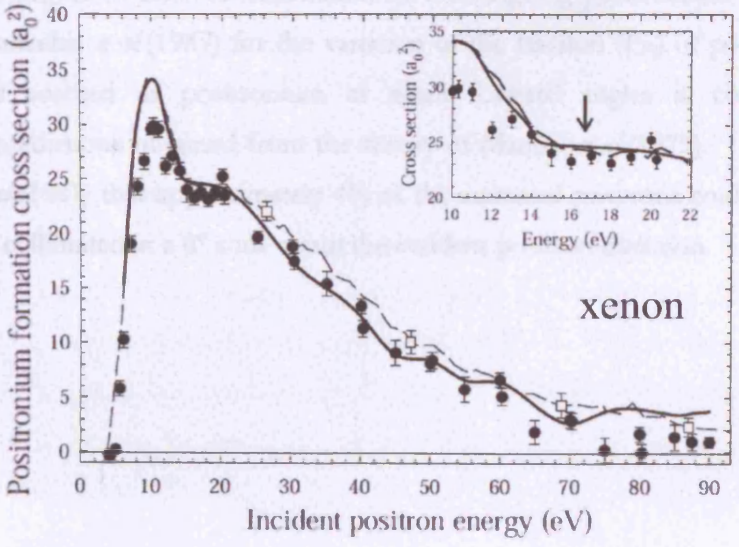

Figure 1.13 Positronium formation cross-section for xenon. A comparison is shown between the data of Marler *et al* (2005) [● and —] and those of Laricchia *et al* (2002) [--□--].

1.6 Positronium Interactions

In Table 1.4, the current experimental status of positronium collisions with atomic and molecular targets is summarised. Recently, positronium beam interactions have been reviewed, e.g. by Laricchia *et al* (2003) and Laricchia (2002).

Interaction	Experimental status
Total cross-section	Direct measurements for He, Ar, H_2 and O_2.
$Ps + A \rightarrow all$	Some indirect. This work.
Ps elastic scattering	Coleman *et al* (1994), Nagashima *et al* (1998),
$Ps + A \rightarrow Ps + A$	Skalsey *et al* (1998), limited energy range.
Ps ionisation	Armitage *et al* (2002).
$Ps + A \rightarrow e^+ + e^- + A$	This work.
Ps excitation	None.
$Ps + A \rightarrow Ps^* + A$	

Table 1.4 Experimental status on some of the processes available in positronium collisions with atoms and molecules.

1.6.1 Positronium Beam Production

Early developments in positronium beam production were reviewed by Laricchia (1993). More specifically, the prospect of producing a positronium beam emerged from the first experimental investigations of $d\sigma_{Ps}/d\Omega$. These were stimulated by theories, which indicated a high degree of forward collimation of the outgoing positronium. In Figure 1.14, the results of Laricchia *et al* (1987) for the variation of the fraction (F_{Ps}) of positrons scattered by helium and emitted as positronium at small forward angles is compared to the corresponding predictions obtained from the theory of Mandal *et al* (1979). It was concluded by Laricchia *et al* (1987) that approximately 4% of the scattered positrons could be detected as ortho-Ps atoms collimated in a 6° cone about the incident positron direction.

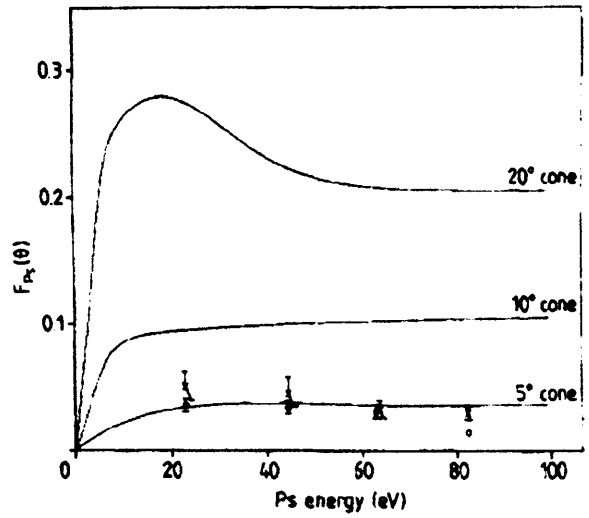

Figure 1.14 Fraction $F_{Ps}(\theta)$ of positrons scattered by helium and emitted as positronium within 5, 10 and 20° angular ranges about the incident positron direction. Experimental points – Laricchia *et al* (1987); theory – Mandal *et al* (1979).

A beam of positronium atoms can be formed via the charge-exchange reaction of a positron beam in a suitable gaseous target, given by:

$$e^+ + A \rightarrow Ps + A^+, \qquad 1.10$$

where the positron captures an electron from the target gas, A. The positronium beam production efficiency, ε_{Ps}, is defined as the number of positronium atoms produced per incident positron per steradian in accordance with:

$$\varepsilon_{Ps} = \frac{N_{Ps}}{\Omega N_+} D, \qquad 1.11$$

where N_{Ps} and N_+ are the number of positronium atoms and incident positrons, respectively, D accounts for the in-flight decay of positronium atoms before the detector and Ω takes into account the detection solid angle.

An investigation into the production efficiency of a positronium beam from argon, helium and molecular hydrogen gaseous targets was made by Garner *et al* (1996), who found that H_2 is the most efficient converter gas at an energy of 30eV. The results from the study of Garner *et al* (1996) are shown as a 3D plot in Figure 1.15. At 90eV, the three gases give similar results. At 120eV, argon becomes the most efficient gas for collimated positronium production by ~40%.

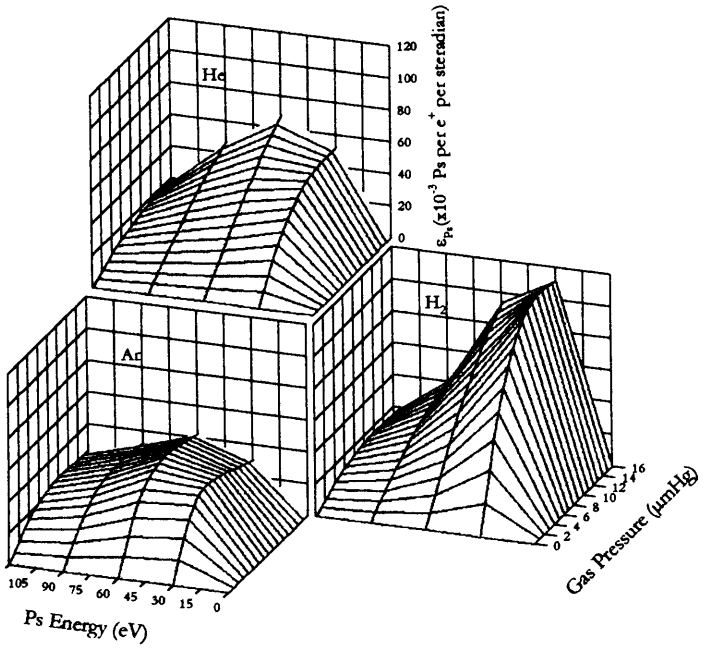

Figure 1.15 Positronium-beam production efficiency measurements of Garner *et al* (1996).

Figure 1.15 indicates that, as the pressure of the target gas increases, the production efficiency saturates (Zafar *et al*, 1991; Laricchia and Zafar, 1992) due to competition between positronium formation and subsequent scattering of positronium from the target gas. The positronium beam production efficiency depends on the differential positronium formation cross-section, $d\sigma_{Ps}/d\Omega$, and the total cross-sections, σ_T, for both positron and positronium scattering, as discussed further in chapter 3.

1.6.2 Total cross-sections for positronium scattering from atoms and molecules

Garner *et al* (1996) determined the total cross-sections, σ_T^{Ps}, for positronium in collision with argon, helium and H_2 through beam attenuation measurements using the Beer-Lambert law:

$$\sigma_T^{Ps} = \frac{kT}{pL}\left(\frac{I_0}{I}\right), \qquad 1.12$$

where I_0 (I) is the net incident (transmitted) flux of positronium atoms, k is the Boltzmann constant, p is the target gas pressure, L is the effective length of the scattering cell and T is the ambient temperature.

Figure 1.16 shows the results of σ_T^{Ps} for argon, molecular hydrogen and helium (Garner *et al*, 1996) where it can be seen that all targets show a similar trend: an increase to a broad maximum followed by a slow decrease with increasing energy. Included in the figures are the cross-section values extrapolated to zero detection angle, so as to account for the effect

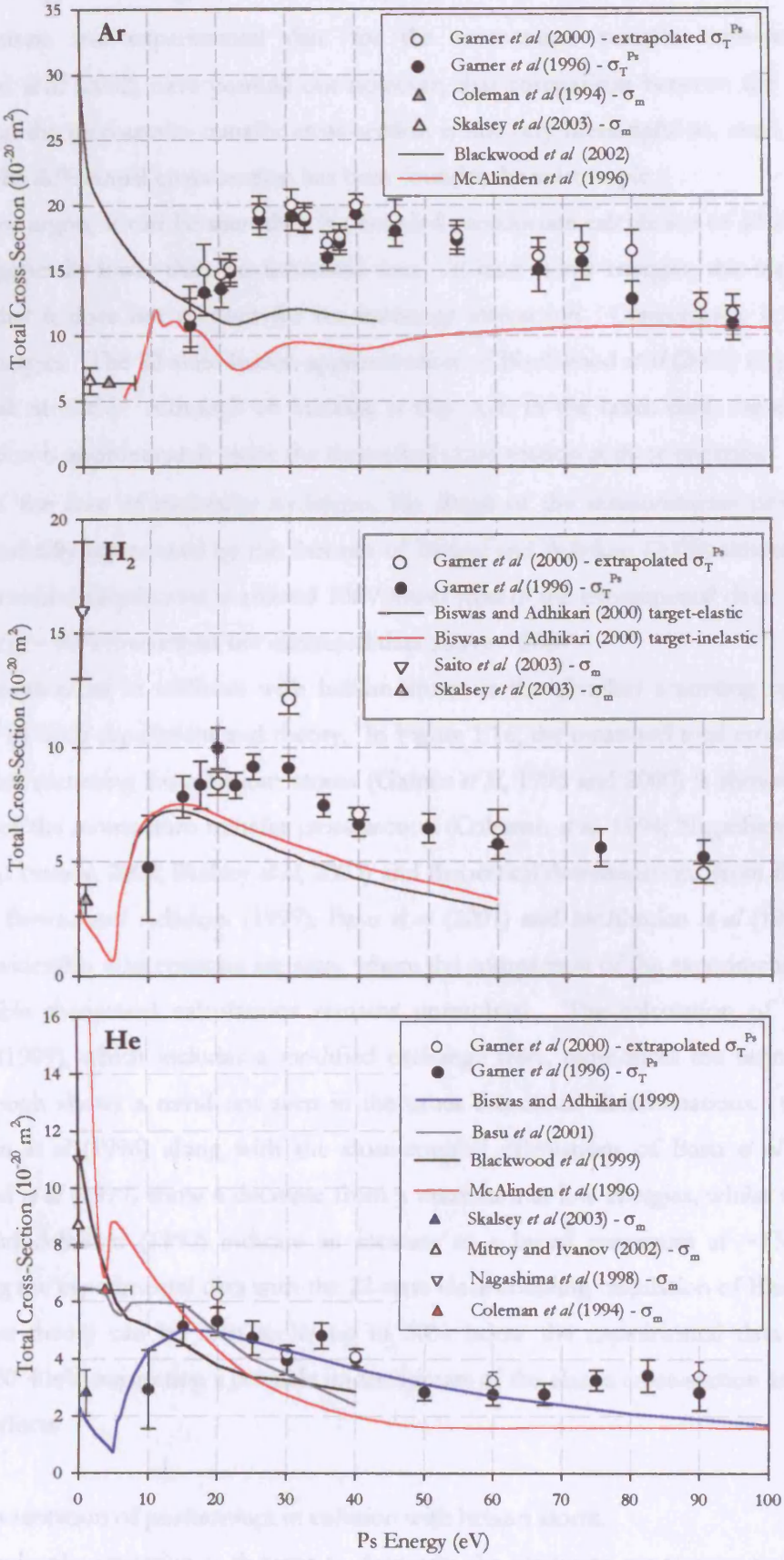

Figure 1.16 Available experimental and theoretical data for the total cross-section of positronium in collision with various targets.

of forward angle scattering, by Garner *et al* (2000). Also shown are the relevant theoretical determinations and experimental data for the momentum transfer cross-section (σ_m). Blackwood *et al* (2002) have pointed out however, that comparison between the total cross-section and the momentum transfer cross-section is not very meaningful as, even at very low energies, the differential cross-section has been found to be anisotropic.

For argon, it can be seen that the coupled pseudostate calculation of McAlinden *et al* (1996) is generally lower than the measured data. At least at low energies, this may be due to the fact that it does not account for the exchange interaction. Convergence is seen at the highest energies. The 22-state frozen approximation of Blackwood *et al* (2002) displays a small broad peak at 32eV. Although an increase is also seen in the beam data, the experimental cross-section is approximately twice the theoretical cross-section at these energies.

In the case of molecular hydrogen, the shape of the measurements of Garner *et al* (1996) is broadly reproduced by the theories of Biswas and Adhikari (2000) although the peak in the theoretical calculations is around 10eV lower than in the experimental data. Once again the theory is ~50% lower than the measured data above ~30eV.

Positronium in collision with helium atoms is the simplest scattering system to be addressed by both experiment and theory. In Figure 1.16, the measured total cross-section for positronium scattering from helium atoms (Garner *et al*, 1996 and 2000) is shown along with estimates of the momentum transfer cross-section (Coleman *et al*, 1994; Nagashima *et al*, 1998; Mitroy and Ivanov, 2002; Skalsey *et al*, 2003) and theoretical determinations from Blackwood *et al* (1999), Biswas and Adhikari (1999), Basu *et al* (2001) and McAlinden *et al* (1996). Below 10eV, considerable discrepancies are seen, where the comparison of the experimental data with the available theoretical calculations remains unresolved. The calculation of Biswas and Adhikari (1999), which includes a modified exchange term, reproduces the beam data fairly well, although shows a trend not seen in the other theoretical determinations: the work of McAlinden *et al* (1996) along with the close-coupled calculations of Basu *et al* (2001) and Blackwood *et al* (1999) show a decrease from a maximum at low energies, whilst the result of Biswas and Adhikari (1999) indicate an increase to a broad maximum at ~15eV. When comparing the experimental data with the 22-state close-coupling calculation of Blackwood *et al* (1999), the theory can be seen to lie up to 30% below the experimental data at energies between 20-40eV, suggesting a possible underestimate of the elastic cross-section and/or target inelastic effects.

1.6.3 Fragmentation of positronium in collision with helium atoms

Projectile ionisation is thought to dominate the scattering processes occurring in the Ps-He collision system at intermediate energies (Biswas and Adhikari, 1999; Blackwood *et al*,

1999). The process has been observed in collisions of positronium with helium atoms by Armitage *et al* (2002), where its cross-section and the longitudinal energy distributions of the residual positrons have been measured. These results are shown in Figure 1.17, where the limits on the experimental data arise from the uncertainty in the detection efficiency of positrons and positronium (Armitage, 2002). Corresponding theories are also shown in the figure. The theoretical determination of Biswas and Adhikari (1999), made using the Born approximation, and the classical trajectory Monte Carlo (CTMC) calculation of Sarkadi (2003) both lie above the experimental data: the former by a factor of ~2; and the latter by a factor of ~1.6. The Coulomb-Born approximation used by Ray (2002) produces results below the measured values, which are instead broadly in agreement with the close-coupled calculation of Blackwood *et al* (1999).

The longitudinal energy spreads for the residual positrons (Armitage *et al*, 2002) are shown in Figure 1.18. There, the energy distributions for the residual positrons can be seen to peak at a value just below half the residual energy E_r, where $E_r=E_{Ps}-B$, with E_{Ps} being the positronium kinetic energy and B, its binding energy of 6.8eV. Such a peak indicates that the residual particles each have an energy of approximately half the residual energy ($E_r/2$) and are emitted at a small angle with respect to the beam axis. This implies that the positron and electron remain strongly correlated in the final state in an analogous manner to the Electron

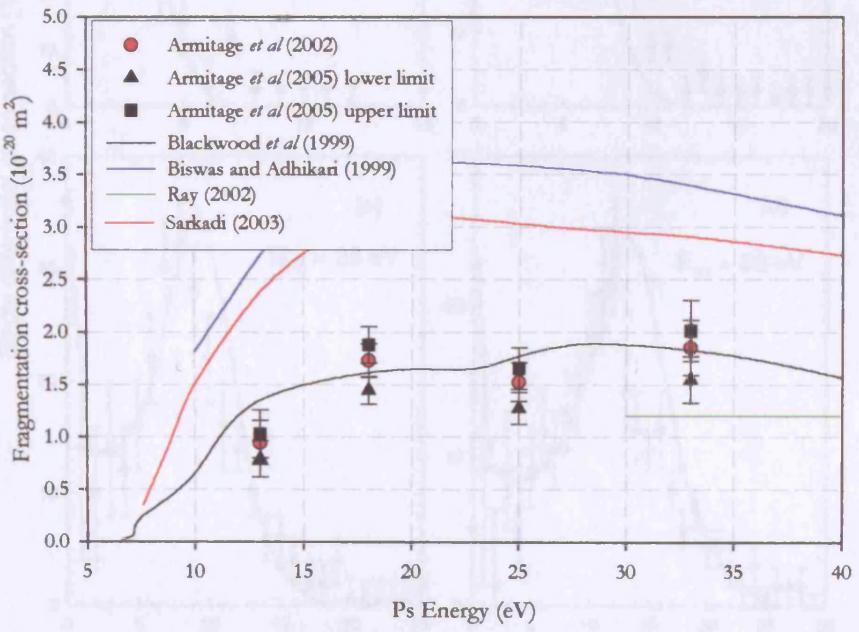

Figure 1.17 Experimentally and theoretically determined cross-section for the fragmentation of positronium in collision with helium atoms: experimental data (Armitage *et al*, 2002) are shown with upper and lower limits.

Loss to the Continuum in atom-atom collisions, where the ejected electron has a low relative velocity with respect to the scattered projectile.

Sarkadi (2003) treated the fragmentation of positronium in collision with helium atoms using a three-dimensional, three-body version of the CTMC method. As shown in Figure 1.18, following normalisation, the calculations reproduce fairly well the longitudinal energy distributions measured by Armitage *et al* (2002). Sarkadi (2003) normalised the experimental data to his CTMC cross-sections to emphasise the agreement between experiment and theory on the width and asymmetry of the peak, including the trend at lower energies for the peak to become less prominent. The shift in the peak energy from $E_r/2$ is explained by Armitage *et al* (2002) as arising from the confinement of the residual positrons in the guiding magnetic field, whereby any finite angular distribution would result in the measured energy distribution being

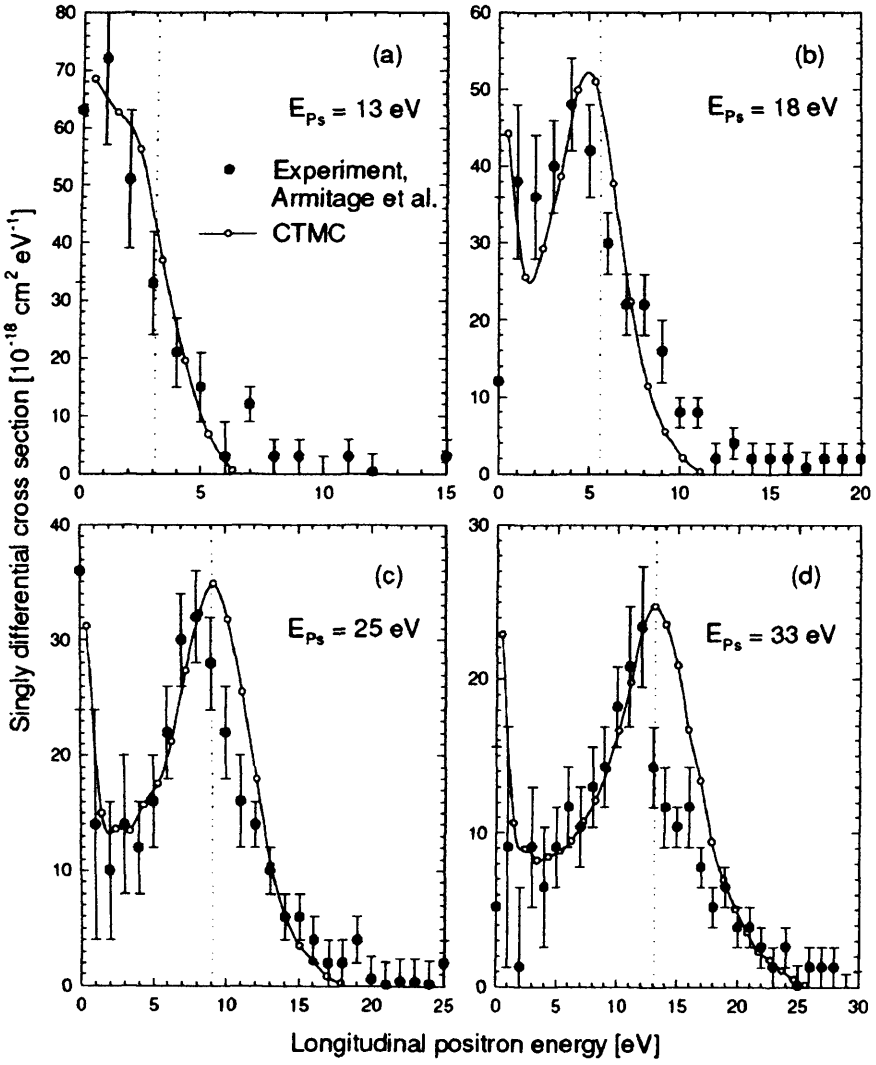

Figure 1.18 Longitudinal energy distributions of positrons released from the break-up of positronium in collision with helium atoms. Experimental data of Armitage *et al*, 2002 (full circles) are normalised to CTMC calculations of Sarkadi, 2003 (hollow circles) [Figure taken from Sarkadi (2003)].

shifted to lower energies and becoming broadened. Armitage *et al* (2002) determined that the break-up positrons are released within an angle of less than 20° with respect to the beam axis across the energy range, in good agreement with the theoretical determination of Sarkadi (2003).

In addition to the longitudinal energy distribution of the positrons, Sarkadi (2003) extended the calculation to include the energy distribution of the residual electrons: the two are compared in Figure 1.19 for positronium energies of 18eV and 33eV. The energy distributions of the residual electrons exhibit a less pronounced peak, shifted with respect to the peak in the positron spectra. The enhancement of the low energy spectrum in the case of the electrons is attributed (Sarkadi, 2003) to electron emission at angles around 90°, which would render the longitudinal energy of those electrons close to zero. These differences become less pronounced as the positronium energy increases from 18 to 33eV and it is suggested by Sarkadi (2003) that increasing the energy further would result in a decrease in the variation.

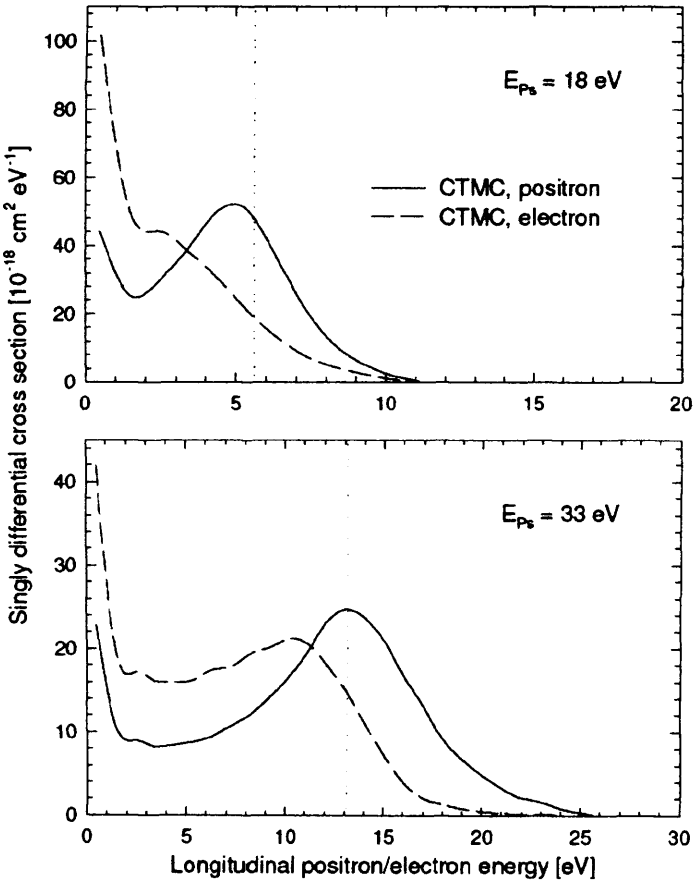

Figure 1.19 Calculations of the longitudinal energy distributions of positron (solid line) and electron (dashed line) ejected in Ps-He collisions. Vertical dotted lines indicate $E_s/2$ [Figure taken from Sarkadi (2003)].

1.7 Motivation for the Present Work

The study of Garner *et al* (1996) determined molecular hydrogen to be the most efficient gas for the conversion of a positron- to positronium-beam at 30eV. In this work, investigations are extended to include molecular nitrogen, in order to determine whether this larger diatomic molecule can provide a better convertor gas over a broader energy range. The positronium total cross-section has also been determined for this target. Following the work of Laricchia *et al* (2002), the positronium production efficiency from xenon is also investigated and the dominant quantum state of the beam determined in order to identify possible production of positronium in an excited state. In addition, the total cross-section for positronium scattering from this target is examined.

Following the work of Armitage *et al* (2002) and Sarkadi (2003), it would be desirable to extend the measurements of the fragmentation cross-section to higher energies and above the threshold for target ionisation. For this purpose, an alternative method based on a simple retarding field analyser is developed and employed in this work. The performance of this method is initially checked by comparison with the previous data and measurements are extended to 60eV. Following measurements of the differential- and integrated break-up cross-section by positron detection, a preliminary investigation into the detection of the corresponding ejected electrons is also presented.

Chapter 2

Experimental Arrangement and Detection Systems

2.1 Overview

This chapter contains a discussion of the experimental apparatus and the methods used in the production of a positron beam and its conversion to a monoenergetic beam of positronium atoms. The positronium beam used for this study was initially designed by Zafar *et al* (1991) and developed by Garner (1997), Özen (2000) and Armitage (2002) prior to the work described in this thesis.

Figure 2.1 shows a schematic diagram of the apparatus. The arrangement can be separated into two parts: the source region and the experimental region, the two being separated by a pneumatic valve. The first section contains the source of positrons, a radioactive isotope of sodium (^{22}Na). The decay of ^{22}Na produces fast β^+ particles, with a branching ratio of 90%, which are thermalised using a solid argon moderator and accelerated to the required energy by applying a voltage directly to the source, positive with respect to the chamber earth. The positron beam is then guided in a magnetic field produced by eleven Helmholtz coils and separated from high energy particles (gamma-rays and fast β^+ and e^-) emanating from the source and moderator region by a Wien filter.

In the second section, the positron beam enters the first (production) gas-cell, where positronium is produced via charge-exchange of positrons and the target gas. The second (scattering) gas-cell contains the gas under investigation in scattering studies, for example measurements of positronium total cross-sections. A retarding potential arrangement lies between the two cells to reflect residual positrons exiting the production cell. Another such arrangement is placed after the scattering cell, before the detectors, in order to reflect positrons arising from the possible break-up of positronium.

A number of different detection methods were used in this study. Time-of-flight measurements were performed using two channel electron multiplier arrays (CEMA); a tagger (CEMA1), which incorporates a positron remoderator and is situated before the production cell, and the end of beamline detector (CEMA2). Coincidences between these two detectors enable the measurement of the energy distributions of the positron and positronium beams. The other detection systems use a gamma-ray detector (CsI or NaI) in coincidence with CEMA2. These methods require no remoderation of the positron beam, thus allowing the full intensity of the beam to be used. A detailed discussion of the apparatus and detection systems mentioned above follows.

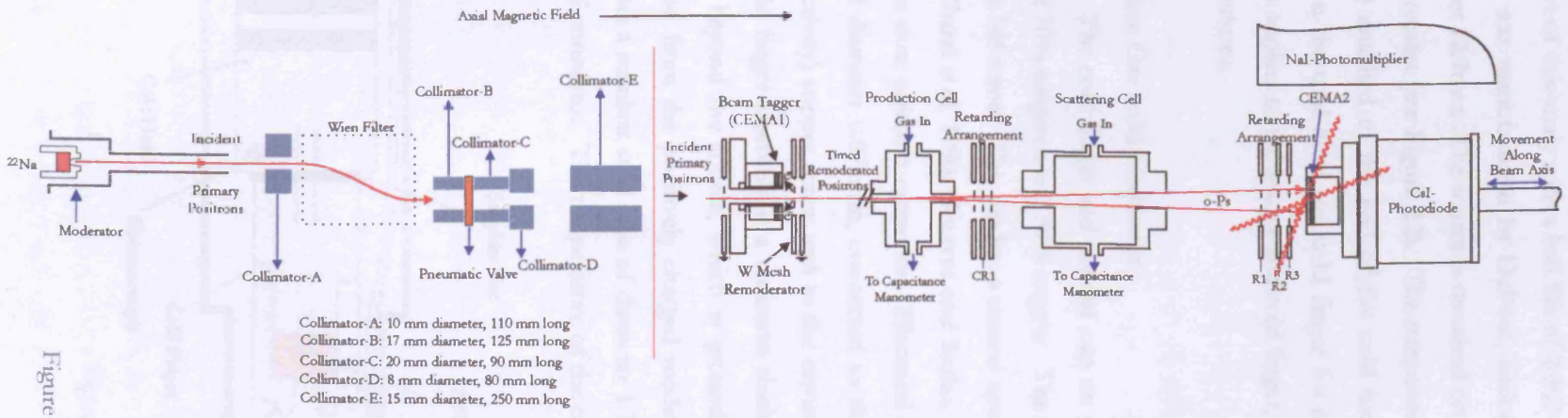

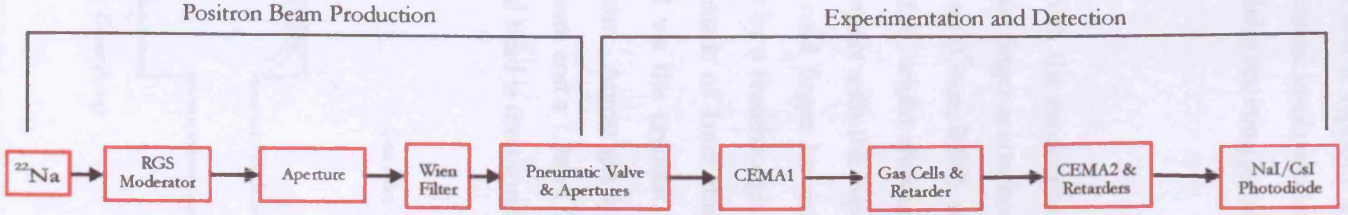

Figure 2.1 Schematic diagram of the positronium beamline.

2.2 Positron Beam Production

2.2.1 Positron Source

The source of positrons is a radioactive isotope of sodium (^{22}Na) of activity 77.6mCi at the start of this study with a half life of 2.602 years, thus decaying to 38.8mCi by the end. The source was manufactured by DuPont, enclosed in a titanium capsule of height 9.7mm and diameter 12.7mm. The source is mounted on the cold finger of the head of a two stage closed-cycle cryostat (see Figure 2.2). The temperature is monitored using a thermocouple (Cr-AuFe 0.07%) attached to the end of the cold head and a sapphire disc of diameter 0.5mm lies between the cold head and cold finger for electrical insulation, such that a non-zero voltage may be applied to the source and cold finger, whilst retaining good thermal conductivity at low temperatures.

2.2.2 Rare Gas Solid Moderator

The cold finger and conical cup on which the moderators are grown are made of an alloy of 70% tungsten and 30% copper. The cold finger is attached to the cold head by a glass-ceramic M6 screw. The cup has a conical aperture (Özen, 2000), which provides a large surface area (Khatri *et al*, 1990; Greaves and Surko, 1996), whilst allowing penetration of the electric field for slow positron extraction. Electrical contact with the cup is maintained via a tungsten wire of diameter 0.075mm, connected to the cold finger by an OFHC (Oxygen Free High Conductivity) copper screw and to the cryostat by a feedthrough. Surrounding the cold head and cold finger assembly is a radiation shield made of 1mm thick OFHC copper, extending 90mm beyond the source, which is grounded via the cryostat such that positrons may be extracted from the positively charged moderator. Argon gas is admitted into the radiation shield via a stainless steel pipe of diameter 1.75mm and a 1.3mm OFHC Cu pipe, separated by a PTFE connector. The temperature of the cold head is monitored via a Lakeshore controller.

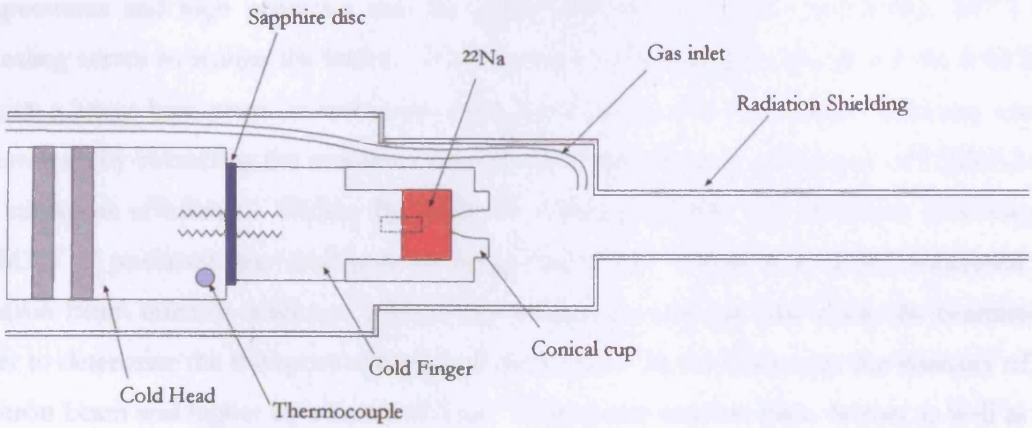

Figure 2.2 Schematic of the cold head and cold finger.

Rare gas solid (RGS) moderators have been found to be the most efficient positron moderators (Gullikson and Mills, 1986). In particular, neon has been found to produce the most efficient moderator by a factor of ~5 with respect to argon, krypton and xenon (Mills and Gullikson, 1986), however, we are currently unable to reach a low enough temperature or impurity concentration in our system to grow a neon RGS moderator. Ultra high vacuum conditions are required to grow an RGS moderator (Petkov *et al*, 1997). In order to achieve this, the system was baked to a temperature of 350K to achieve a base pressure of the order of 1×10^{-9} Torr. The gas line was then flushed to reduce impurities further, prior to the cryostat being turned on. At a temperature of ~7K, argon gas was admitted into the system to a pressure of ~2×10^{-6} Torr in the source chamber, equivalent to 2×10^{-8} Torr in the **E×B** chamber (in the region of the Wien Filter, Figure 2.1). The pressure was determined using the ion gauge and corrected for the gas being used by:

$$P(true) = P(measured)/K, \qquad 2.1$$

where K is the normalisation constant for the gas, which in the case of argon, is 1.4. From this, an estimate of the pressure, P, inside the heatshield was obtained from:

$$P = P(true)\left(\frac{S}{C}+1\right), \qquad 2.2$$

where S is the pumping speed of the system ($65ls^{-1}$) and C, the conductance between the source and **E×B** chambers and through the heatshield ($2.36ls^{-1}$).

Figure 2.3 shows a plot of typical moderator growth at T=7K and P(**E×B**)=2×10^{-8} Torr. The number of slow positrons, monitored with a multichannel scaler, increases with the moderator thickness until saturation, at which point the gas line is shut. Following this, a further increase in the positron beam is seen as fewer slow positrons are attenuated by residual gas in the chamber. The moderator is then annealed by turning the cryostat off until the temperature reaches ~35K. At this point, it is turned back on again. Crystals grown at low temperatures and high pressures may be highly defective (Venables and Smith, 1977) and annealing serves to realign the lattice. It also removes residual argon frozen on the cold head to give a lower base pressure and more stable moderators. The moderation efficiency can be determined by correcting the number of positrons for the detection efficiency of CEMA2 and the transport efficiency. Within the work of Armitage (2002), the detection efficiency of CEMA2 to positrons was evaluated as being 0.46±0.01. Özen *et al* (2000) measured the positron beam intensity with and without the collimators and gas cells along the beamline in order to determine the transport efficiency of the system. In the latter case, the intensity of the positron beam was higher by a factor of four. Taking into account these factors as well as the number of disintegrations per second of the radioactive source, the moderation efficiency can be calculated. This is shown in Figure 2.3b.

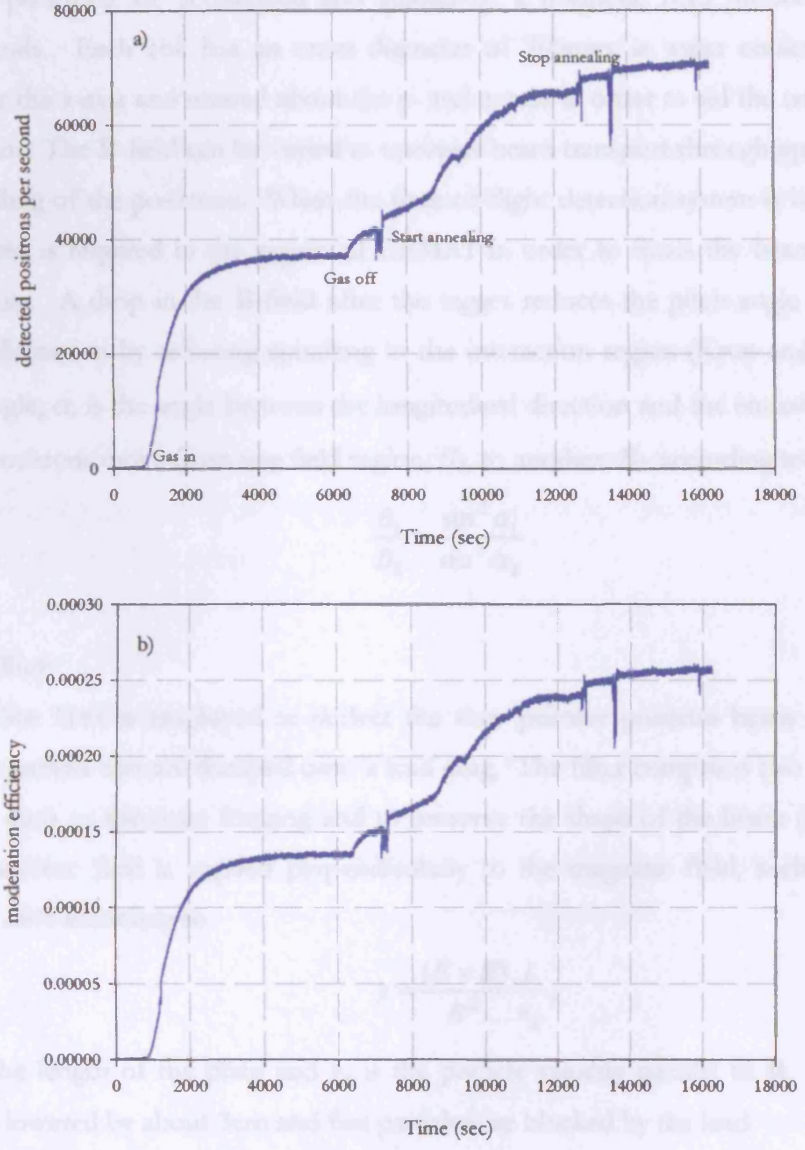

Figure 2.3 Example of a growth curve for an argon gas solid moderator.

Epithermal positron emission from RGS moderators results in a relatively wide positron energy spread (Gullikson and Mills, 1986). When the positron energy falls below the positronium formation threshold (in solid argon, E_{th}=9.95±0.05eV), the energy loss is dominated by phonon emission. The energy of the emitted positron lies between E_{th} and zero, depending on the implantation depth and phonon emission rate. As the moderator becomes thicker, the epithermal contribution decreases due to the effective increase in implantation depth. As a result, the emitted positrons have a narrower energy spread, suggesting a reduction in the epithermal contribution, as explained by Armitage (2002).

2.3 Positron Beam Transport

2.3.1 Magnetic Field

The positrons are accelerated and guided by a magnetic field produced by eleven Helmholtz coils. Each coil has an outer diameter of 700mm, is water cooled and can be moved about the x-axis and rotated about the y- and z-axes in order to aid the transport of the positron beam. The **B**-field can be varied to optimise beam transport through apertures and to reduce spiralling of the positrons. When the time-of-flight detection system is being used, the highest **B**-field is required in the region of CEMA1 in order to focus the beam through the tagger aperture. A drop in the **B**-field after the tagger reduces the pitch angle and serves to achieve parallelisation by reducing spiralling in the interaction region (Kruit and Read, 1983). The pitch angle, α, is the angle between the longitudinal direction and the emission vector and changes as positrons move from one field region, B_1, to another, B_2, according to:

$$\frac{B_1}{B_2} = \frac{\sin^2 \alpha_1}{\sin^2 \alpha_2}. \qquad 2.3$$

2.3.2 Wien Filter

A Wien filter is employed to deflect the slow primary positron beam such that fast particles and gamma rays are dumped onto a lead plug. The filter comprises two curved plates, flared at the ends to minimise fringing and to preserve the shape of the beam (Hutchins *et al*, 1986). An electric field is applied perpendicularly to the magnetic field, such that charged particles will drift according to:

$$y = \frac{(E \times B)}{B^2} \frac{L}{v_x}, \qquad 2.4$$

where L is the length of the plate and v_x is the particle velocity parallel to **B**. The positron beam is thus lowered by about 3cm and fast particles are blocked by the lead.

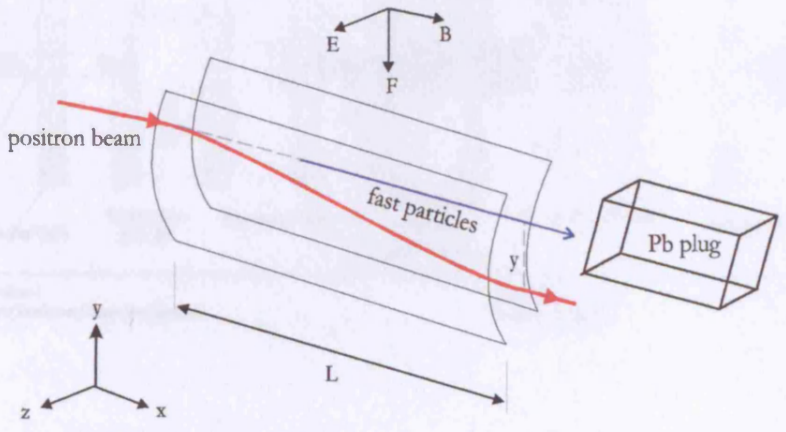

Figure 2.4 Schematic of the Wien Filter.

2.4 Vacuum System

The two halves of the experimental apparatus are pumped by different methods and will be described in turn.

2.4.1 Source Region

The vacuum on the source side is achieved via two turbo pumps connected perpendicularly to the vacuum chamber (see Figure 2.5). An Edwards turbo drag pump (EXT 70H) is connected to the source chamber and a Varian turbo pump (V550) to the **E×B** chamber. These pumps are water cooled and both are backed by an Edwards two stage rotary pump (E2M28). The backing line pressure is monitored using a Pirani gauge. For safety purposes, the backing pump may be isolated using a magnetic or manual valve in the case of vacuum or power failure. An ion gauge is situated in each chamber to monitor the pressure. The source region is separated from the experimental region by a pneumatic valve in order to isolate the two halves of the system.

2.4.2 Experimental Region

On the experimental side, four water cooled oil diffusion pumps are used (see Figure 2.5). Two are backed by an Edwards E2M40 rotary pump and the others by a Varian SD300 and a Varian DS 202 rotary pump, respectively. Between each diffusion pump and its backing pump lies a Pirani gauge to monitor the pressure in the backing line, and a magnetic valve and isolation taps such that the backing pump may be isolated if required.

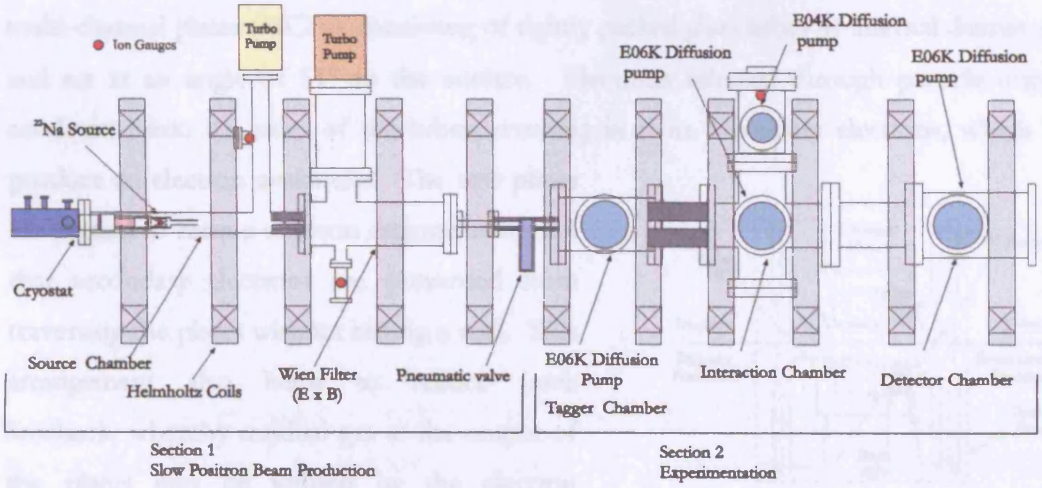

Figure 2.5 The positronium beam vacuum system.

2.5 Vacuum System Protection

In order to prevent damage to the system due to water or electrical failure, a number of protection systems are in place. The diffusion pumps, coils, turbo pumps, cryostat and coils are cooled by six water circuits. Each has a flowtrol which relies on water pressure to maintain a closed circuit, such that a decrease in water pressure leads to a loss of connection and, thus, causes the circuit to trip. The pneumatic valve then closes to isolate the two halves of the experiment and the power to the diffusion pumps, turbo pumps, coils and high voltages is lost. The magnetic valves close to isolate the backing pumps and prevent backstreaming from the diffusion pumps. Further protection systems are in place, which rely on the pressure in the backing lines in the case of a pump failure, a leak in the vacuum chamber or an uncontrolled influx of gas. The trip level for the pressure in the backing lines is set to 6×10^{-2} Torr. An additional protection circuit exists, which prevents the cryostat being powered if the water pressure and vacuum are unsatisfactory.

2.6 Experimental Region

2.6.1 CEMA1

The experimental region comprises two internal detectors. The first (CEMA1 shown in Figure 2.6) uses a remoderation technique (Laricchia *et al*, 1988) such that secondary electrons, produced when the positrons strike a tungsten remoderator, are detected by CEMA1. The remoderator comprises four annealed tungsten meshes, each of 90% transmission, which are positively biased with respect to the earth grid and allow the energy of the remoderated positrons to be set. The electrons are extracted using a suitable electric field between the remoderator and the front of the channel plates. The array comprises two impedance matched multi-channel plates (MCPs), consisting of tightly packed glass tubes of internal diameter 25μm and set at an angle of 51° to the surface. Electrons released through particle impact are accelerated into the sides of the tubes, resulting in more secondary electrons, which in turn produce an electron avalanche. The two plates are aligned to form a chevron arrangement such that secondary electrons are prevented from traversing the plates without hitting a wall. This arrangement also helps to reduce ionic feedback, whereby residual gas at the output of the plates may be ionised by the electron avalanche. The ion may travel back through the plates, releasing more secondary electrons, which give rise to spurious signals. At the end

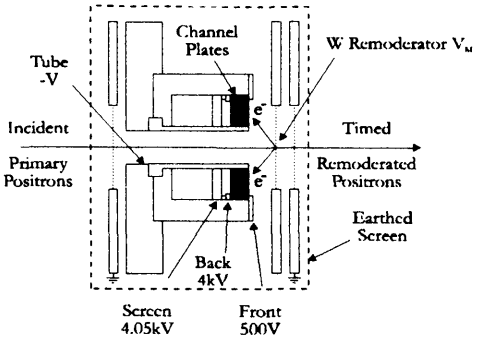

Figure 2.6 Schematic of CEMA1.

of the MCP, the electrons are drawn onto a brass disc (the screen) and the pulse from the screen is fed into various electronics, as discussed in §2.7.1.

CEMA1 is situated on a manipulator arm to allow movement in the linear and rotational directions. This enables the detector arrangement to be orientated for the maximum count rate and also the removal of the detector when not in use. The entire assembly is surrounded by an earth grid in order to minimise stray electric fields.

2.6.2 Gas Cells

Two gas cells are utilised in the experimental arrangement, both made of aluminium cylinders. Whilst the apertures on the production cell are brass, those on the scattering cell are made of lead. Gas inlets are attached to external gas cylinders with intermediate needle valves and the internal pressure is monitored via external capacitance manometers (Chell MK7893). A retarding arrangement between the two cells allows any residual positrons from the production cell to be stopped by applying a positive potential. The positronium scattering cell used initially in this study was designed by Armitage (2002) during the study of the fragmentation of positronium in collision with helium atoms, such that residual positrons (from the break-up of positronium) of energy up to 100eV and emittance angle of 90° would not be intercepted by the exit aperture.

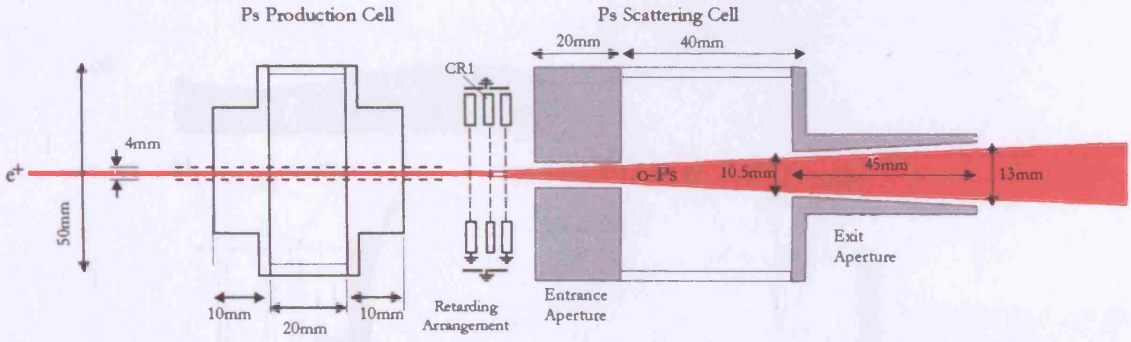

Figure 2.7 Schematic of the gas cells.

2.6.3 CEMA2

CEMA2 (see Figure 2.8) lies after the gas cells and is used to detect both positrons and positronium atoms. This detector comprises two plates similar to those in CEMA1 but without the central hole. A retarding arrangement is positioned in front of the detector (see Figure 2.8) such that a potential may be applied to stop positrons as required. R1 is grounded when detecting the incident positron beam and positrons from the fragmentation of positronium (Armitage *et al*, 2002) and is positively biased to detect positronium, so as to repel

residual positrons. R2 and R3 are used to return secondary electrons emitted from the surface of CEMA2 and, thereby, increase the detection efficiency. The entire array is surrounded by an earth shield and mounted on a linear manipulator such that the positronium flight length may be varied. Pulses from CEMA2 are sent to external electronics, as discussed in §2.7.2.

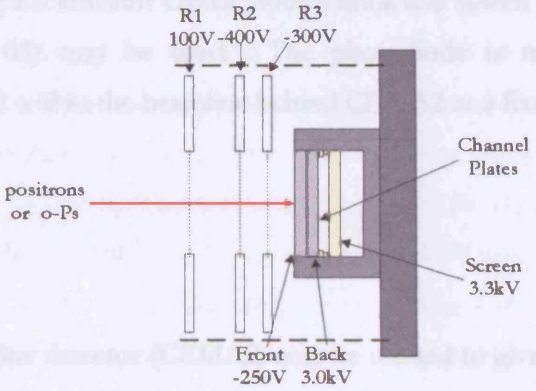

Figure 2.8 Schematic of CEMA2.

2.6.4 Gamma-ray detectors

A NaI detector is used to register gamma-rays from positron annihilation and in this way, coincidence measurements may be achieved between a positron incident on CEMA2 and one of its annihilation photons. This detector comprises a scintillator crystal (150mm diameter, 80mm width) coupled to a photomultiplier tube, which has a potential difference of ~2.5kV across it. It lies perpendicularly to the detection chamber and comprises a light pipe of ~1m to enable the arrangement to be placed outside the influence of the magnetic field. CEMA2 is positioned as close to the NaI detector as possible, as shown in Figure 2.9a, in order to afford the maximum solid angle.

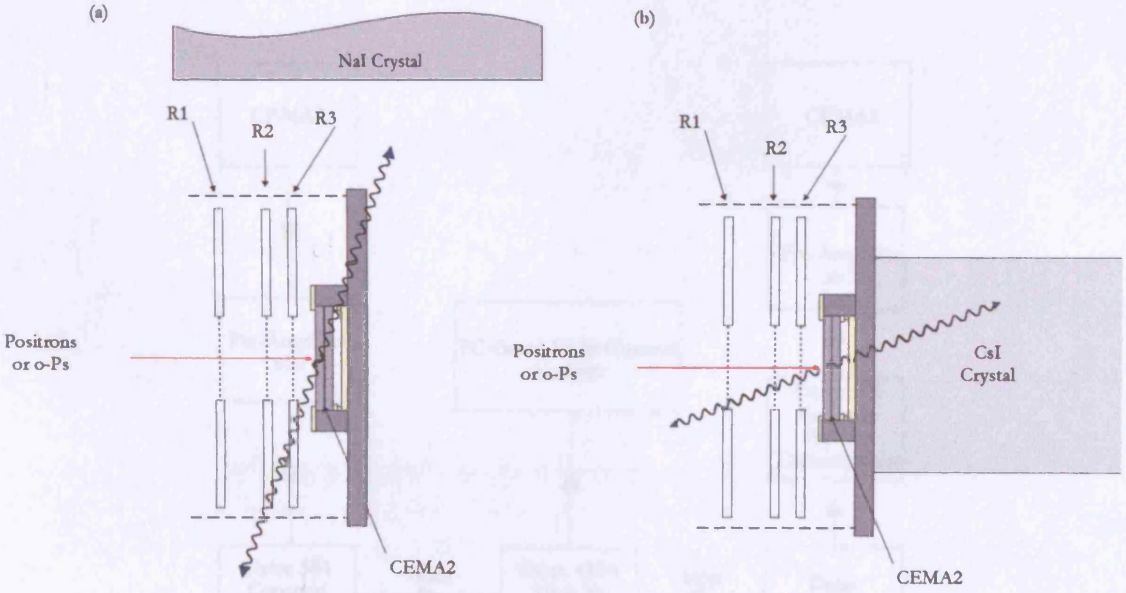

Figure 2.9 Position of the (a) NaI detector and (b) CsI detector with respect to CEMA2.

Alternatively, a CsI detector comprising a scintillator crystal, 40mm thick and 40mm in diameter, coupled to a photodiode (eV-251-03) may be used. The photodiode is not susceptible to magnetic fields, so can be situated within the beamline behind CEMA2 at a fixed solid angle, as shown in Figure 2.9b.

2.7 Detection Systems

2.7.1 Time-of-flight detection system

The tagger (CEMA1) and end of beamline detector (CEMA2) may be utilised to give a time-of-flight spectrum by providing stop and start signals respectively, to give an inverted timing sequence (Davies, 1987). This setup was used due to the fact that the tagger gave approximately eight times the number of pulses obtained from CEMA2, therefore, a reduction in the dead time of the system could be achieved. The pulses from each detector were fed into a pre-amplifier (×10) before being passed through a constant fraction discriminator (CFD). The signal from the tagger CFD was delayed by 754ns before being sent to the stop input of a time to amplitude convertor (TAC), whilst that from CEMA2 was sent to the start input. This output was then fed to a PC-based multi-channel analyser (Ortec MCA), as shown in Figure 2.10. Examples of the time-of-flight spectra for the incident positron beam, incident positronium beam and background, obtained with vacuum in both cells, are shown in Figure 2.11. Spectrum a) was obtained using an incident positron beam of 38.6eV. The larger peak in this spectrum corresponds to remoderated positrons detected at CEMA2 and the smaller peak (X) corresponds to electrons, released at CEMA2 via positron impact, travelling back down the

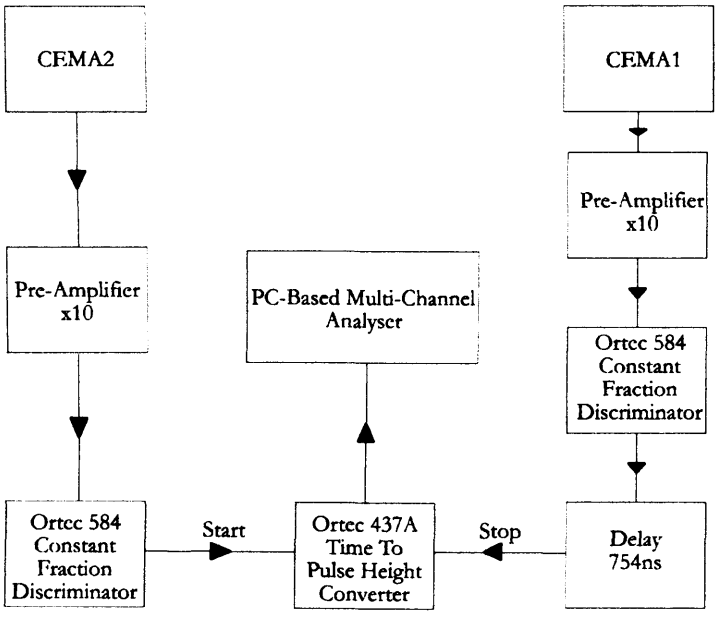

Figure 2.10 Electronics for the time-of-flight detection system.

beamline to be detected at CEMA1. Spectrum b) was obtained by neutralising the positron beam via charge-exchange with H_2 in the production cell. A number of peaks are seen in this spectrum: the peak from positronium is seen around channel 560 and the t_0, at channel 840, arises from positrons annihilating at the remoderator. This peak relies on either back-to-back gamma-rays from positron annihilation at the remoderator being detected at CEMA1 or an electron liberated from the remoderator being detected at CEMA1 in coincidence with one of the annihilation photons being detected at CEMA2. The peak marked Y corresponds to positrons and positronium annihilating at the gas cells and CR1 (shown in Figure 2.7). In spectrum c), measured with vacuum in both cells, similar peaks to those in spectrum b) can be seen, with the exception of the positronium peak.

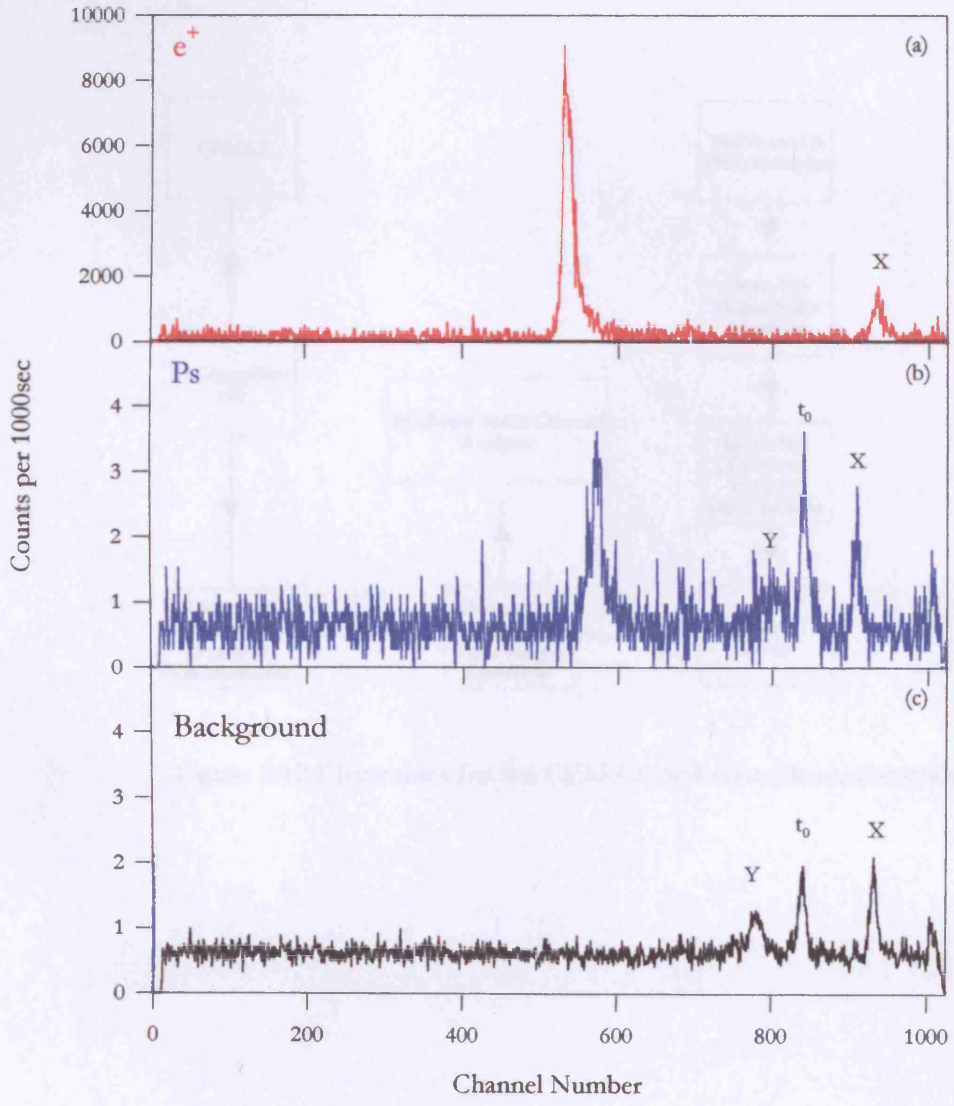

Figure 2.11 Time-of-flight spectra for a) positrons, b) positronium and c) the background.

2.7.2 CEMA2/NaI coincidence detection system

As with the time-of-flight system, CEMA2 provides the start signal but here, the NaI detector provides the stop signal. The output from the NaI was fed into a timing filter amplifier and then into a CFD. The NaI signal was delayed for 500ns and then fed into the TAC. A schematic of the electronics is shown in Figure 2.12 and examples of a) the incident positron, b) the incident positronium and c) the background spectra, in Figure 2.13. Spectrum a) was obtained with an incident positron beam of 24.6eV and b), by neutralising the positron beam in the production cell, which contained molecular hydrogen gas at a pressure of 10μmHg. Spectrum c) was taken with the same conditions in the production cell, but with helium in the scattering cell at a pressure of 7μmHg. Spectrum d) is a measurement of the background, taken with vacuum in both cells.

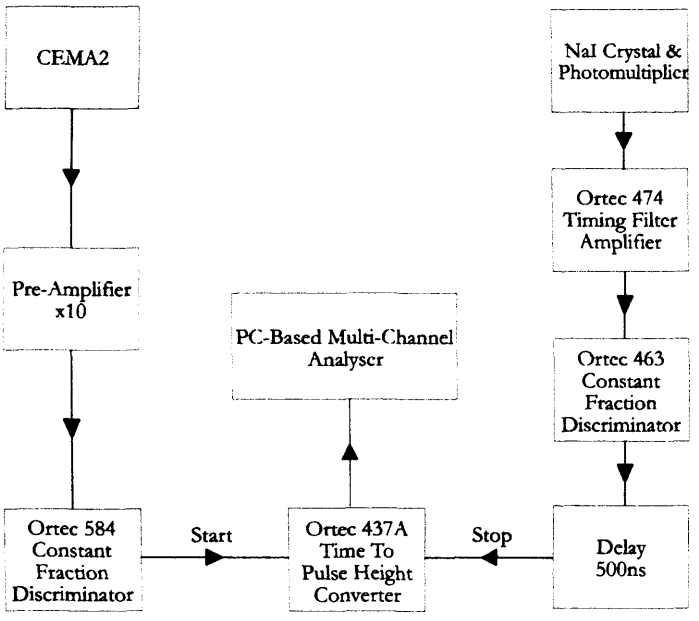

Figure 2.12 Electronics for the CEMA2/NaI coincidence detection system.

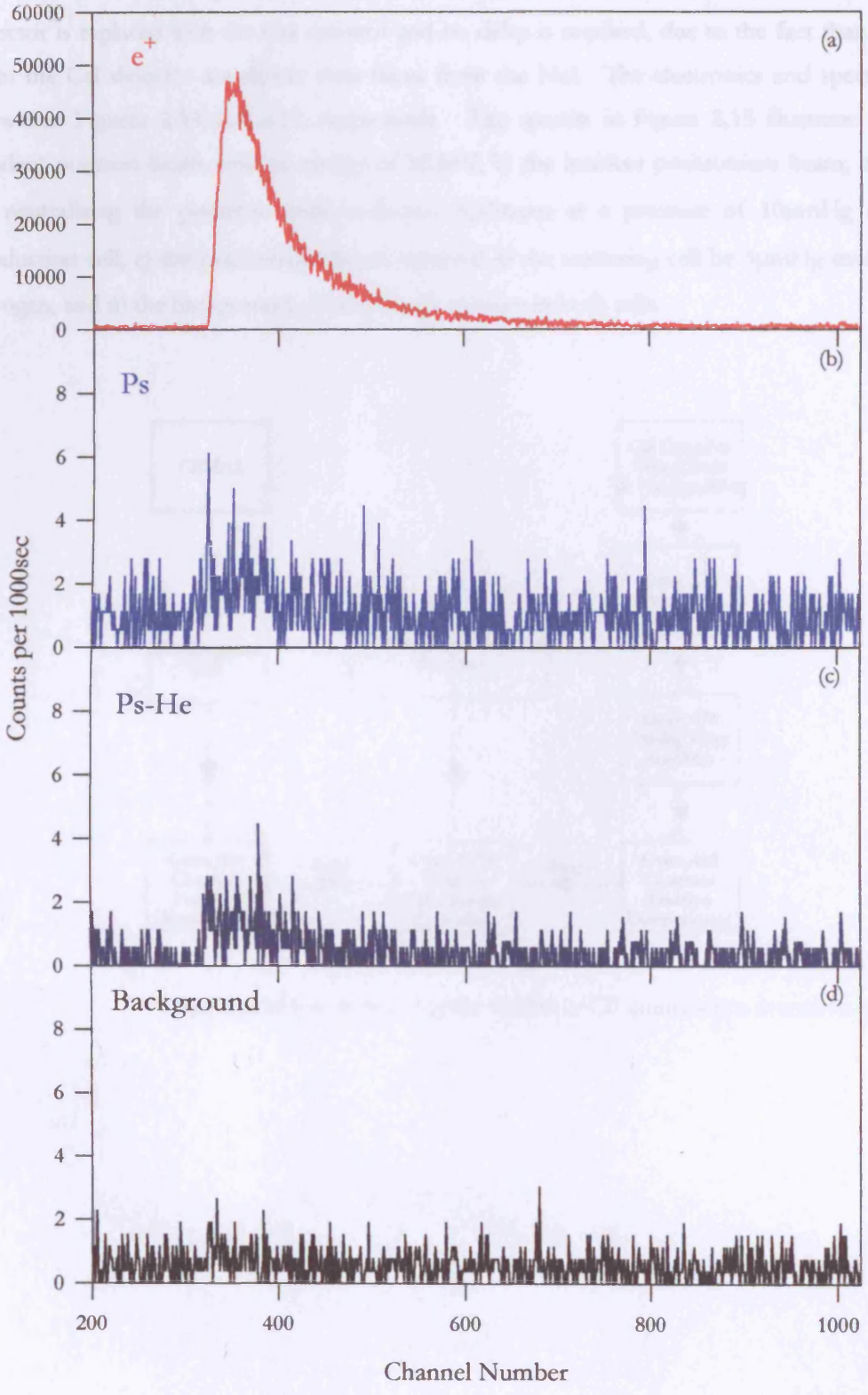

Figure 2.13 CEMA2/NaI coincidence spectra for a) positrons, b) positronium, c) Ps-He and d) the background.

2.7.3 CEMA2/CsI coincidence detection system

This detection system is similar to that described in the previous section. The NaI detector is replaced with the CsI detector and no delay is required, due to the fact that pulses from the CsI detector are slower than those from the NaI. The electronics and spectra are shown in Figures 2.14 and 2.15, respectively. The spectra in Figure 2.15 illustrate: a) the incident positron beam, with an energy of 38.6eV; b) the incident positronium beam, created by neutralising the positrons with molecular hydrogen at a pressure of 10μmHg in the production cell; c) the positronium beam scattered in the scattering cell by 3μmHg molecular nitrogen; and d) the background, obtained with vacuum in both cells.

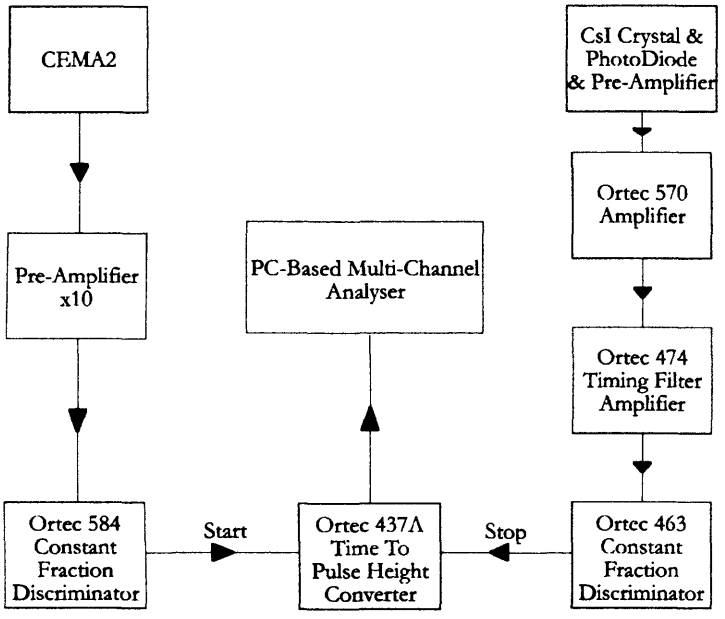

Figure 2.14 Electronics for the CEMA2/CsI coincidence detection system.

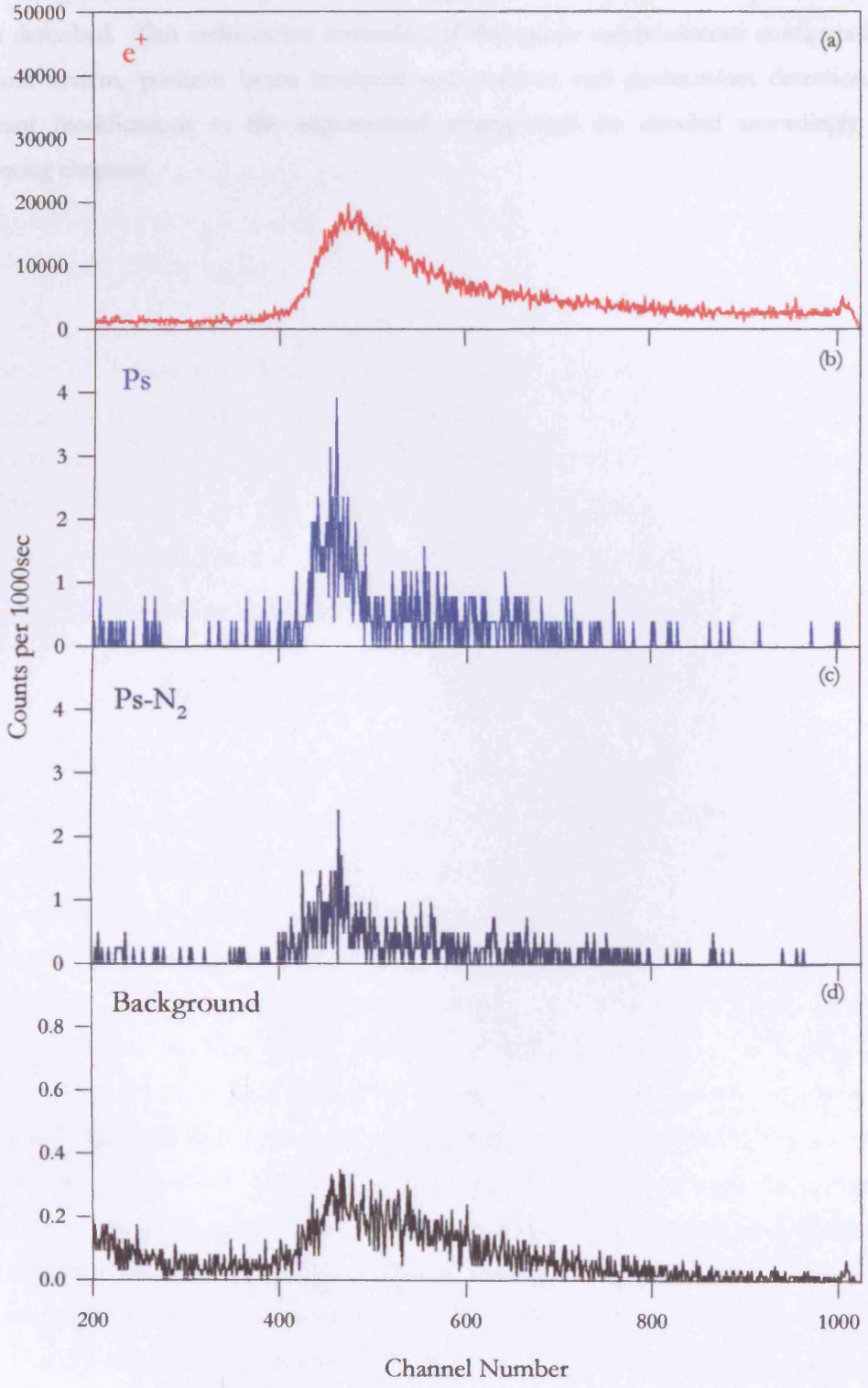

Figure 2.15 CEMA2/CsI coincidence spectra for a) positrons, b) positronium, c) Ps-N_2 and d) the background.

2.8 Summary

In this chapter, the main components of the apparatus used throughout the present work have been described. This includes the discussion of the source and moderator configuration, the vacuum system, positron beam transport and positron and positronium detection. Any relevant modifications to the experimental arrangement are detailed accordingly in the following chapters.

Chapter 3

Positronium Beam Production Efficiency

3.1 Overview

Provided there are no inelastic effects simultaneous to positronium formation, the kinetic energy of a beam of positronium atoms (E_{Ps}) is tuneable via that of the positron beam (E_+) (Laricchia *et al*, 1987) according to:

$$E_{Ps} = E_+ - I + 6.8eV/n^2 , \qquad 3.1$$

where I is the ionisation energy of the production gas and 6.8eV/n² is the positronium binding energy in a state of principal quantum number n. The efficiency for the production of a beam of positronium atoms is dependent on the differential positronium formation cross-section, $d\sigma_{Ps}/d\Omega$, of the target gas used to neutralise the positron beam and the total cross-sections, σ_T, for both positron and positronium scattering (corresponding superscripts $^+$ and ^{Ps}, respectively). The positronium beam production efficiency, ε_{Ps}, can be expressed as:

$$\varepsilon_{Ps} \propto \left\{1 - \exp\left(-\rho l_+ \sigma_T^+\right)\right\}\left\{\frac{1}{\sigma_T^+}\int_0^{\theta'} \frac{d\sigma_{Ps}}{d\Omega}\sin\theta d\theta\right\}\exp\left(-\rho l_{Ps}\sigma_T^{Ps}\right), \qquad 3.2$$

where the first term corresponds to the fraction of scattered positrons, the second is related to the probability of forming positronium within the angular range $0-\theta'$ and the third, to the transmission probability of positronium through a gas of number density, ρ and length, l_{Ps}.

Investigations into the production of an energy tuneable beam of positronium atoms have been made previously. Laricchia *et al* (1987) and Zafar *et al* (1991) studied the production efficiency obtained via the charge-exchange reaction of positrons in gaseous argon and helium. This investigation was extended by Garner *et al* (1996) to include molecular hydrogen, as described in §1.6.1. The present study has extended the range of targets to include molecular nitrogen. This was chosen because, among those studied, molecular hydrogen had been determined to be the most efficient, especially at low energies, thus a larger diatomic molecule seemed appropriate for investigation. It has been found that using molecular nitrogen as the neutralising gas enables the production of a collimated positronium beam up to 250eV, as well as providing a more efficient convertor than molecular hydrogen above 90eV.

As detailed in §1.5, Laricchia *et al* (2002) conjectured that the second peak seen in the positronium formation cross-section from xenon might be due to the production of positronium in an excited state (Ps*). Estimates were extracted which indicated that, at 40eV, 50-100% of the positronium could be formed in an excited state. Encouraged by the possibility of forming a beam of Ps*, the beam production efficiency from xenon and the

dominant quantum state of positronium have been investigated. The overall yield of forward-going positronium atoms has been found to be lower than suggested by the integrated positronium formation cross-section, whilst investigation of the quantum state of the beam indicated that the beam is primarily comprised of ground state positronium atoms.

3.2 Experimental Procedure

In this study, measurements of the positronium beam production efficiency have been carried out for both molecular nitrogen (N_2) and molecular hydrogen (H_2) across a range of pressures (0-16μmHg) and positronium kinetic energies between 30-250eV. Data have been obtained using the NaI-CEMA2 detection system discussed in §2.7.2, i.e. the channel-electron-multiplier-array (CEMA2) at the end of the beamline in coincidence with a NaI gamma-ray detector. The detector signals have been monitored using two multichannel scalers (MCS) and a multichannel analyser (MCA) has been used to record coincidences between them. The intensity of the positronium beam has been measured for 3600sec and the incident positron beam has been monitored in between each measurement. During the positronium measurements, positive potentials have been applied to retarders R1 and CR1 (see Figure 2.1) in order to prevent positrons transmitted through the production cell from reaching the detectors.

The positronium beam energy distribution has been ascertained by conversion of the time-of-flight spectra (see Figure 2.11). This required calibration of the TAC-MCA system via measurement of the time per channel, t_{ch}. This was done by inserting known time delays on the

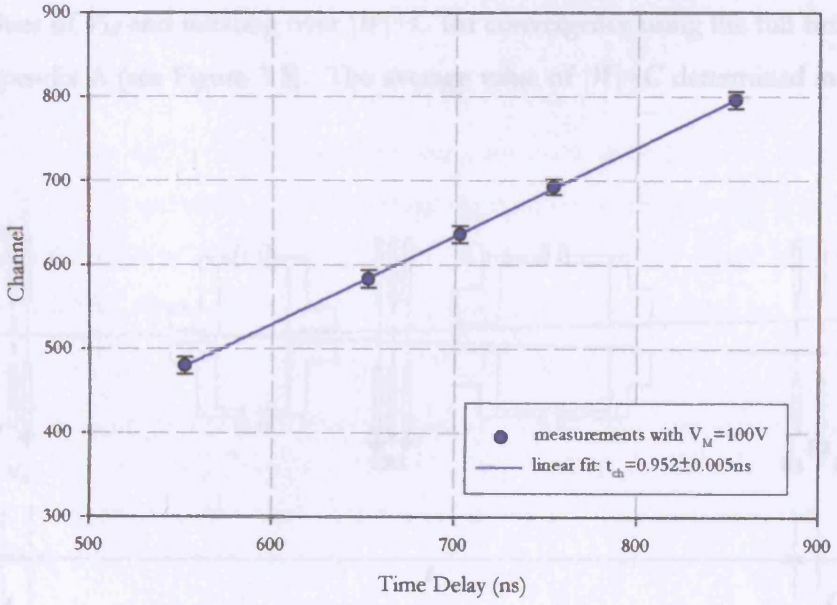

Figure 3.1 Example of the measurements required for the determination of the time per channel, t_{ch}.

stop input of the time-to-amplitude convertor (see §2.7.1) and noting, for each time delay, the channel number where a peak occurred. A linear plot was made, such as that shown in Figure 3.1, the gradient of which yields t_{ch}.

From knowledge of t_{ch} and measurements of the change in the positron peak in the time-of-flight spectrum with energy, the sum of the magnitude of the workfunction (W) corrected for possible contact potential (C) effects, $|W|+C$, has been determined. This is required in order to determine the absolute energy of the positronium beam as per equation 3.1, where the kinetic energy of the positron beam, E_+, is given by:

$$E_+ = eV_M + |W| + C, \tag{3.3}$$

where V_M is the remoderator potential. The channel at which the positron peak appears, $ch_+(E)$, is given by:

$$ch_+(E) = ch_0 - t_+(E)/t_{ch}, \tag{3.4}$$

where ch_0 is the channel at which the time-zero peak occurs and $t_+(E)$ is the time between the CEMA1 and CEMA2 pulses, which may be expressed as:

$$t_+(E) = t_c - t_{e^-} + t_{e^+} + t_r. \tag{3.5}$$

Figure 3.2 provides a schematic definition of the times used in equation 3.5: t_c is the time taken for a positron of constant velocity ($v_{e+} = \sqrt{2E_+/m}$, where m is the mass of the positron) to travel from the earth grid of the CEMA1 configuration to R1, t_{e-} and t_{e+} are the acceleration times for secondary electrons and remoderated positrons from the remoderator to CEMA1 and the earth grid, respectively, and t_r is the acceleration time for the positrons through the grids in front of CEMA2. $|W|+C$ may, therefore, be determined by measuring $ch_+(E)$ at different values of V_M and iterating over $|W|+C$ for convergence using the full fitting equation given in Appendix A (see Figure 3.3). The average value of $|W|+C$ determined in this work is (1.1±0.2)eV.

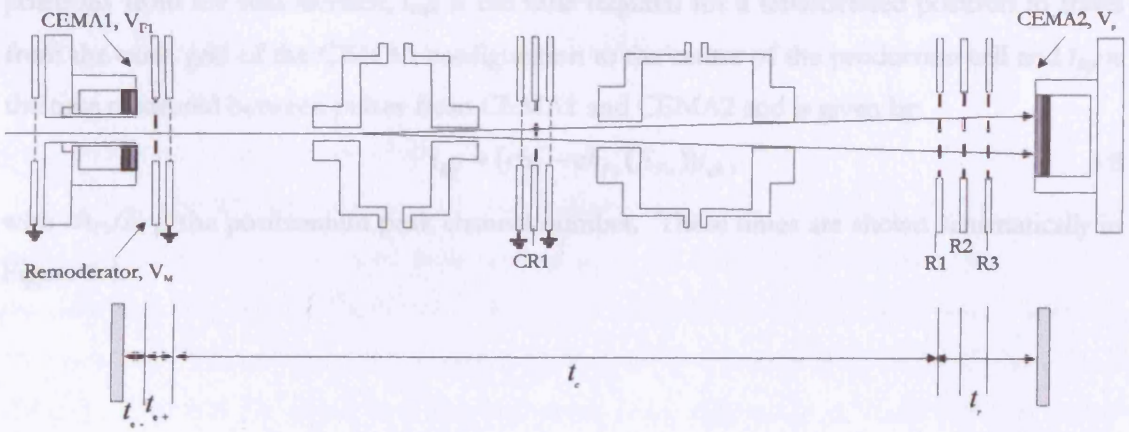

Figure 3.2 Schematic definition of the times used for determination of $|W|+C$.

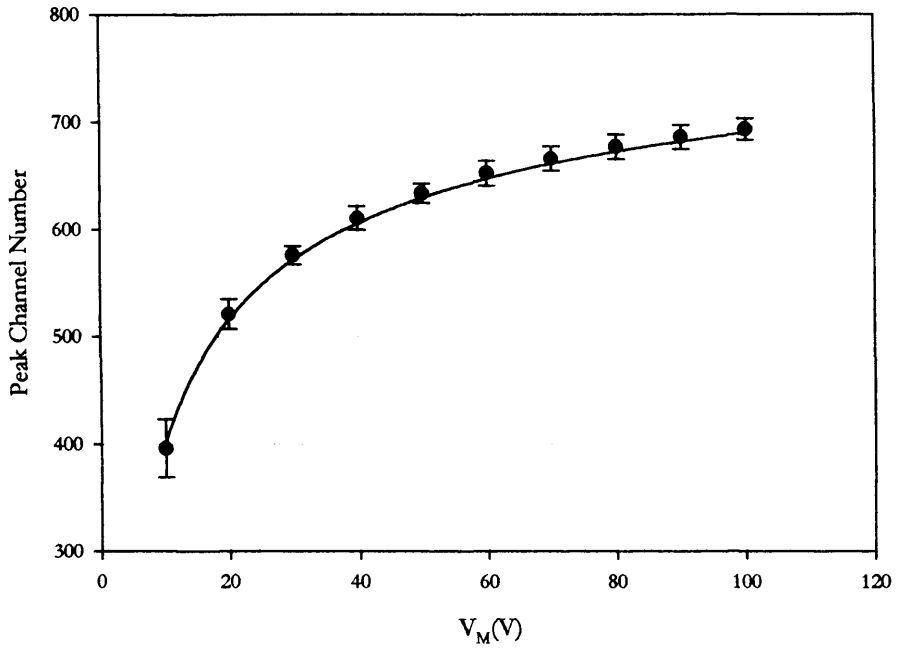

Figure 3.3 Determination of the workfunction and contact potential, $|\Phi^-|+C$, via comparison of the measured position of the positron peak and the calculated value.

The energy of the positronium beam can be calculated from the time-of-flight spectrum using:

$$E_{Ps} = m\left(\frac{L_{Ps}}{t_{Ps}}\right)^2, \tag{3.6}$$

where m is the positron mass, L_{Ps} is the positronium flight length and t_{Ps} is the time taken for a positronium atom to travel from the centre of the production cell to CEMA2. This may be expressed as:

$$t_{Ps} = t_{tof} - t_{e^-} + t_{e^+} - t_{cell}, \tag{3.7}$$

where t_{e-} and t_{e+} are again the acceleration times for secondary electrons and remoderated positrons from the remoderator, t_{cell} is the time required for a remoderated positron to travel from the earth grid of the CEMA1 configuration to the centre of the production cell and t_{tof} is the time measured between pulses from CEMA1 and CEMA2 and is given by:

$$t_{tof} = (ch_0 - ch_{Ps}(E_{Ps}))t_{ch}, \tag{3.8}$$

with $ch_{Ps}(E_{Ps})$ the positronium peak channel number. These times are shown schematically in Figure 3.4.

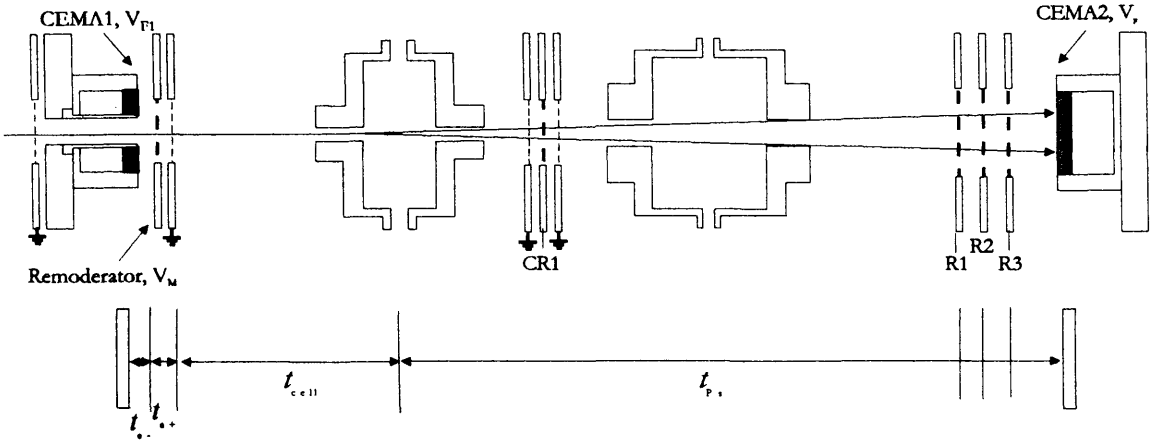

Figure 3.4 Schematic definition of the times required to determine the absolute positronium energy.

3.3 Results

The positronium production efficiency, ε_{Ps}, has been defined in §1.6.1 as the number of positronium atoms produced per incident positron per steradian in accordance with:

$$\varepsilon_{Ps} = \frac{N_{Ps}}{\Omega N_+} D, \tag{3.9}$$

where N_{Ps} and N_+ are the number of positronium atoms and incident positrons, respectively and D accounts for the decay of positronium atoms of energy, E_{Ps}, along the flight length to the detector, d, i.e.:

$$D = \exp\left(\frac{-t}{\tau}\right) = \exp\left[\left(\frac{-d}{\tau}\right)\left(\frac{m}{eE_{Ps}}\right)^{\frac{1}{2}}\right] = \exp\left(\frac{-16.79(d)}{[E_{Ps}(eV)]^{\frac{1}{2}}}\right), \tag{3.10}$$

where d=(0.654±0.001)m and Ω=(1.14±0.01)msr is the detection solid angle subtended by CEMA2. In the following sections, the results obtained in the present work for molecular hydrogen, molecular nitrogen and xenon are presented and compared with the previous work of Garner *et al* (1996). The energy distributions of the positronium beam produced in each case have also been determined by transformation of the corresponding time-of-flight spectra.

3.3.1 Molecular Hydrogen and Molecular Nitrogen

The results obtained for the positronium production efficiency, ε_{Ps}, of molecular hydrogen and molecular nitrogen in the energy range 30-250eV are shown in Figure 3.5 along with the previous data of Garner *et al* (1996) for molecular hydrogen, argon and helium for completeness. The present data for H_2 can be seen to be consistent with those of Garner *et al* (1996). It should be noted that measurements from this study at E_{Ps}=65eV are shown alongside previous data of Garner *et al* at 60eV.

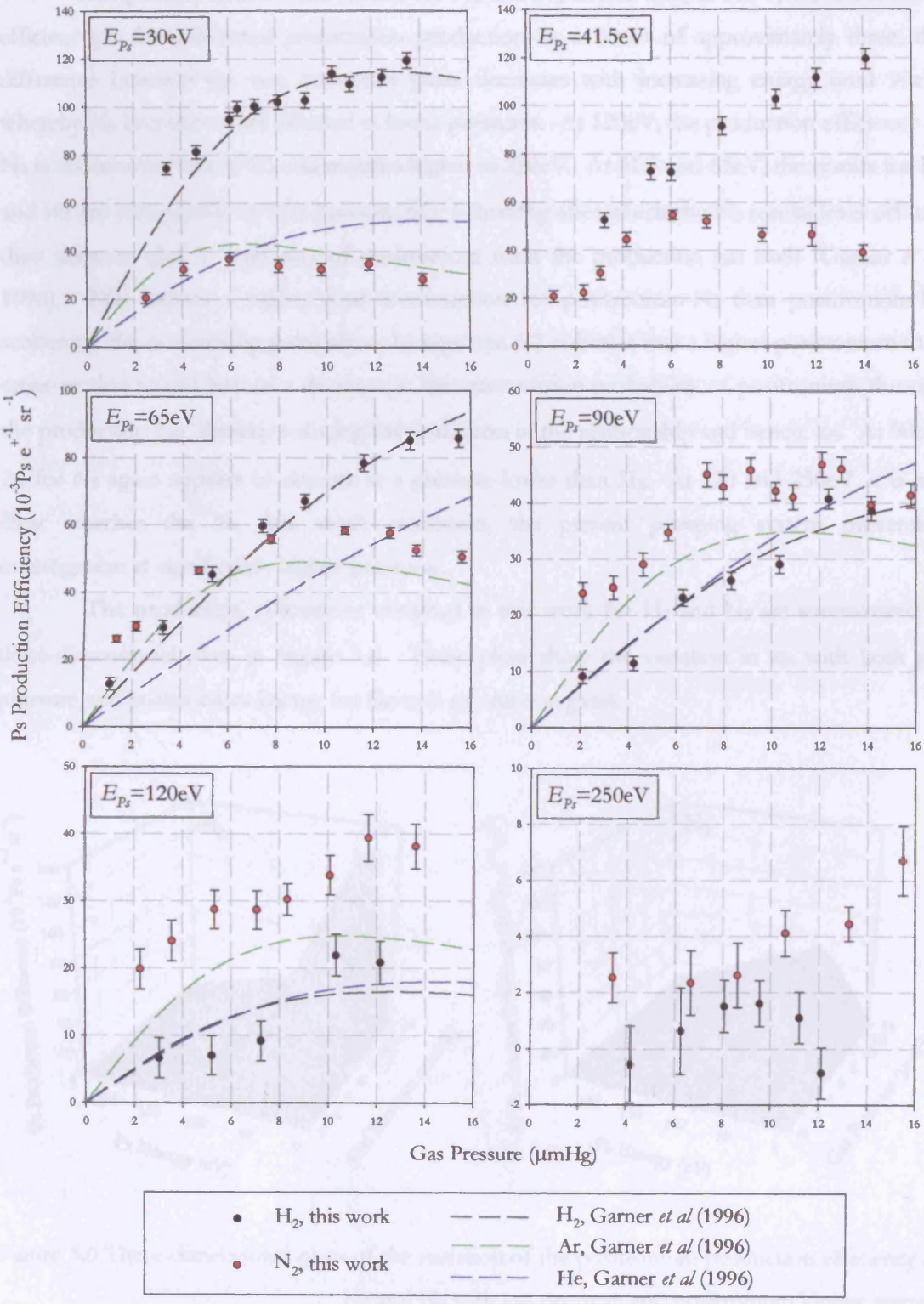

Figure 3.5 Pressure dependence of the positronium beam production efficiency for various targets and positronium kinetic energies.

Comparison between the results for H_2 and N_2 shows that, at 30eV, H_2 is the more efficient gas for collimated positronium production by a factor of approximately three; the difference between the two convertor gases decreases with increasing energy until 90eV, whereby N_2 becomes more efficient at lower pressures. At 120eV, the production efficiency of N_2 is about twice that of H_2 and remains higher at 250eV. At 41.5 and 65eV, the results for H_2 and N_2 are comparable up to a pressure of ~6-8μmHg after which the N_2 results level off and then decrease due to scattering of positronium from the production gas itself (Garner *et al*, 1996). This implies a higher total cross-section for positronium-N_2 than positronium-H_2 scattering: the relationship given above by equation 3.2 indicates that a higher positronium total cross-section would lead to a decrease in the transmission probability of positronium through the production gas, thereby reducing the third term in the relationship and hence, ε_{Ps}. At 90eV, ε_{Ps} for N_2 again appears to saturate at a pressure lower than H_2. At 120 and 250eV, it is not clear whether the N_2 data reach saturation, the present pumping system preventing investigation at significantly higher pressures.

The production efficiencies obtained in this work for H_2 and N_2 are summarized as three-dimensional plots in Figure 3.6. These plots show the variation in ε_{Ps} with both gas pressure and positronium energy for the two production gases.

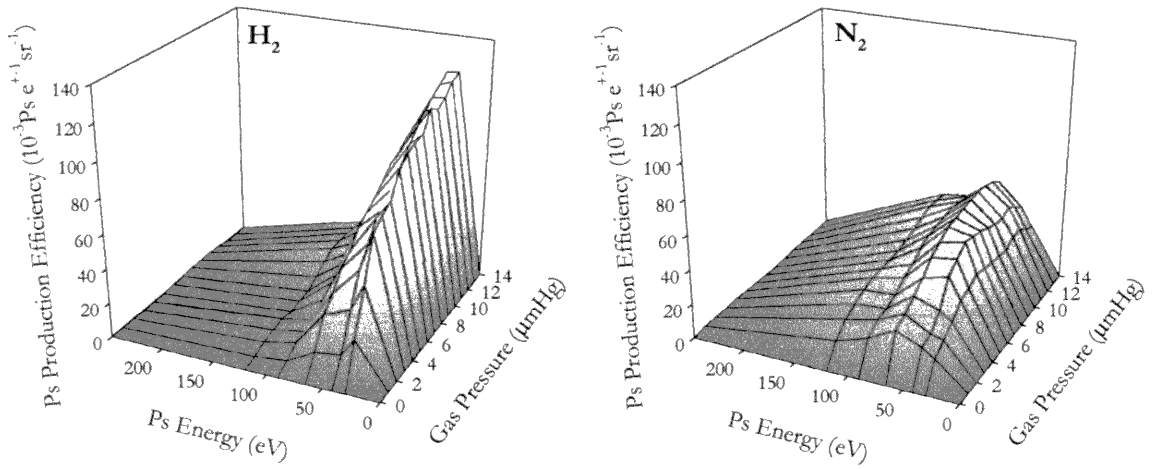

Figure 3.6 Three dimensional plots of the variation of the positronium production efficiency of H_2 and N_2 with gas pressure and positronium kinetic energy.

3.3.2 Determination of the Positronium Beam Energy Distribution

In order to determine the kinetic energy and thus dominant quantum state of the positronium beam, the time-of-flight detection method has been used, as detailed in §3.2. The energy distribution, ΔE, of the incident positron beam (from the argon RGS moderator or the

tungsten remoderator) has been measured by applying a retarding potential to the grid R2, in front of CEMA2. The other grids in the arrangement were kept at ground during these measurements in order to parallelise the **E**-field and minimise the effects of field penetration. As the potential on R2 was increased from below the source/remoderator potential ($V_{S/M}$) to above, the intensity of the positron beam was measured and then differentiated with respect to energy to yield energy distributions of the positron beam from either moderator as shown below.

Gullikson and Mills (1986) and Petkov *et al* (1997) have estimated values of the FWHM of the energy spread of a positron beam from an argon RGS moderator as being 1.7±0.2eV and 2.0eV respectively, with a long tail being attributed to the contribution from epithermal positron emission (see §2.2.2). The energy distribution from the argon RGS moderator used in this work is shown in Figure 3.7, where it can be seen that its width of (1.9±0.1)eV is comparable to the data of Gullikson and Mills (1986) and Petkov *et al* (1997).

Figure 3.8 shows the energy distribution of the remoderated positron beam. The implantation energy (V_S) was rather low (500V) for these measurements, resulting in a large epithermal contribution. This high energy tail could be reduced by increasing the positron implantation energy, although this would result in a decrease in the beam intensity. The FWHM of the remoderated beam shown in Figure 3.8 is (2.4±0.1)eV.

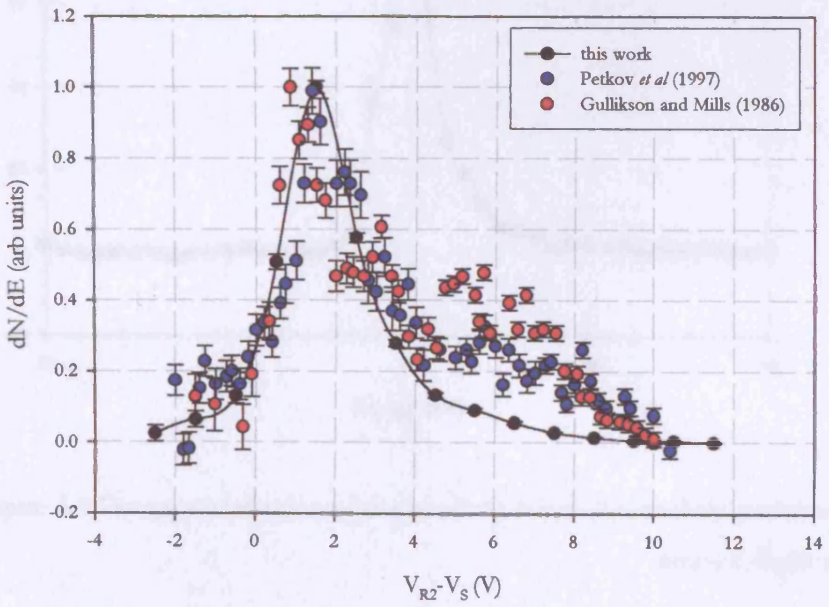

Figure 3.7 Energy distribution of the positron beam from an argon RGS moderator.

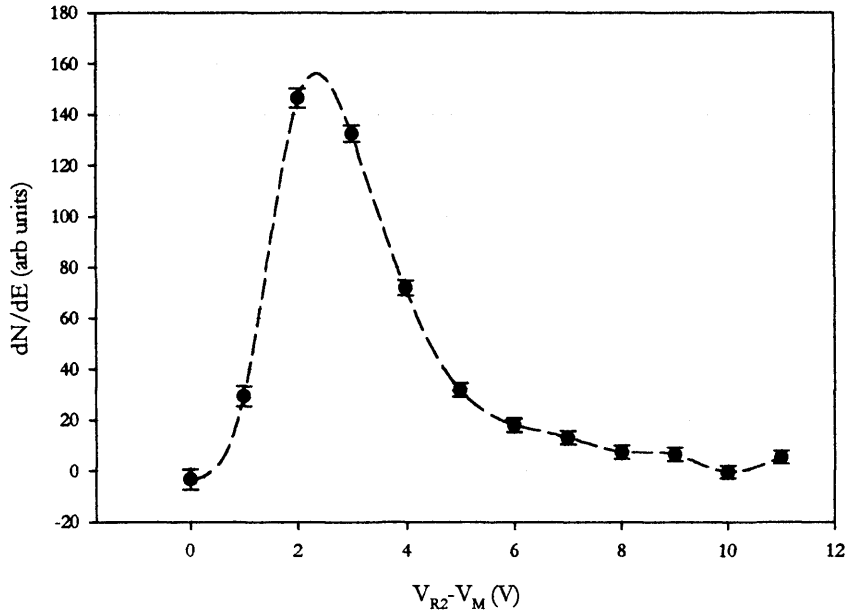

Figure 3.8 Energy distribution of the positron beam from the tungsten remoderator at CEMA1.

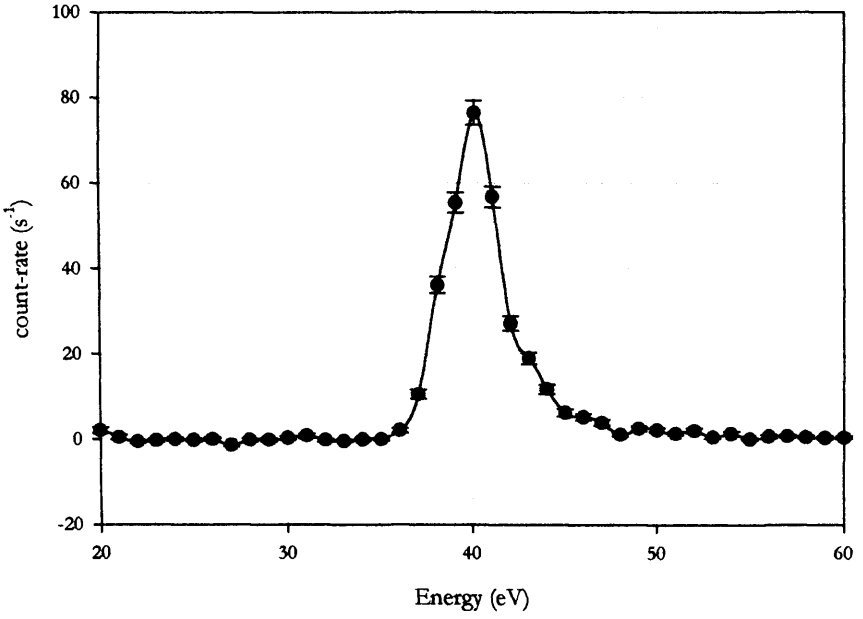

Figure 3.9 Energy distribution of the positron beam obtained by conversion of the time-of-flight spectrum.

Figure 3.9 gives an example of the energy distribution of the positron beam (V_M=38.6V), obtained after conversion of the time-of-flight spectrum. The FWHM of this apparent energy distribution is (3.6±0.3)eV, the widening in comparison to that shown in Figure 3.8 is due to the intrinsic timing resolution, Δt_i, of the detection system, which may be

evaluated directly from the full width at half maximum (FWHM) of the time-zero (t_0) peak shown in Figure 2.11, multiplied by t_{ch}. The t_0 peak has been approximated to a Gaussian distribution, although some asymmetry is evident. For positrons of energy E_+(eV), the time taken to travel a length L to the detector is given by:

$$t = \sqrt{\frac{m}{2eE_+}} L, \qquad 3.12$$

which has an associated time-spread of:

$$\Delta t = \frac{t}{2}\frac{\Delta E}{E_+}, \qquad 3.13$$

where ΔE is the intrinsic energy spread of the positron beam taken to be the FWHM of the energy distribution shown in Figure 3.8. The width of the positron peak measured using the time-of-flight system is given by:

$$\Delta t_{tof} = \sqrt{\Delta t^2 + \Delta t_i{}^2}, \qquad 3.14$$

which corresponds to an apparent energy spread of:

$$\Delta E_{tof} = 2E_+\left(\frac{\Delta t_{tof}}{t}\right). \qquad 3.15$$

Determinations of the energy spreads of the positron and positronium beams from 30-250eV, showed a shift in the observed peak position with respect to that expected from equation 3.3. The shift became increasingly evident, at (1.5±0.1)eV for V_M=38.6V and at (10.2±0.2)eV for V_M=258.8V. In order to investigate this, the tagger configuration and particle trajectories were simulated using the Charged Particle Optics (CPO) programme illustrated below in Figure 3.10. This showed that the secondary electrons emitted from the remoderator

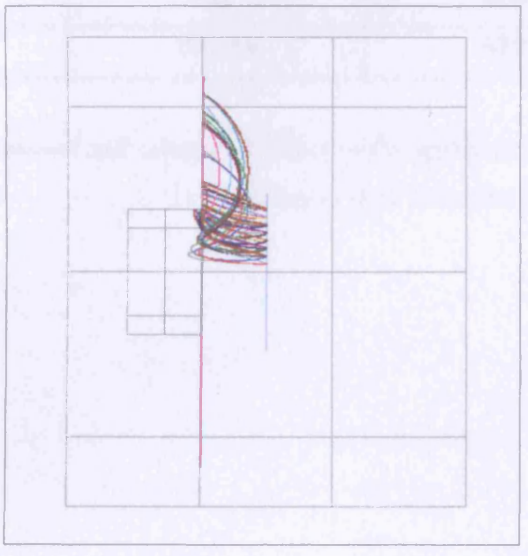

Figure 3.10 Example of the results obtained with CPO for determination of secondary electron trajectories.

and travelling back to CEMA1 do not follow straight trajectories as previously assumed, but take a variety of curved paths back to the detector. This indicated an underestimate of the time, t_{e-}, included in equations 3.5 and 3.7 for the transformation of the positron and positronium time- into energy-spectra. The increase in this time was calculated over the range of energies and for the magnetic field used in this study, was found to show little energy dependence having an average value of (4.1±0.8)ns across the range. With the inclusion of this new time, the peaks in the positron and positronium energy spectra occurred at the positions expected for the applied remoderator voltage and calculated values of t_{cb} and $|W|+C$.

Table 3.1 compares the measured results for ΔE_{tof} at each energy investigated in this work with the value calculated using equation 3.15. A good correspondence between the two can be seen, indicating that the apparent energy spread of the positron beam dominantly arises from the system timing resolution consistent with an intrinsic energy spread of (2.4±0.1)eV.

Figure 3.11 shows the apparent energy distributions for the positronium beam obtained from H_2 and N_2, the energy being set using equation 3.1 As can be seen, they show a broadly symmetric peak at an energy consistent with that for ground state positronium (with n=1), produced from both N_2 and H_2. The slight asymmetry may be attributed to the shape of the corresponding t_0 peaks, as mentioned above.

E_+(eV)	$\Delta E_{tof}(e^+)$from spectrum	$\Delta E_{tof}(e^+)$ (eV) from equation 3.15
38.8	3.3±1.6	3.6±0.6
98.8	11±5	12±2
128.8	13±7	20±3
258.8	31±15	41±7

Table 3.1 Comparison of measured and calculated values of the apparent energy spreads of the positron peak from the time-of-flight spectra.

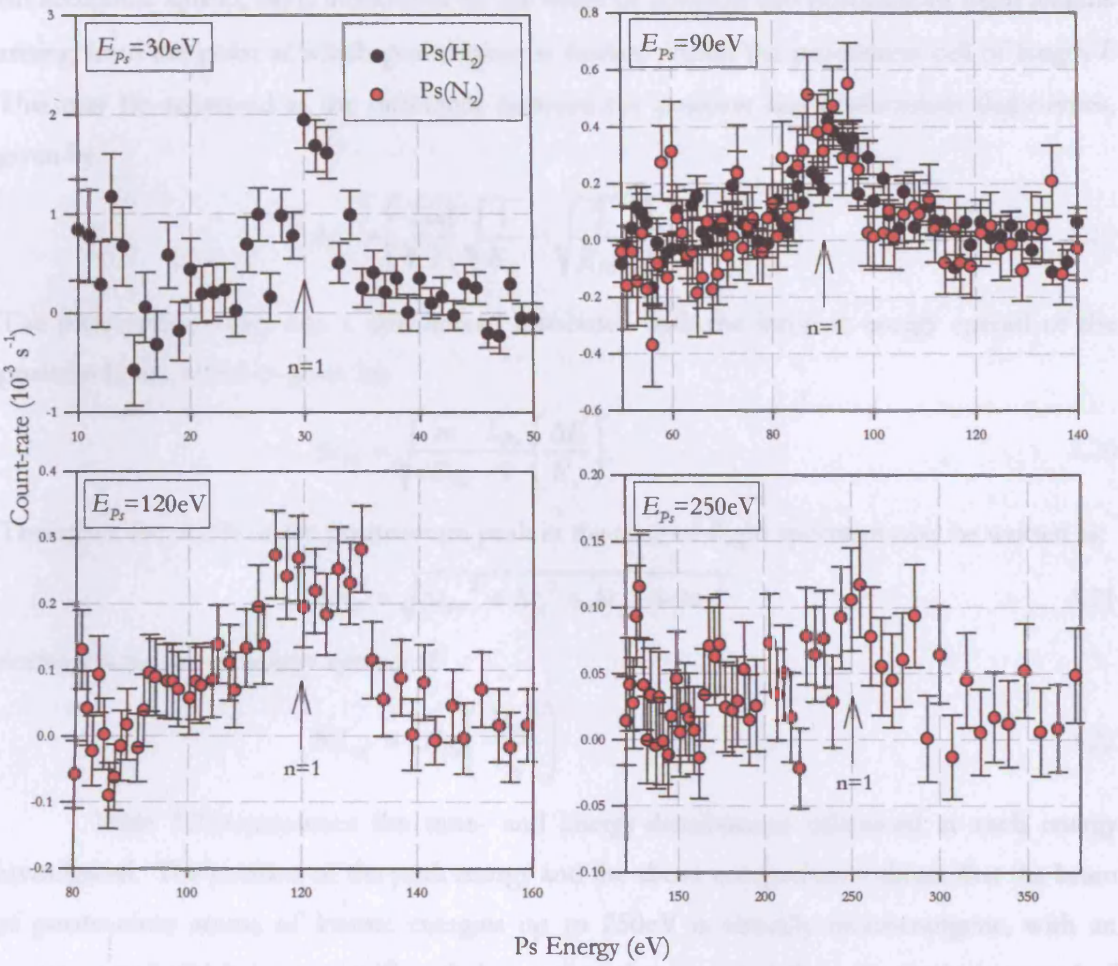

Figure 3.11 Apparent energy distributions of the positronium beam produced from molecular hydrogen and molecular nitrogen in the energy range E_{Ps}=30-250eV.

The width of the measured positronium energy distribution is also governed by the intrinsic timing resolution of the detection system, Δt_i, as well as additional instrumental time-spreads, discussed below. The time taken for a positron of kinetic energy E_+(eV) to travel a distance L_+ from the remoderator to reach the centre of the production cell is given by:

$$t_+ = \sqrt{\frac{m}{2eE_+}} L_+ \qquad 3.16$$

and the positrons will have a time spread of:

$$\Delta t_+ = \frac{t_+}{2}\frac{\Delta E}{E_+} \qquad 3.17$$

upon reaching the centre of the cell. Positronium of kinetic energy E_{Ps}(eV) formed in the production cell travels a distance L_{Ps} to the detector with a flight-time of:

$$t_{Ps} = \sqrt{\frac{m}{eE_{Ps}}} L_{Ps}. \qquad 3.18$$

An additional spread, Δt_f is introduced by the range of positron and positronium flight lengths arising from the point at which positronium is formed within the production cell of length l. This may be expressed as the difference between the positron and positronium flight-times, given by:

$$\Delta t_f = \left(\sqrt{\frac{m}{2}} \left(\sqrt{\frac{1}{E_+}} - \sqrt{\frac{2}{E_{Ps}}} \right) \right) l . \qquad 3.19$$

The positronium beam has a time-spread associated with the intrinsic energy spread of the positron beam, which is given by:

$$\Delta t_{Ps} = \sqrt{\frac{m}{eE_{Ps}}} \frac{L_{Ps}}{2} \left(\frac{\Delta E}{E_+} \right). \qquad 3.20$$

Therefore, the width of the positronium peak in the time-of-flight spectrum may be written as:

$$\Delta t_{tof} = \sqrt{\Delta t_{Ps}{}^2 + \Delta t_i{}^2 + \Delta t_f{}^2 + \Delta t_+{}^2} \qquad 3.21$$

corresponding to an energy spread of:

$$\Delta E_{tof} = 2E_{Ps} \left(\frac{\Delta t_{tof}}{t_{Ps}} \right). \qquad 3.22$$

Table 3.2 summarises the time- and energy-distributions calculated at each energy investigated. The position of the peak energy and the above comparison indicate that the beam of positronium atoms of kinetic energies up to 250eV is virtually monoenergetic, with an energy spread which is not significantly larger than that expected from the intrinsic spread of the positron beam ((2.4±0.1)eV) and the overall system timing resolutions.

E_{Ps}(eV)	ΔE_{tof}(Ps)from spectrum	ΔE_{tof}(Ps) (eV) from equation 3.22
30	6.2±0.2	3.0±0.5
90	11±1	10±2
120	25±1	17±3
250	33±5	35±6

Table 3.2 Calculated values of the corresponding energy spreads of the positronium peak in the time-of-flight spectrum at each energy investigated.

3.3.3 Xenon

Following the work of Laricchia *et al* (2002), which identified a double peak structure in the positronium formation cross-section from xenon, now confirmed by Marler *et al* (2005), the production of a beam of positronium atoms from xenon has been investigated or the first time.

In particular, the attribution of the second peak to a possible contribution from positronium in an excited state (Laricchia *et al*, 2002) has lead to the investigation of the dominant quantum state of the beam.

The positronium energy distribution from xenon has been measured for two different production gas pressures, 2 and 5μmHg, due to the fact that a higher target gas pressure would be expected to attenuate any Ps* more efficiently than it would ground state atoms. These are shown in Figure 3.12 and are compared with that obtained from H_2. Also shown in the figure are the positions of E_{Ps} for positronium being formed in the ground- (n=1) and excited (n=2) state. As can be seen, no significant structure consistent with that from Ps* is apparent in the beam produced from xenon. The spectra are similar to those from H_2 in the region, where any Ps* component would be expected, although Laricchia *et al* (2002) suggested that, at this energy, the contribution from Ps* from xenon may be 50-100%. The inability to identify such a component could be due to the timing resolution of the detection system, a broader differential cross-section for Ps* formation, or significant quenching/scattering which may remove Ps* more efficiently from the beam than ground state positronium.

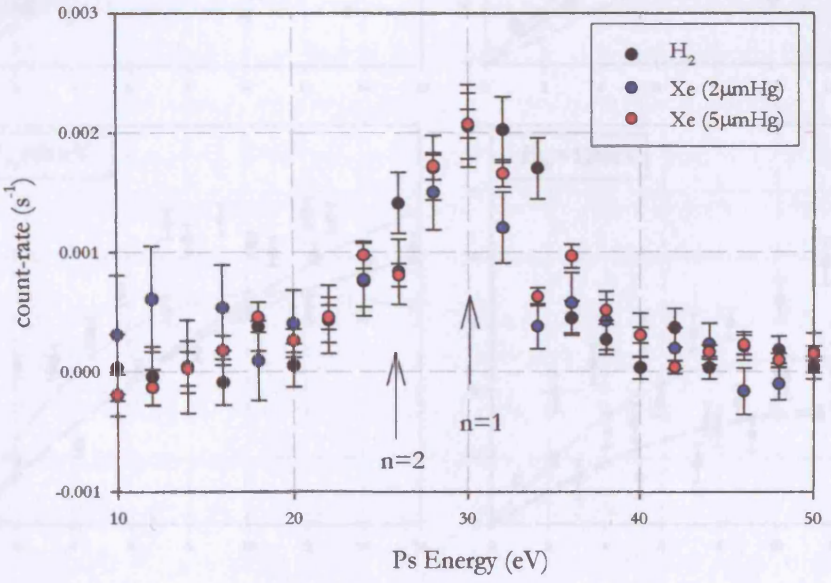

Figure 3.12 Comparison of positronium beam energy distributions from H_2 and Xe.

The positronium production efficiency of xenon has been measured for a range of target gas pressures at E_{Ps} of 30 and 50eV, using the time-of-flight detection system. Following this, further measurements of the positronium production efficiency from xenon were made with the same energy range and detection system as used in the study of molecular nitrogen (i.e. NaI-CEMA2). Both sets of data are shown in Figure 3.13, where they are compared with the

data for H_2 and N_2 from this study† as well as the previous data of Garner *et al* (1996) for H_2, He and Ar. At 30 and 60eV, the measurements for xenon can be seen to saturate before those of helium and argon: similar to the comparison made between H_2 and N_2 in §3.3.1, the positronium atoms formed via the charge-exchange reaction with xenon would be less likely to be transmitted through the gas due to a presumably higher total cross-section for positronium-xenon scattering than that of helium or argon. At 90eV, however, the measured ε_{Ps} for xenon is comparable to that for argon and at 120eV, the data are in broad agreement with those from both argon and helium.

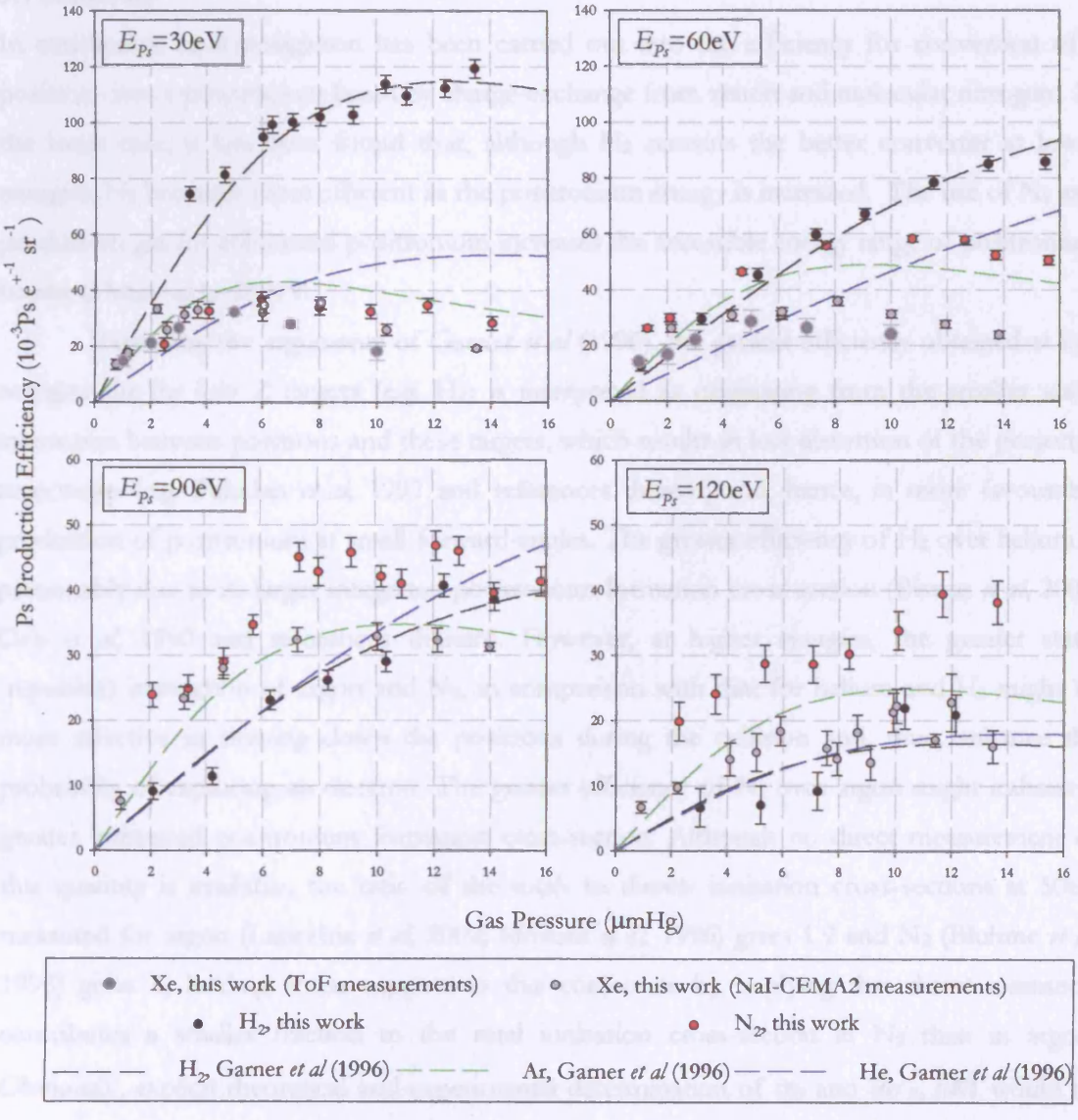

Figure 3.13 Pressure dependence of the positronium beam production efficiency from Xe at various positronium kinetic energies.

† The comparison at 60eV is made with H_2 and N_2 data from this study at 65eV.

The integrated positronium formation cross-section of Laricchia *et al* (2002) suggests that the positronium yield from xenon is high compared to other noble gases, however, measurements of the production efficiency show that relatively little positronium is detected in the forward direction (see Figure 3.13). A broad differential positronium formation cross-section, as predicted by McAlinden and Walters (1994) with a peak at around 20°, might provide an explanation for these findings i.e. large amounts of positronium are formed, but over a broad angular range. An alternative explanation is that positronium is lost to some efficient scattering/quenching mechanism (Heyland *et al*, 1982) in interactions with xenon.

3.4 Summary

In conclusion, an investigation has been carried out into the efficiency for conversion of a positron- into a positronium-beam by charge-exchange from xenon and molecular nitrogen. In the latter case, it has been found that, although H_2 remains the better converter at lower energies, N_2 becomes more efficient as the positronium energy is increased. The use of N_2 as a production gas for collimated positronium increases the accessible energy range of positronium beams at least up to 250eV.

Extending the arguments of Garner *et al* (1996), the greater efficiency obtained at low energies for the low Z targets (e.g. H_2) is interpreted as originating from the smaller static interaction between positrons and these targets, which results in less distortion of the projectile trajectories (e.g. Paludan *et al*, 1997 and references therein) and, hence, in more favourable production of positronium at small forward-angles. The greater efficiency of H_2 over helium is presumably due to its larger integrated positronium formation cross-section (Biswas *et al*, 2002; Deb *et al*, 1990 and references therein). However, at higher energies, the greater static (repulsive) interaction of argon and N_2, in comparison with that for helium and H_2 might be more effective in slowing down the positrons during the collision and, thus, enhance the probability of capturing an electron. The greater efficiency of N_2 over argon might indicate a greater integrated positronium formation cross-section. Although no direct measurement of this quantity is available, the ratio of the total- to direct- ionisation cross-sections at 50eV measured for argon (Laricchia *et al*, 2002; Moxom *et al*, 1996) gives 1.9 and N_2 (Bluhme *et al*, 1998) gives 4, lending some support to this conjecture by implying that direct ionisation contributes a smaller fraction to the total ionisation cross-section in N_2 than in argon. Obviously, explicit theoretical and experimental determination of σ_{Ps} and $d\sigma_{Ps}/d\Omega$ would be valuable in furthering our understanding.

The positronium beam production efficiency from xenon is lower than suggested by the integrated positronium formation cross-section. This may be due to a broader differential cross-section (McAlinden and Walters, 1994), expected by the increased static interaction in

comparison to H_2 or N_2, allowing for the explanation that large amounts of positronium are formed but little is detected in the forward direction. Alternatively, some rapid quenching mechanism, as invoked by Heyland *et al* (1982), might imply that positronium is lost due to the interaction with xenon. The quantum state of the beam has been investigated by measurement of the energy distribution and indicated that the beam which survives in the forward direction is comprised dominantly of ground state positronium atoms.

Chapter 4

Positronium Total Cross-Section

4.1 Overview

As discussed in §1.6.2, prior to the present work, measurements of the positronium total cross-section had been made for molecular hydrogen, molecular oxygen, argon and helium in the energy range 10-120eV. In this chapter, new determinations of the positronium total cross-sections of molecular hydrogen, molecular nitrogen and xenon are presented. Results have been extracted both indirectly, from the positronium beam production efficiency measurements (detailed in chapter 3), and directly, from beam-transmission measurements. Good agreement has been found between the two methods as well as with previous data, where available.

4.2 Indirect Determination of the Total Cross-Section

As discussed in §3.1, the positronium beam production efficiency may be expressed as:

$$\varepsilon_{Ps} \propto \left\{1-\exp\left(-\rho l_{+}\sigma_T^{+}\right)\right\}\left\{\frac{1}{\sigma_T^{+}}\int_0^{\theta'}\frac{d\sigma_{Ps}}{d\Omega}\sin\theta d\theta\right\}\exp\left(-\rho l_{Ps}\sigma_T^{Ps}\right), \qquad 4.1$$

where the first term corresponds to the fraction of scattered positrons, the second is related to the probability of forming positronium within the angular range $0-\theta'$ and the third to the transmission probability of positronium through a gas of number density, ρ and cell length for positronium, l_{Ps}. By assuming that the attenuation of the positronium atoms within the production cell is negligible at low pressures, the third term in equation 4.1 may be neglected and hence:

$$\varepsilon_{Ps}^{inc} = \kappa\left\{1-\exp\left(-\rho l_{+}\sigma_T^{+}\right)\right\}\left\{\frac{1}{\sigma_T^{+}}\int_0^{\theta'}\frac{d\sigma_{Ps}}{d\Omega}\sin\theta d\theta\right\}, \qquad 4.2$$

where κ is a constant. Thus, an extrapolation from low- to high- pressure of ε_{Ps} may be made, as illustrated in Figure 4.1, to obtain ε_{Ps}^{inc}, a measure of the incident beam at a given pressure, p. From plots such as this, the positronium total cross-section, σ_T^{Ps}, may be inferred from the observed deviations of ε_{Ps} from ε_{Ps}^{inc} using the Beer-Lambert law:

$$\sigma_T^{Ps} = \frac{1}{\rho l_{Ps}}\ln\left(\frac{\varepsilon_{Ps}^{inc}}{\varepsilon_{Ps}}\right). \qquad 4.3$$

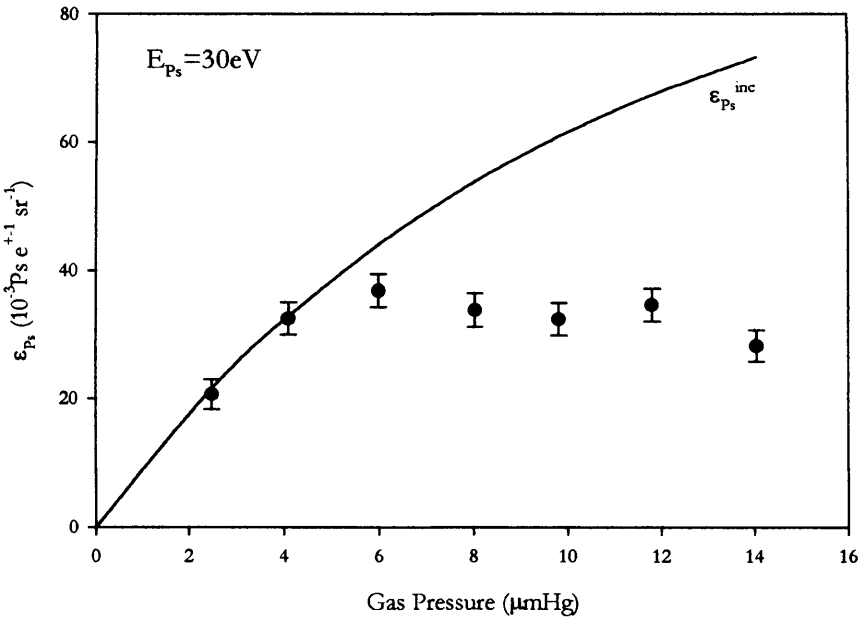

Figure 4.1 Illustration of the extrapolation method to obtain ε_{Ps}^{inc} according to equation 4.2.

The cell length for positronium, l_{Ps}, has been defined as the difference between the effective length of the production cell, l_+^P, and the point in the cell where half of the detected positronium atoms are formed. l_+^P has been determined by performing attenuation measurements with a positron beam and normalising to known σ_T^+ values (Kauppila and Stein, 1990; Hoffman *et* al, 1982; Dababneh *et al*, 1980 and 1982) according to:

$$l_+^P = \frac{kT}{p\sigma_T^+} \ln \frac{I_0}{I}, \qquad 4.4$$

where I_0 (I) is the incident (transmitted) beam, k is the Boltzmann constant, p is the target gas pressure, L is the effective length of the scattering cell and T is the ambient temperature. In order to facilitate this, the incident energy of the positrons was chosen to be in a region where σ_T^+ is constant within the energy spread of the beam, as indicated in Figure 4.2. A narrow, high-energy portion of the positron beam was selected in order to reduce the uncertainty introduced by positrons which may have scattered elastically at forward angles. This was achieved by using the grid CR1 between the gas cells (see Figure 2.1) to retard a large portion of the beam. In retrospect, both the retarding grids in front of CEMA2 may have been used, as opposed to CR1, for this purpose in order to determine the energy of the positron beam with better resolution. In the examples given below, CR1 was set to Vs+7V i.e. 31V, as indicated by the dashed vertical line in the figure, which resulted in a count-rate of ~400e^+s^{-1}.

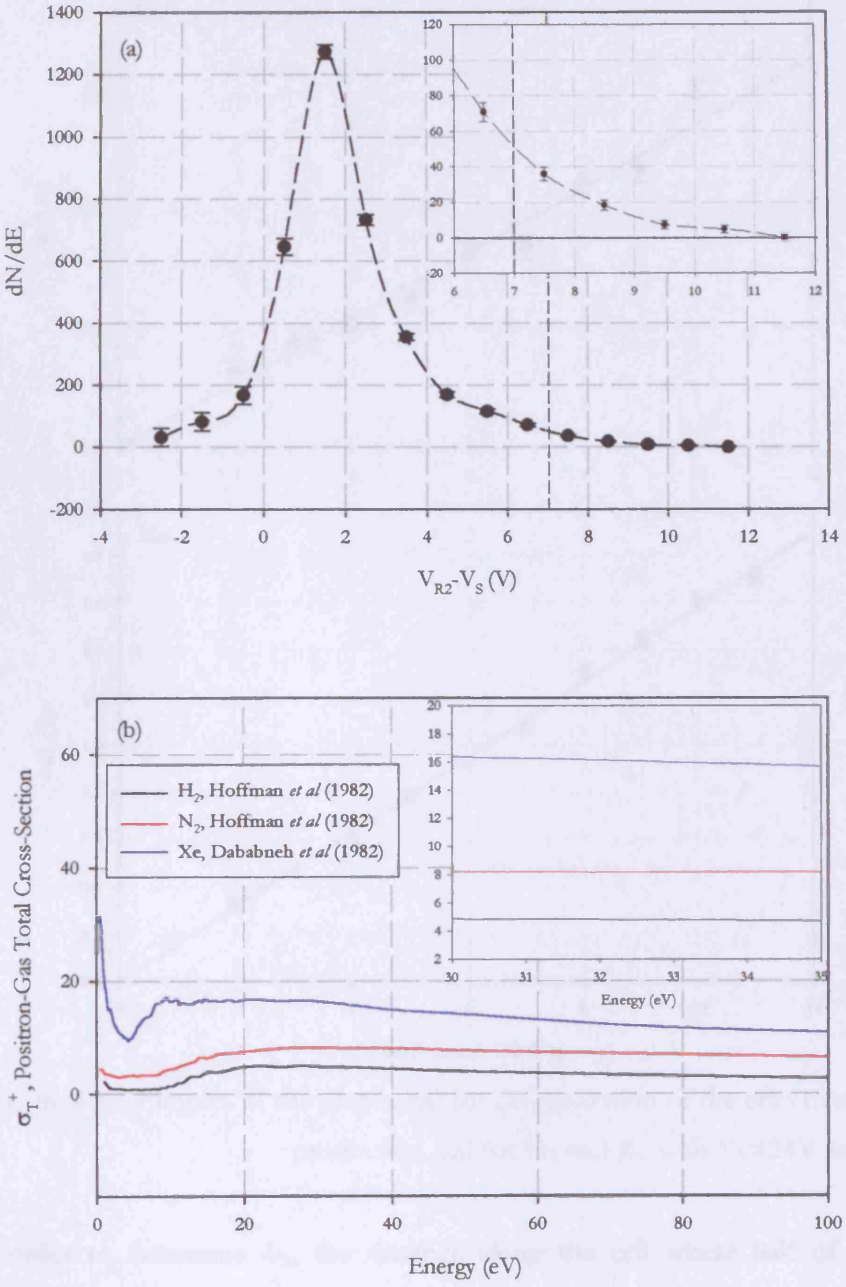

Figure 4.2 (a) An example of an energy spectrum of the positron beam (V_S=24V) and (b) relevant positron-gas total cross-section. Insets indicate the regions of interest.

Figure 4.3 shows the results obtained from positron-gas attenuation measurements over a range of pressures, p=0-11μmHg for molecular hydrogen and xenon. Such types of measurements were made for all targets under investigation in this study. As these results did not indicate any significant mass dependence, an average of the values obtained for the cell length has been taken, yielding l_+^P =(3.47±0.04)cm.

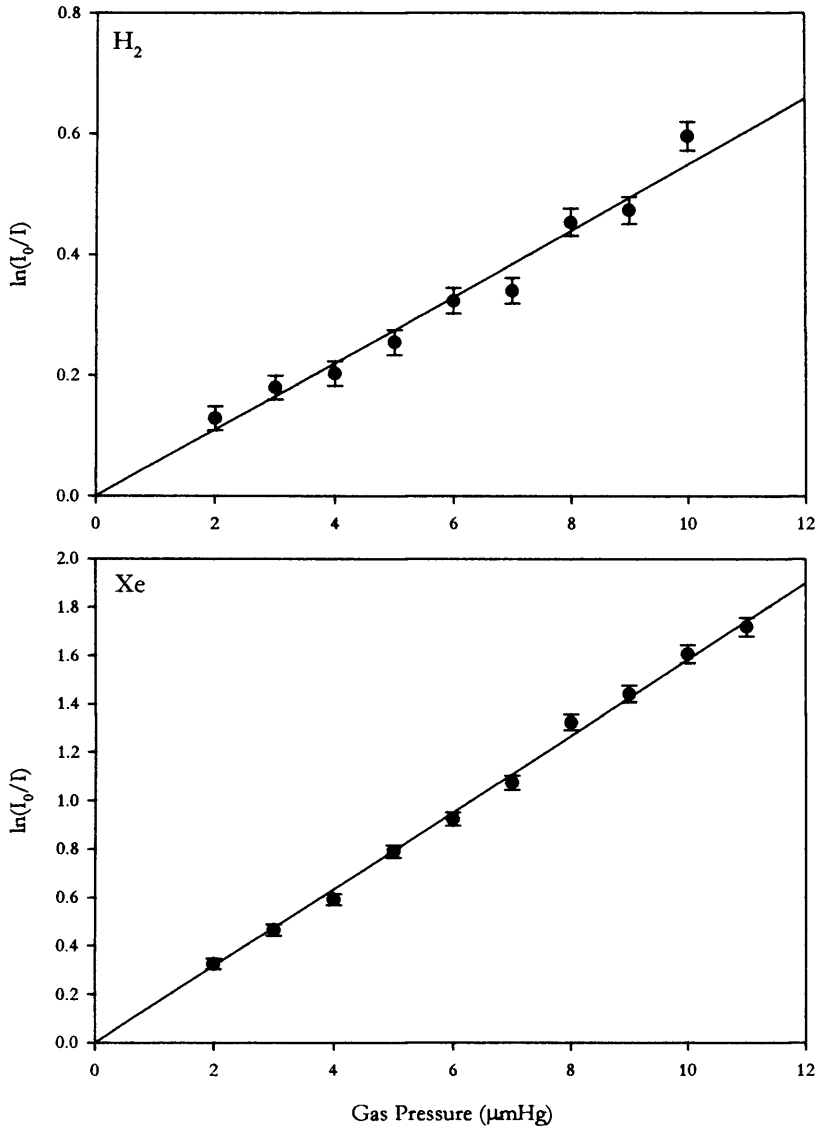

Figure 4.3 Examples of the plots used for determination of the effective length of the production cell for H_2 and Xe with Vs=24V and CR1=31V.

In order to determine l_{Ps}, the distance along the cell where half of the detected positronium atoms are formed has been calculated: this requires consideration of the variation in the detection solid angle, the fraction of positronium atoms which decay in-flight from differing points along the production cell and the fraction of positrons which scatter along the cell.

The fraction of positronium atoms $F(x)$ with kinetic energy, E_{Ps}, which survive in-flight decay to reach the detector may be written as:

$$F(x) = \exp\left(\frac{-t}{\tau}\right) = \exp\left(\frac{-16.79(D-x)}{E_{Ps}^{\frac{1}{2}}}\right), \qquad 4.5$$

where τ is the lifetime of ortho-positronium and, on the right hand side of the equation, *(D-x)* is in metres and E_{Ps} is in electronvolts.

The fraction of positrons which are transmitted through the cell is given by:

$$\frac{I}{I_0} = \left(\exp(-\rho x \sigma_T^+)\right) \tag{4.6}$$

and, therefore, the fraction per unit length which scatters within an element of length *dx*, in the limit $dx \rightarrow 0$, may be expressed as:

$$S(x) = \frac{d}{dx}\left(1 - \frac{I}{I_0}\right) = \rho\sigma_T^+ \exp(-\rho x \sigma_T^+). \tag{4.7}$$

This fraction of positrons may form collimated positronium in accordance with the differential positronium formation cross-section according to:

$$N_{Ps}(l_+^P) = \frac{1}{\sigma_T^+}\int_0^{l_+^P} \frac{d\sigma_{Ps}}{d\Omega}\Delta\Omega(x)F(x)S(x)dx. \tag{4.8}$$

In equation 4.8, $\frac{d\sigma_{Ps}}{d\Omega}$ may be assumed to be constant within the angular divergence of the positronium beam (~±1° with respect to the beam axis) and the detection solid angle, $\Delta\Omega(x)$, may be expressed as:

$$\Delta\Omega(x) = \frac{\pi r^2}{(D-x)^2}, \tag{4.9}$$

where r is the radius of the CEMA2 detector channel-plates, D is the distance from the entrance aperture of the production cell to the detector and x is the distance from the entrance aperture to where positronium is formed within the cell, so $0 \le x \le l_+^P$.

The number of collimated positronium atoms is thus:

$$N_{Ps}(l_+^P) = \frac{1}{\sigma_T^+}\frac{d\sigma_{Ps}}{d\Omega}\int_0^{l_+^P}\Delta\Omega(x)F(x)S(x)dx \tag{4.10}$$

$$= \rho\pi r^2 \frac{d\sigma_{Ps}}{d\Omega}\int_0^{l_+^P}\left[\frac{1}{(D-x)^2}\exp\left(\frac{-16.79(D-x)}{E_{Ps}^{\frac{1}{2}}}\right)\exp\left(-\rho x\sigma_T^+\right)\right]dx,$$

which may be rearranged to give:

$$N_{Ps}(l_+^P) = \rho\pi r^2 \frac{d\sigma_{Ps}}{d\Omega}\int_0^{l_+^P}\frac{1}{(D-x)^2}\exp(xB - C)dx, \tag{4.11}$$

where:

$$B = \left(\frac{16.79}{E_{Ps}^{\frac{1}{2}}} - \rho\sigma_T^+\right) \quad \text{and} \quad C = \left(\frac{16.79D}{E_{Ps}^{\frac{1}{2}}}\right). \tag{4.12}$$

In order to find the point in the cell where half the collimated positronium atoms are formed, the integral $N_{Ps}(l_+^P)$ has been evaluated numerically using:

$$N_{Ps}(l_+^P) = \int_0^{l_+^P} f(x)dx = \sum_{x=0}^{l_+^P} f(x)\Delta x \qquad 4.13$$

from *0* to l_+^P for incrementally decreasing values of Δx, until convergence was found. Hence, the value of x for which $N_{Ps}(x) = N_{Ps}(l_+^P)/2$, i.e. the point along the cell where half the collimated positronium atoms are formed, was determined for each gas studied and used to calculate l_{Ps} used in equation 4.3.

As a test of the performance of the system and method, the total cross-section for Ps-H_2 scattering determined from the variation of ε_{Ps} with target gas pressure measured in this work is shown in Figure 4.4 and found to be in broad agreement within errors with the direct σ_T^{Ps} measurements of Garner *et al* (1996). The present σ_T^{Ps} results for N_2 are also shown in the figure, where it can be seen that the indirectly determined cross-section has an average value of $(11\pm1)\times10^{-20}m^2$ in the range 30-120eV, decreasing to $(4.8\pm1.3)\times10^{-20}m^2$ by 250eV. The present results for N_2 are compared with the previous data of Leslie *et al* (2002). The reason for the discrepancy between the two sets of data is that the former assumed l_+^P to be equal to the geometric length of the body of the production cell, i.e. (2.0±0.2)cm and consequently, l_{Ps} to be half this value. The analysis in this work has found l_{Ps} to lie in the range (1.31±0.02)cm to (2.01±0.02)cm, depending on the projectile energy and production gas pressure. The latter estimation is considered more accurate.

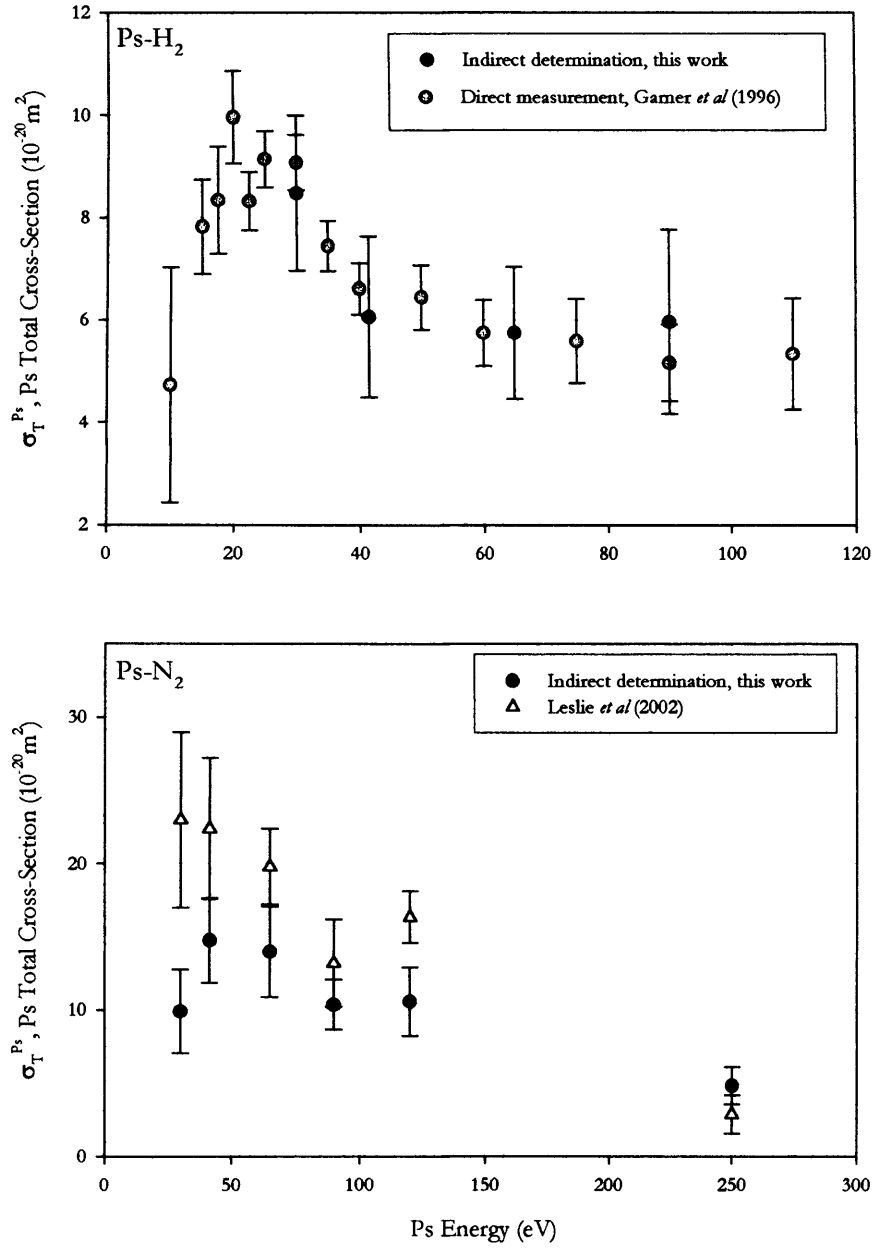

Figure 4.4 Indirect determinations of the positronium total cross-section for H_2 and N_2. A comparison is shown with direct measurements of Garner *et al* (1996) for H_2 and the previous indirect determinations of Leslie *et al* (2002) for N_2.

Indirect determinations of the positronium total cross-section have also been performed for xenon using the same method. The results are shown in Figure 4.5, where two sets of experimental data are shown arising from separate sets of measurements of the positronium production efficiency from xenon, as discussed in §3.3.3. The two data sets can be seen to yield values of σ_T^{Ps}, which are reasonably consistent.

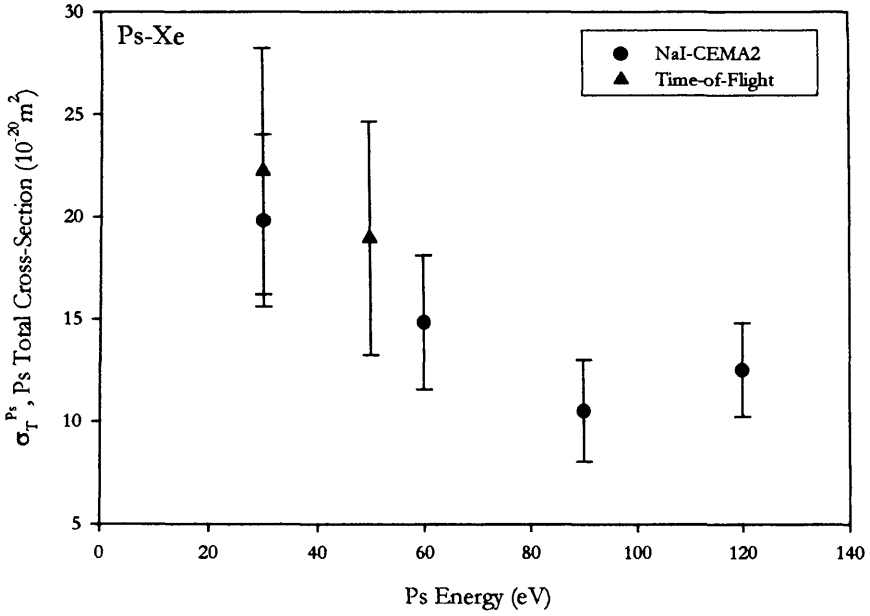

Figure 4.5 Present indirectly determined values for the positronium total cross-section for Xe from ε_{Ps} data obtained using two different methods.

4.3 Direct Determinations of the Total Cross-Section

4.3.1 Experimental Procedure

By measuring the variation in intensity of the positronium beam both with (I) and without (I_0) gas in the scattering cell, total cross-sections may be directly determined, once again, according to the Beer-Lambert law:

$$\sigma_T^{Ps} = \frac{kT}{pl_+^S} \ln\left(\frac{I_0}{I}\right), \qquad 4.14$$

where k is the Boltzmann constant, T is the ambient temperature, p the target gas pressure and l_+^S is the effective length of the scattering cell, determined using a similar method as for l_+^P, discussed above. The retarding grids CR1 and R1 were used to select the high-energy portion of the positron beam, as indicated in Figure 4.2, and positron-transmission measurements were made with the gas under investigation in the scattering cell at pressures in the range 0-12μmHg. As was the case for the measurements of l_+^P, no target dependence was seen in the measurements of l_+^S and an average value of (6.75±0.20)cm has, therefore, been determined and used in this study.

During total positronium cross-section measurements, the ambient temperature was kept constant by the air conditioning system in the laboratory to within ±1°. The gas pressure was monitored using computer software and found to be stable within ±0.5%.

At each energy investigated, a number of measurements were made over a range of pressures, typically in the range 0-6μmHg, and the weighted mean of the individual

measurements used to determine the total cross-section. The intensity of the incident positron beam was monitored before and after each positronium measurement, such that any variation could be taken into account in the analysis. Measurements of the incident positronium beam were performed using molecular hydrogen as the neutralising gas, contained in the production cell at a pressure of 10μmHg. Such measurements were made alternately with those of the positronium beam transmitted through the gas under investigation. Due to the variation in the positronium count-rate with kinetic energy, the run time varied between 300s and 3600s, in order to achieve an overall statistical uncertainty of ±5%.

For this work, the apertures of the scattering cell were replaced with those shown in Figure 4.6. These apertures were made from lead so as to provide additional shielding of gamma-rays from the detectors, thereby reducing contributions to the background signal which arise from positrons annihilating prior to the cell, as well as the 1.28MeV gamma-rays from the ^{22}Na source.

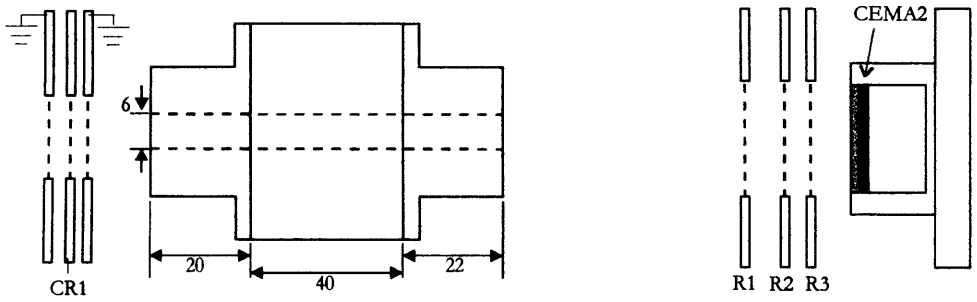

Figure 4.6 Schematic diagram of the scattering cell (dimensions in mm).

During measurements of the positronium-gas total cross-section, the cell retarder CR1 was set such that any residual slow positron exiting the production cell without forming positronium was repelled to prevent it from entering the scattering cell. Similarly, the retarding grid R1 in front of the detector (CEMA2) was used to repel any positron resulting from positronium fragmentation upon impact on the gas in the scattering cell prior to the detector or any surface along its way. It is essential that the potential applied to R1 is greater than that applied to CR1, as otherwise, a significant signal can arise from positronium which fragments in the region between CR1 and the earth grid: the residual positrons being accelerated towards the detector by the positive potential applied to CR1. It is essential that R1 must be used to repel such positrons prior to detection.

4.3.2 Results

i) Molecular Hydrogen

Once again, as a general check on the performance of the system, the total cross-section for positronium scattering from molecular hydrogen was measured using the NaI-CEMA2 coincidence detection system with an angular acceptance of (1.10±0.01)°. Figure 4.7 shows the direct measurements of the positronium total cross-section from molecular hydrogen, along with the indirectly determined values shown previously in Figure 4.4, to be in good agreement with the previous measurements of Garner *et al* (1996). Also shown in the figure are the extrapolated values of Garner *et al* (2000), which measured the effects of forward angle scattering on σ_T^{Ps} for molecular hydrogen. Garner *et al* (2000) evaluated this effect by measuring σ_T^{Ps} over a range of detection solid angles and extrapolating to 0msr to determine the 'true' value of the cross-section.

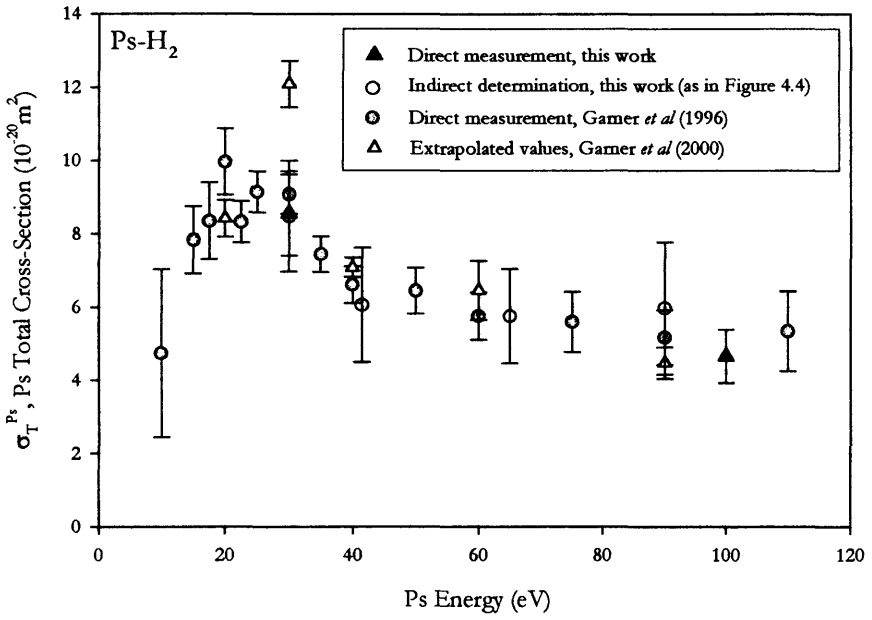

Figure 4.7 Experimental determinations of the total cross-section for positronium scattering from H_2.

ii) Molecular Nitrogen

Values of the total cross-section for positronium scattering from molecular nitrogen have been obtained in the energy range 10-130eV using the NaI-CEMA2 coincidence detection system with a positronium detection solid angle of 1.15msr, corresponding to a beam angle of ±(1.10±0.01)°. Following the work on the forward scattering of positronium atoms by Garner *et al* (2000) mentioned in §4.3.2i, additional measurements were made for molecular nitrogen using the CsI-CEMA2 coincidence detection system, which enables the flight-length and, hence, acceptance angle to be altered. Measurements were made for an incident positronium

energy of 30eV over a range of solid angles from 1.16 to 9.51msr (1.10° to 3.15°) and yielded values which were consistent within errors, showing no significant effect of forward scattering. Garner *et al* (2000) extracted the 'true' total cross-section, σ_T, using:

$$\frac{kT}{pL}\ln\left(\frac{I_0}{I_m}\right)=\sigma_T-\left\langle\frac{d\sigma}{d\Omega}\right\rangle\Delta\Omega, \qquad 4.15$$

where I_m/I_0 is the measured beam attenuation at a given solid angle $\Delta\Omega$ and $\langle d\sigma/d\Omega\rangle$ is an average of the differential scattering cross-section with respect to any process which results in the scattering of the projectile in the range 0 to $\Delta\Omega$. In their study, Garner *et al* (2000) saw the largest effect in argon in the region 20-60eV where, measurements over the same angular range as in this work, showed a decrease of ~10% in measured total cross-section with $\Delta\Omega$. The CsI-CEMA2 measurements in this study shown in Figure 4.8 suggest that, at E_{Ps}=30eV, the effects of forward scattering are negligible for Ps-N_2 interactions, over the angular range investigated.

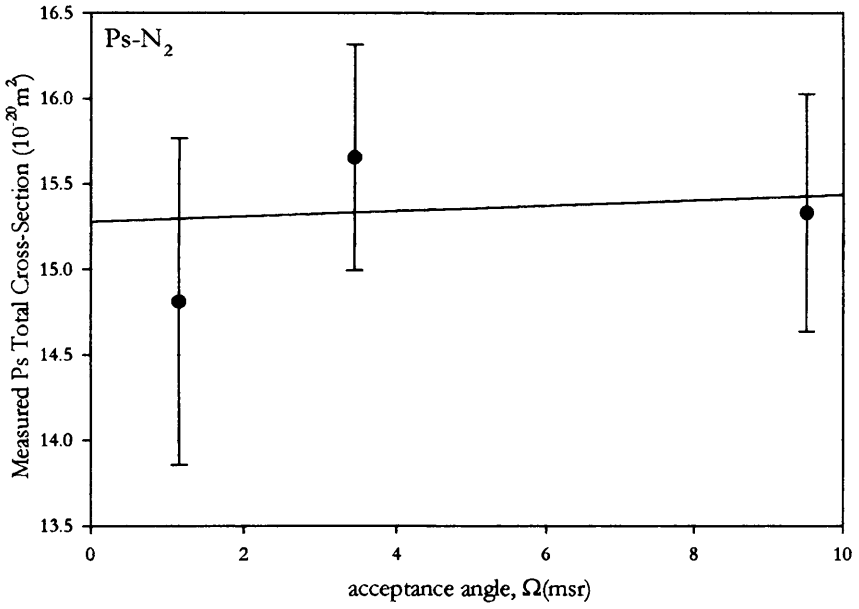

Figure 4.8 Total cross-section for positronium scattering from N_2 measured using the CEMA2-CsI detection system for acceptance angles in the range 1.16-9.51msr.

Figure 4.9 shows the direct measurements of the total cross-section along with the extrapolated value from the data shown in Figure 4.8 and the indirect determination shown in Figure 4.4, whereby good consistency is seen between these sets of data. There is currently no theoretical calculation available for comparison.

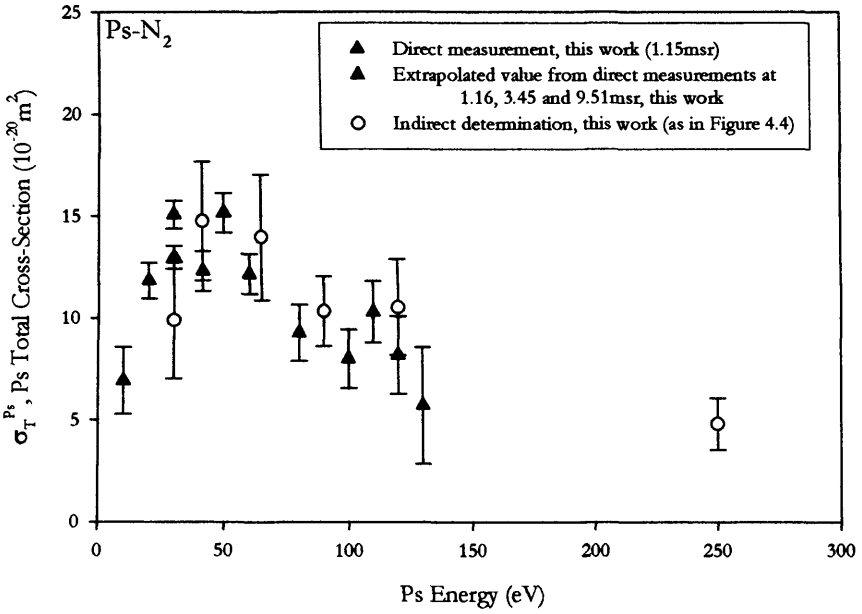

Figure 4.9 Total cross-section for positronium scattering from N_2.

iii) Xenon

Direct measurements of the total cross-section for positronium scattering from xenon in the energy range 10-100eV have been made using the NaI-CEMA2 coincidence detection system, as described in §2.7.2. These results are shown in Figure 4.10 and are compared with the indirectly determined values, shown previously in Figure 4.5. Also shown in the figure is a weighted mean of the direct and indirect values. The theoretical prediction of Blackwood *et al* (2002) shown is that of the Ps-Xe elastic cross-section, calculated using the static exchange approximation. In this approximation, results become unreliable above the first inelastic threshold as flux is not conserved. Below the first inelastic threshold, however, the calculation suggests an increase in the cross-section with decreasing energy, which is a trend that is not inconsistent with the present experimental data. However, the poor precision of the experimental datum at low energies prevents a definite conclusion in this respect.

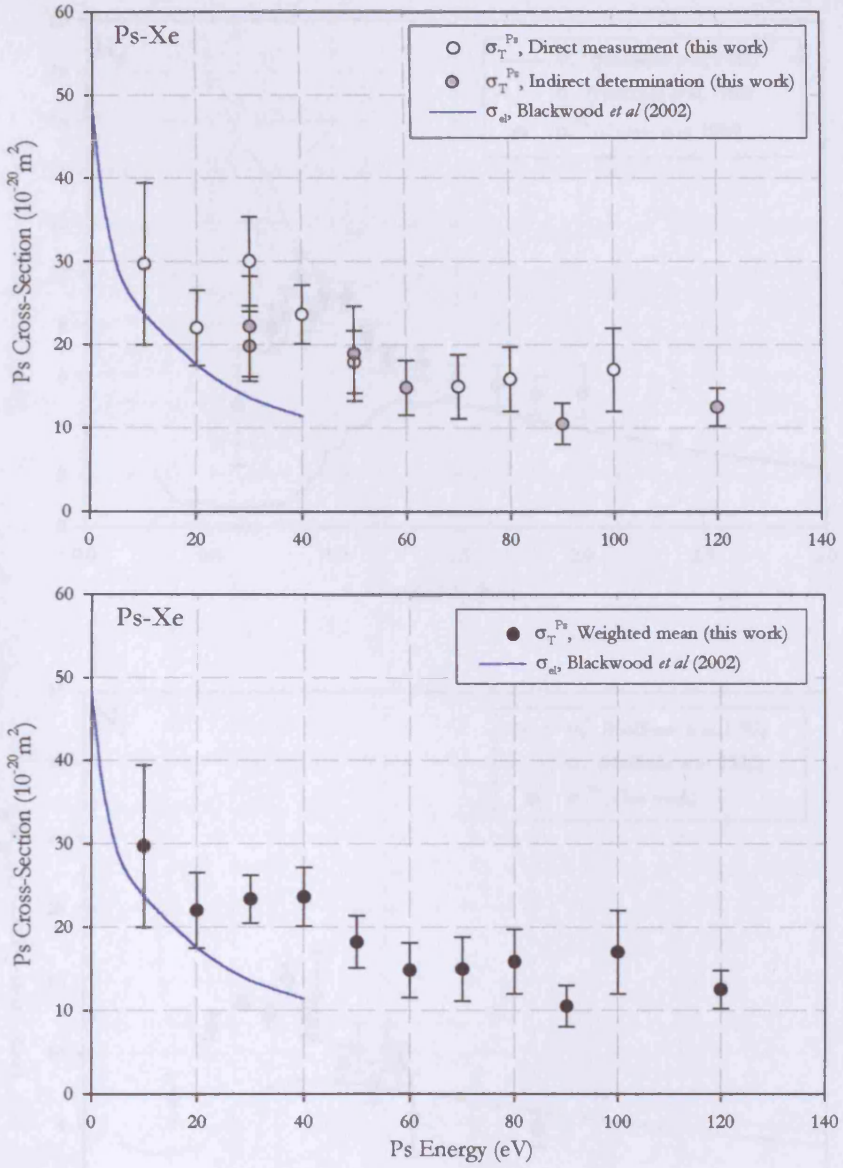

Figure 4.10 Theoretical (line) and experimental (points) determinations of the positronium cross-section from Xe.

4.4 Discussion

4.4.1 Molecular Hydrogen and Nitrogen

Figure 4.11 compares the measurements of the positronium total cross-sections for H_2 and N_2 with equivelocity electrons and positrons (Hoffman *et al*, 1982). The H_2 data for positronium are those of Garner *et al* (1996) and those for N_2 are the weighted means of the present (direct and indirect) determinations, as in Figure 4.9. For H_2, in the region of 0.5a.u the electron total cross-section (σ_T^-) is ~20 times higher than that of the positron (σ_T^+). σ_T^+ increases rapidly after the positronium formation threshold (at ~0.8a.u), approaching and

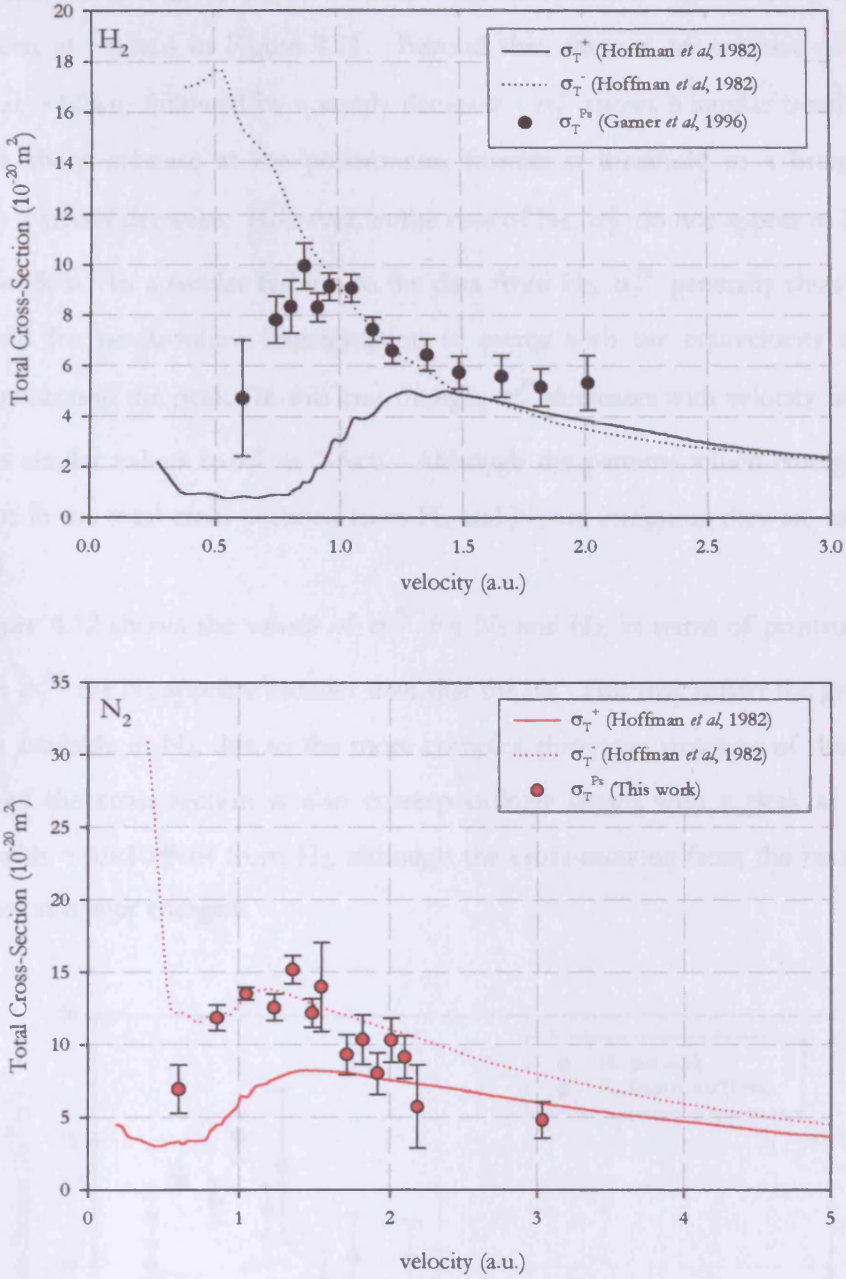

Figure 4.11 Total cross-sections for equivelocity positron, electron and positronium scattering from H_2 and N_2.

merging with σ_T^- at around 1.5a.u. The positronium total cross-section (σ_T^{Ps}) shows a rapid increase from ~0.6a.u., near the opening of the channel for positronium fragmentation. This rise continues to a broad maximum followed by a decrease in σ_T^{Ps}, and a merging with σ_T^- from around 1a.u. Above 1.5a.u, σ_T^{Ps} is on average, ~20% higher than $\sigma_T^{\pm}$.

In the case of N_2, σ_T^- exhibits a shape resonance at low velocities, the decrease from which is seen at ~0.5a.u in Figure 4.11. Beyond this, there is an increase of ~20%, to a maximum at ~1.2a.u, followed by a steady decrease. σ_T^+ shows a similar trend to that seen from H_2: a sharp increase at the positronium formation threshold to a broad maximum, followed by a steady decrease. However, in the case of N_2, $\sigma_T^\pm$ do not appear to have merged, even beyond 5a.u. In a similar fashion to the data from H_2, σ_T^{Ps} generally shows a rise from the threshold for positronium fragmentation to merge with the equivelocity electron total cross-section around the peak. In this case though, σ_T^{Ps} decreases with velocity faster than σ_T^- and reaches similar values to σ_T^+ at 2-3a.u. Although the patterns which emerge from these comparisons in the total cross-sections from H_2 and N_2 are intriguing they are as yet not fully understood.

Figure 4.12 shows the values of σ_T^{Ps} for N_2 and H_2, in terms of positronium energy. The peak in σ_T^{Ps} for N_2 appears broader than that for H_2. This may reflect the greater number of channels available in N_2, due to the more complex electronic structure of this target. The magnitude of the cross-section is also correspondingly larger; with a peak at ~$15\times10^{-20}m^2$ compared with ~$10\times10^{-20}m^2$ from H_2, although the cross-sections from the two targets have similar values at higher energies.

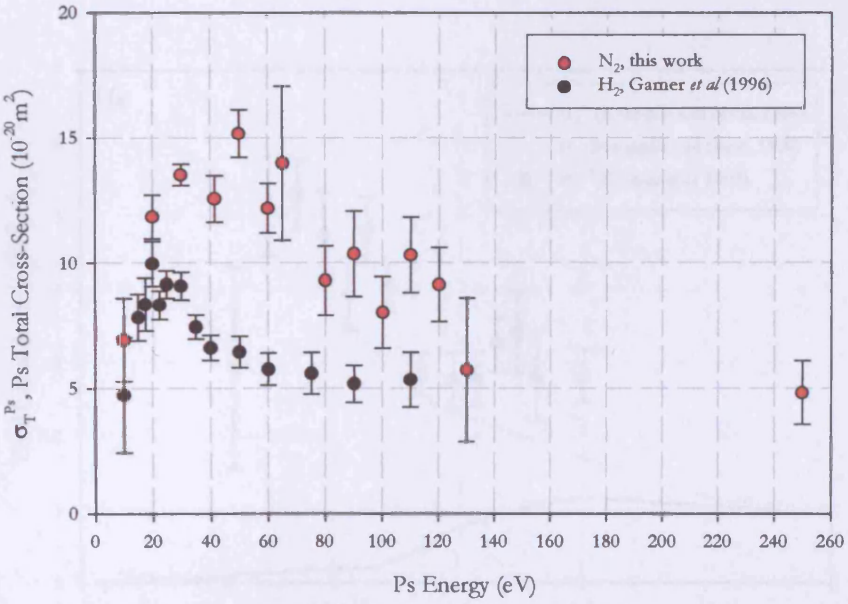

Figure 4.12 Comparison of total cross-sections for positronium scattering from H_2 and N_2.

4.4.2 Xenon

Figure 4.13 shows a comparison of the positronium total cross-section from xenon with the corresponding equivelocity positron and electron data ($\sigma_T^{\pm}$, Dababneh *et al*, 1982). σ_T^- exhibits a shoulder in the region of ~0.7-1.3a.u (the first maximum at ~0.75a.u being due to atomic excitation), which is followed by a rapid decrease which brings it to a value close to that of σ_T^+ at ~1.8a.u. As seen for H_2 and N_2, σ_T^+ shows an increase at the positronium

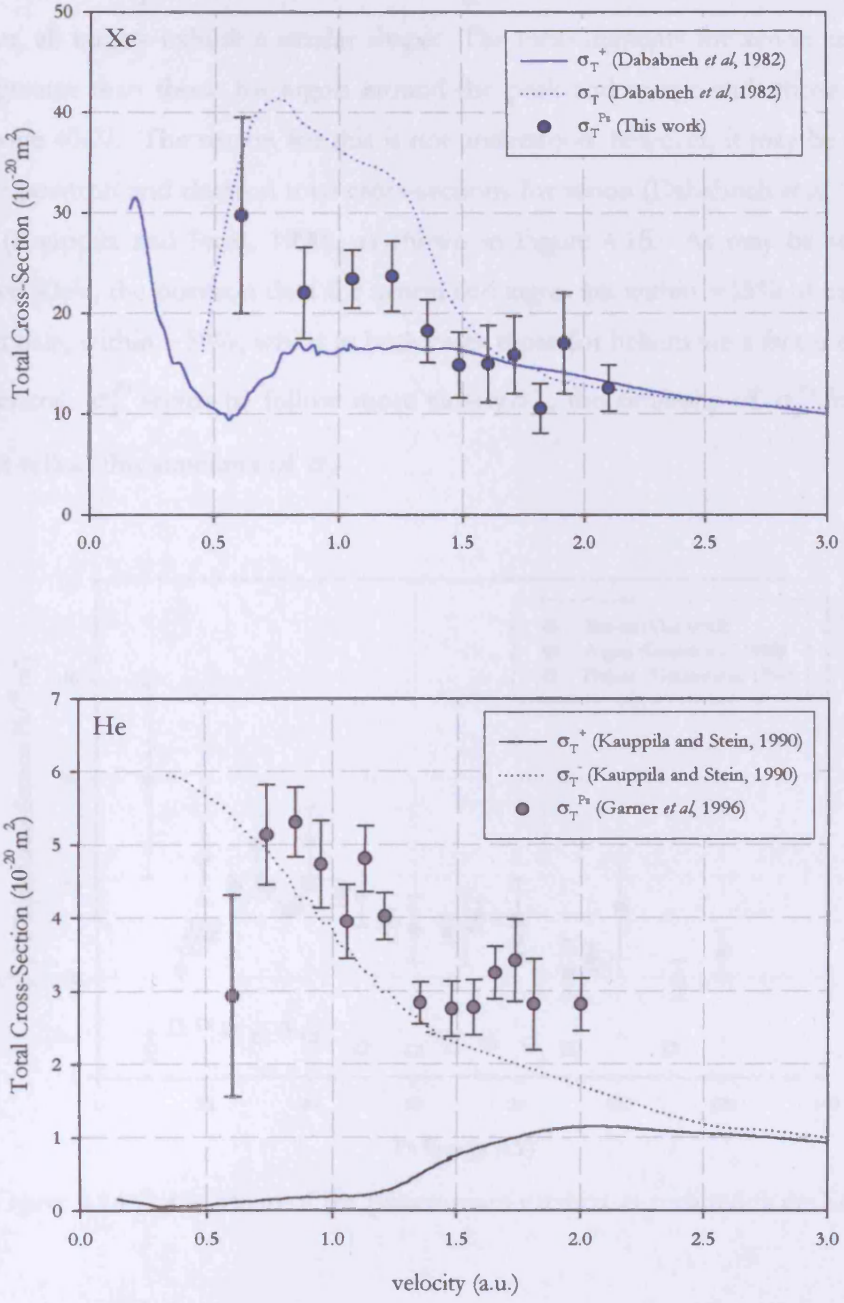

Figure 4.13 Total cross-sections for equivelocity positron, electron and positronium scattering from Xe and He.

formation threshold (~0.6a.u) to a broad peak and begins to slowly decrease beyond ~1.5a.u. The positronium total cross-section (σ_T^{Ps}) from xenon lies between that of the positron and electron, until they all become approximately equal at around 1.6a.u. The corresponding helium data are also shown in the figure where σ_T^{Ps} can be seen to exhibit a trend similar to that for H_2, that is it follows the shape of the electron cross-section, although exceeding it by ~25% on average.

Figure 4.14 shows a comparison of the positronium total cross-sections from xenon, argon and helium. Apart from the lowest energy datum for xenon, which requires further investigation, all targets exhibit a similar shape. The measurements for xenon are on average only 20% greater than those for argon around the peak and merge with those for argon at energies above 40eV. The reason for this is not understood, however, it may be of interest to examine the positron and electron total cross-sections for xenon (Dababneh *et al*, 1982), helium and argon (Kauppila and Stein, 1990), as shown in Figure 4.15. As may be seen from the figure, above 40eV, the positron data for xenon and argon are within ~15% of each other and the electron data, within ~50%, whilst in both cases those for helium are a factor of ~10 lower. Since, in general, σ_T^{Ps} seems to follow more closely σ_T^-, the similarity of σ_T^{Ps} for xenon and argon might reflect this similarity of σ_T^-.

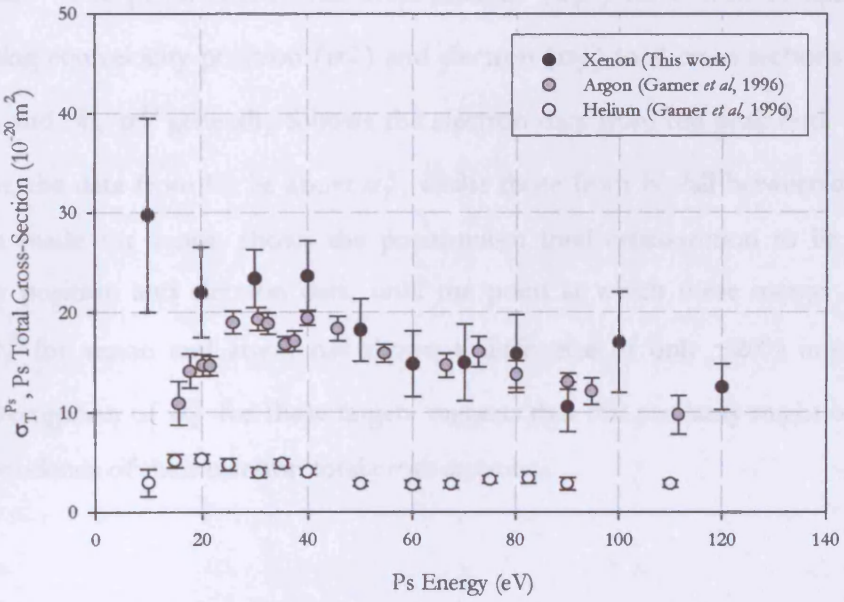

Figure 4.14 Comparison of the positronium total cross-sections from Xe, Ar and He.

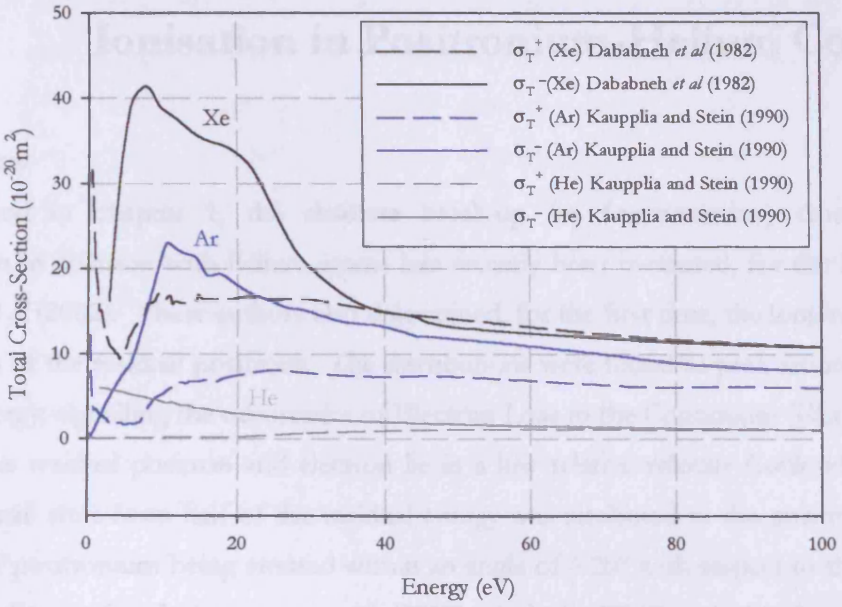

Figure 4.15 Comparison of the positron and electron total cross-sections from Xe, Ar and He.

4.5 Summary

The positronium total cross-sections from molecular hydrogen, molecular nitrogen and xenon have been determined directly and indirectly. Good agreement has been found between the two methods. The positronium total cross-sections (σ_T^{Ps}) have been compared with the corresponding equivelocity positron (σ_T^+) and electron (σ_T^-) total cross-sections. In the case of both H_2 and N_2, σ_T^{Ps} generally follows the electron data from the peak until ~1.5a.u, after which point, the data from H_2 lie above $\sigma_T^{\pm}$, whilst those from N_2 fall between $\sigma_T^{\pm}$. A similar comparison made for xenon shows the positronium total cross-section to lie between the equivelocity positron and electron data, until the point at which these merge. Comparison between σ_T^{Ps} for xenon and argon has shown a difference of only ~20% around the peak region. Investigation of $\sigma_T^{\pm}$ for these targets suggests that this similarity might originate from the correspondence of their electron total cross-sections.

Chapter 5
Ionisation in Positronium-Helium Collisions

5.1 Overview

As discussed in chapter 1, the absolute break-up (or fragmentation) cross-section of positronium in collision with helium atoms has recently been measured, for the first time, by Armitage *et al* (2002). These authors also determined, for the first time, the longitudinal energy distribution of the residual positrons. The distributions were found to peak around half of the residual energy, signalling the occurrence of Electron Loss to the Continuum (ELC, see §1.6.3), in which the residual positron and electron lie in a low relative-velocity Coulomb continuum state. A small shift from half of the residual energy was attributed to the positrons from the break-up of positronium being emitted within an angle of $\approx 20°$ with respect to the beam axis. Following the work of Armitage *et al* (2002), Sarkadi (2003) calculated the integrated fragmentation cross-section and the longitudinal energy distributions of both the residual positrons and electrons using a classical trajectory Monte Carlo (CTMC) calculation. Whilst this calculation yielded an integrated cross-section which was a factor of ~1.6 higher than the experimental results, the shape of the longitudinal energy distributions of the residual positrons were found to be very close to those measured. An asymmetry has been predicted by this theory between the energy distributions of the two residual particles and remains, as yet, untested.

In the experiment of Armitage *et al* (2002), a time-of-flight detection system was employed which enabled a stringent verification of the origin of the signal. However a different method of measurement is required to detect electrons both at high and low energies. The low energy electrons are expected to dominate the target ionisation spectrum but, in the time-of-flight spectrum, would be lost in the background. At higher energies, the energy resolution of the time-of-flight system gets progressively poorer and hinders extraction of the electron energy spectra. In this study, a different method to that employed by Armitage *et al* (2002) has been developed with the aim of investigating, eventually, the spectra of ejected electrons in these two energy regimes. The method is first tested by measuring the spectra of the positrons emitted following positronium-helium collisions and then applied to the detection of electrons. In the case of positron measurements, good agreement with the data of Armitage *et al* (2002) is found. Initial investigations with electrons have shown these measurements to be much more challenging due to the high level of the background. Despite this, some progress has been made and results will be presented. The method employs a retarding field analyser (RFA) to determine both the integrated break-up cross-section and the

longitudinal energy of the positrons and of the electrons. This technique yields results directly without the need to estimate the various partial flight times of the positron/electron/ positronium atom along the path, all of which introduce additional uncertainties, as discussed in chapter 3. The method also benefits from higher count-rates, as no remoderation of the incident positron beam is required. In the case of positrons, measurements have been made using the NaI-CEMA2 coincidence detection system (described in §2.7.2) and for electrons, due to the absence of a correlated gamma-ray signal, the CEMA2 counts have been used. The absence of a correlated signal makes the latter measurements much more sensitive to background levels. Data have been obtained for positrons released following positronium impact on helium at energies of 18, 33 and 60eV. The lower energies were also studied by Armitage *et al* (2002) with which the present data are in accord. Preliminary investigations have been performed to detect the corresponding ejected electrons.

There are two separate sections in this chapter: **I.** Detection of the residual positrons and **II.** Detection of the electrons. These sections detail the experimental method employed and results obtained in each part of the study of ionisation in positronium-helium collisions. In the conclusion (**III**), the main results from the two sections are summarised and discussed. Suggestions are made on how to advance further these studies.

I. Detection of the residual positrons

I.1 Experimental Method

Figure 5.1 shows a schematic diagram of the positronium scattering region. Molecular hydrogen at a pressure of 10μmHg was used as the positronium beam production gas throughout this study. The incident positronium beam from the production cell enters the scattering cell and may break-up on the target gas which, in this work, was helium at a pressure in the range 0-7μmHg.

Positrons released from the fragmentation of positronium are confined to helical trajectories in the **B**-field, with a Larmor radius which depends on their velocity and emittance angle. Armitage (2002) made measurements of the residual positron yield with varying **B**-field, to ensure that all positrons from positronium fragmentation were extracted from the scattering cell. Although no significant variation was seen by Armitage (2002) at 13 and 18eV, it was found that at the two higher energies studied, 25 and 33eV, a higher positron yield was

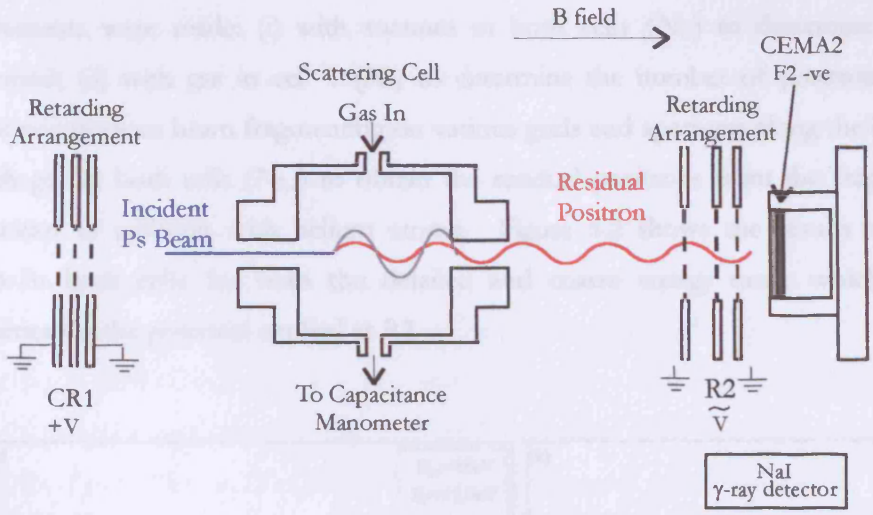

Figure 5.1 Potentials applied to the electrostatic elements during measurements of the residual positrons.

achieved with increasing **B**-field, saturating at 15.7mT. The same magnetic field has been used in this study.

The polarity of the potentials applied to the various electrostatic elements for the measurements of the residual positrons are indicated in Figure 5.1. A potential is applied to CR1 in order to prevent any residual positrons leaving the production cell from entering the scattering cell. The grid R2 in front of CEMA2 is grounded when measuring the total flux of residual positrons plus transmitted positronium atoms and positively biased when measuring the flux of transmitted positronium atoms only. The yield of positrons from positronium fragmentation may then be obtained by subtraction. Discussed in the following sections are the measurements required to obtain the yield of positrons from the fragmentation of positronium. Data were obtained using a PC-based multi-channel analyser (MCA) to record coincidences between the NaI detector and CEMA2 (see §2.7.2). All errors on the count-rates shown include the uncertainty in the pressure (±0.5%) and in the positron beam flux (±0.5%). Measurements have been made over two ranges of V_{R2}: (i) for the determination of the energy differential break-up cross-section, detailed measurements have been made of positrons with energies below the residual energy, whilst (ii) a larger energy range and step has been employed to measure the integrated break-up cross-section. These measurements, not always taken under identical conditions, are shown alongside each other in the following section.

I.2 Results

In order to measure the number of positrons from the fragmentation of positronium and to determine the longitudinal energy distribution of these residual positrons, a variable positive potential was applied to the grid R2 in front of CEMA2, as shown in Figure 5.1.

Measurements were made: (i) with vacuum in both cells (N_V) to determine the vacuum background; (ii) with gas in cell 1 (N_1) to determine the number of positrons due to the incident positronium beam fragmenting on various grids and apertures along the beamline; and (iii) with gas in both cells ($N_{1,2}$) to obtain the residual positrons from the fragmentation of positronium in collision with helium atoms. Figure 5.2 shows the results obtained with vacuum in both cells for both the detailed and coarse energy range which indicate no dependence on the potential applied at R2.

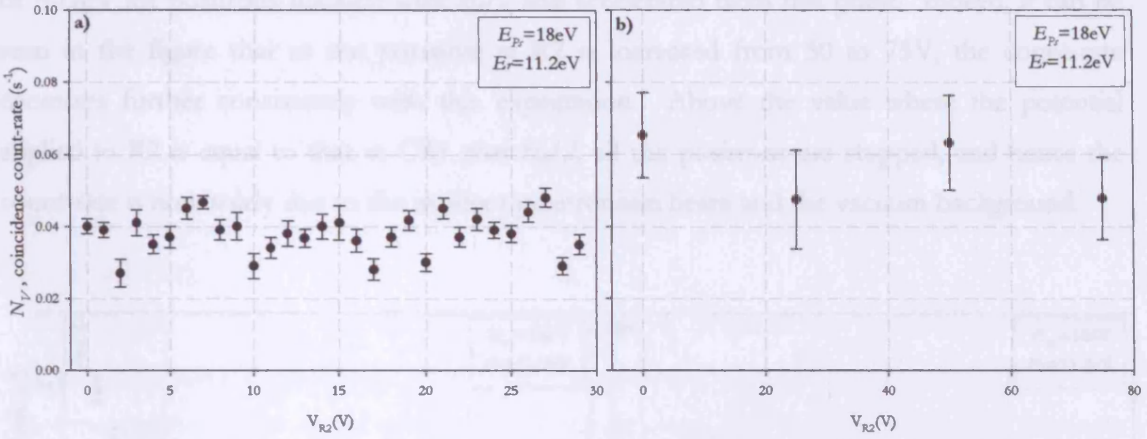

Figure 5.2 An example of background measurements made with vacuum in both cells: a) detailed measurements; b) larger energy range and step.

In order to confirm that the background does not change with gas in the production cell, time-of-flight spectra have been measured with vacuum in both cells (background) and gas in cell 1 (gas). An example of these spectra is shown in Figure 5.3 along with the subtraction of these signals, which indicates that the only net signal is that due to the incident positronium.

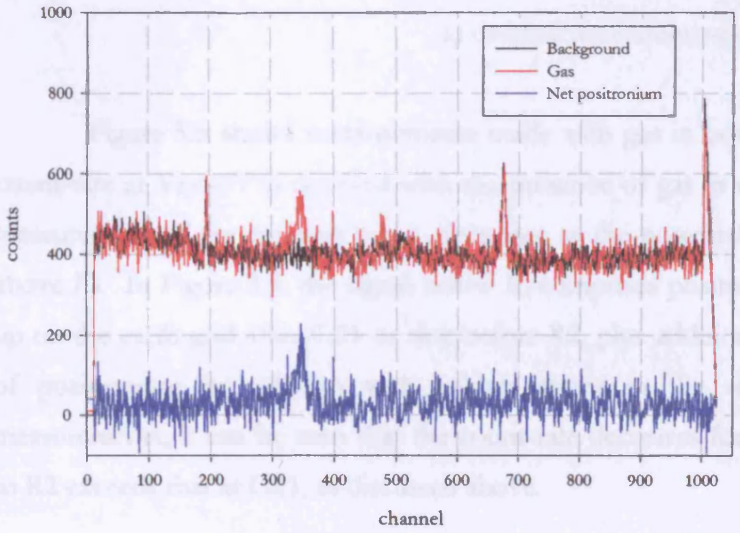

Figure 5.3 Time-of-flight spectra of the 'background', 'gas' and 'net positronium' signals.

An example of the measurements obtained with gas in the production cell is shown in Figure 5.4. The counts measured at energies below E_r (see §1.6.3) arise from the break-up of positronium on the earth grids after CR1 or in front of R2, or on the apertures of the scattering cell. Above E_r, the signal becomes flat and is due to the signal from the incident positronium beam and vacuum background (N_V) only. Given that positronium may break-up on any grid or aperture, a signal would also be expected at higher energies corresponding to positrons released at CR1 and accelerated by the positive potential applied to this grid. In the coarse measurements shown below, the potential applied at CR1 was 65V, corresponding to an energy of ~71eV for positrons released with $E_r/2$ and accelerated from this point. Indeed, it can be seen in the figure that as the potential at R2 is increased from 50 to 75V, the count-rate decreases further consistently with this expectation. Above the value where the potential applied to R2 is equal to that at CR1 plus $E_r/2$, all the positrons are stopped, and hence the count-rate is now solely due to the incident positronium beam and the vacuum background.

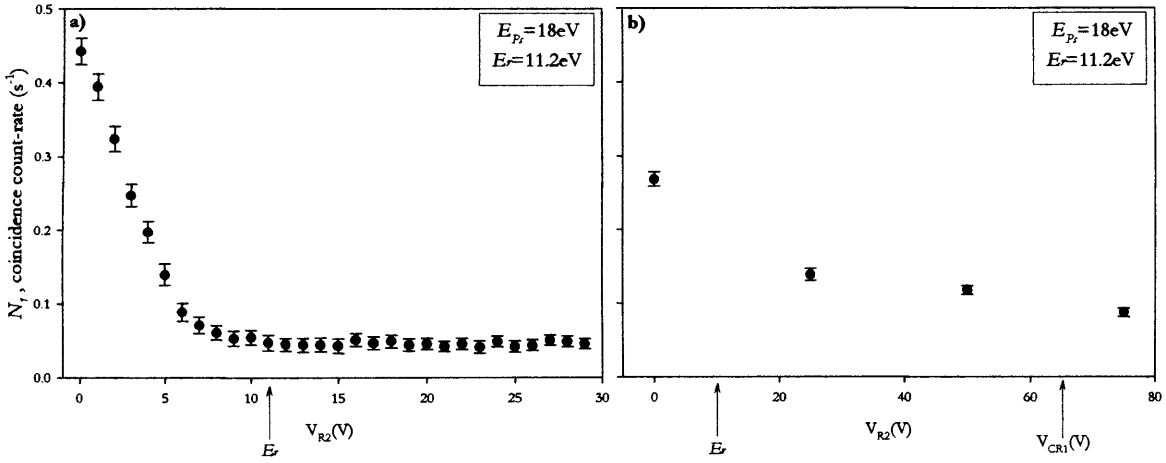

Figure 5.4 An example of positron measurements with gas in the production cell: a) detailed measurements; b) larger energy range and step.

Figure 5.5 shows measurements made with gas in both cells ($N_{1,2}$). The coincidence count-rate at V_{R2}=0V is doubled with the presence of gas in cell 2 and, as seen before in the measurement of the incident beam, decreases as the potential at R2 is increased from 0V to above E_r. In Figure 5.5, the signal below E_r comprises positrons from positronium breaking-up on the earth grid after CR1 or that before R2, plus additional positrons from the break-up of positronium in collision with helium atoms in the scattering cell. In the coarse measurements, it can be seen that the count-rate decreases further when the potential applied to R2 exceeds that at CR1, as discussed above.

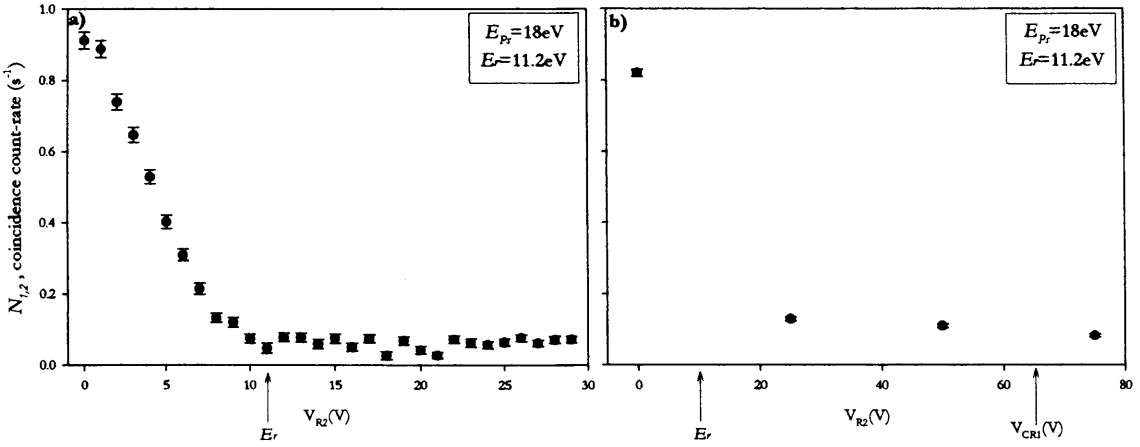

Figure 5.5 An example of positron measurements with gas in both cells: a) detailed measurements; b) larger energy range and step.

Above this point, the signal is due to the transmitted positronium beam and the vacuum background only.

Figure 5.6 shows the net signal ($N_{net}=N_{1,2}-N_1$) obtained for both the detailed and coarse energy step measurements. Fair consistency is found between the two sets of data, both indicating a net positive signal of similar magnitude corresponding to the residual positrons from positronium break-up.

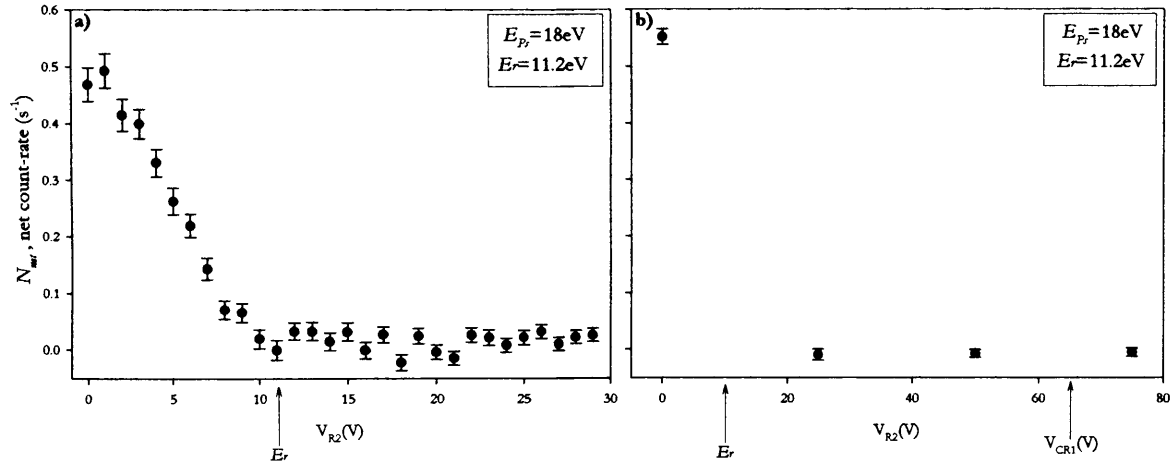

Figure 5.6 An example of the net signal from residual positrons in the case of both a) detailed and b) coarse energy step measurements.

Corresponding measurements to those presented in Figures 5.4 to 5.6 have been made at E_{Ps}=33 and 60eV and have been used to determine both the energy differential and integrated break-up cross-section for positronium in collision with helium atoms, as discussed in the following sections.

I.3 Analysis

I.3.1 Energy Differential Break-Up Cross-Section

The energy spectrum of positrons from positronium break-up, i.e.:

$$\left(\frac{dN_+(E_+)}{dE_+}\right)=\left(\frac{dN_{1,2}(E_+)}{dE_+}\right)-\left(\frac{dN_1(E_+)}{dE_+}\right), \qquad 5.1$$

is shown in Figure 5.7 for positronium energies of 18, 33 and 60eV. The arrows indicate $E_r/2$, where $E_r = E_{Ps}$ - 6.8eV is the residual energy of the system, 6.8eV being the positronium binding energy.

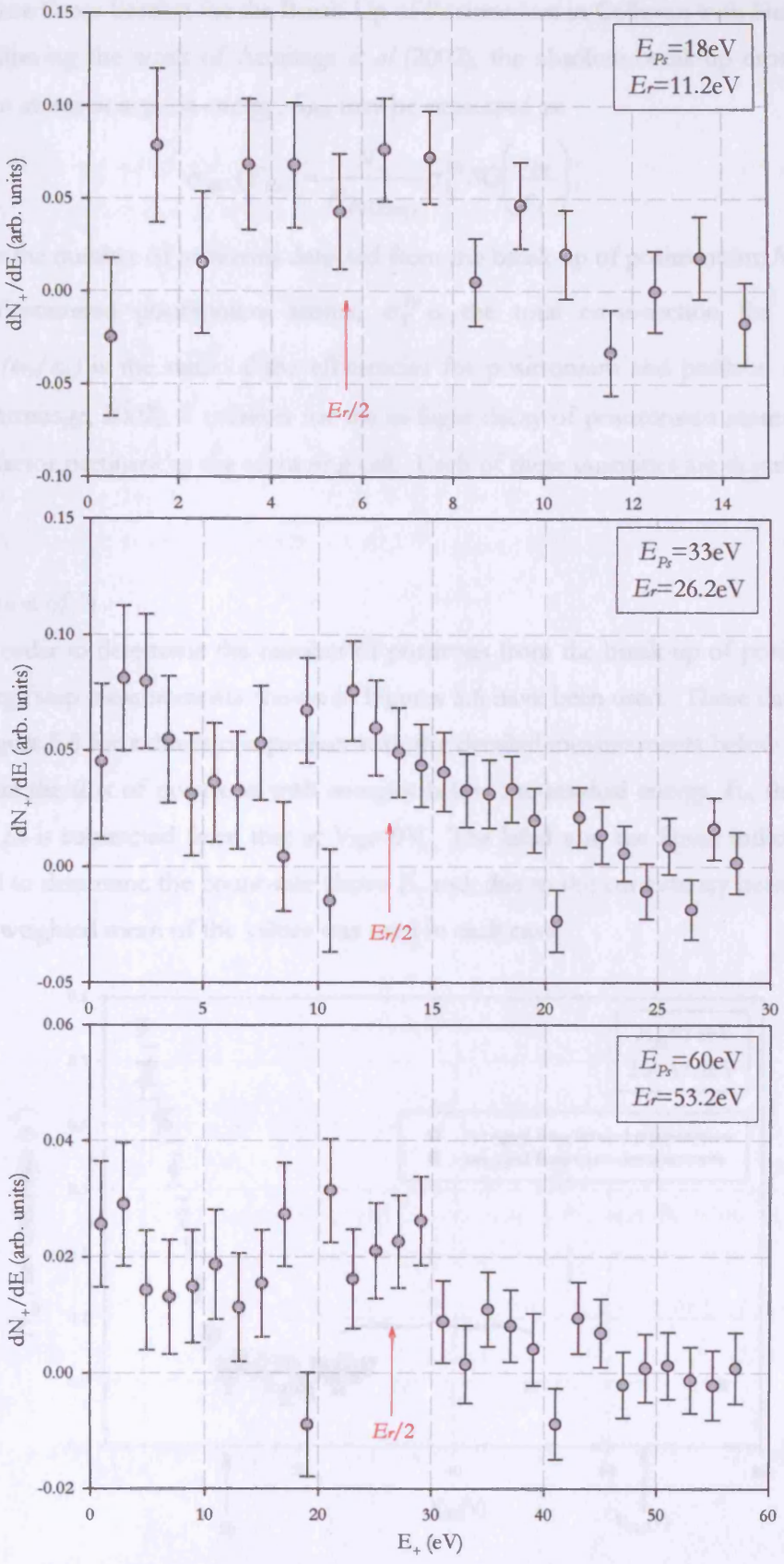

Figure 5.7 Results of $\left(\frac{dN_+(E_+)}{dE_+}\right)$ for E_{Ps}=18, 33 and 60eV.

I.3.2 Absolute Cross-Section for the Break-Up of Positronium in Collision with Helium Atoms

Following the work of Armitage *et al* (2002), the absolute break-up cross-section of positronium atoms at a given energy, E_{Ps}, may be expressed as:

$$\sigma_{BU}(E_{Ps}) = \frac{N_+}{N_{Ps(scatt)}} \sigma_T^{Ps} SG \left(\frac{\varepsilon_{Ps}}{\varepsilon_+} \right), \qquad 5.2$$

where N_+ is the number of positrons detected from the break-up of positronium; $N_{Ps(scatt)}$ is the number of scattered positronium atoms; σ_T^{Ps} is the total cross-section for positronium scattering; $(\varepsilon_{Ps}/\varepsilon_+)$ is the ratio of the efficiencies for positronium and positron detection by CEMA2 (Armitage, 2002); S corrects for the in-flight decay of positronium atoms; and G is a geometric factor pertinent to the scattering cell. Each of these quantities are described in detail below.

Determination of N_+

In order to determine the number of positrons from the break-up of positronium, the coarse energy step measurements shown in Figures 5.6 have been used. These data are shown again in Figure 5.8 for a direct comparison with the detailed measurements below E_r. In order to determine the flux of positrons with energies below the residual energy, E_r, the net count-rate above E_r is subtracted from that at V_{R2}=0V. The label **a** in the figure indicates the data points used to determine the count-rate above E_r and, due to the consistency between the data points, the weighted mean of the values was used in each case.

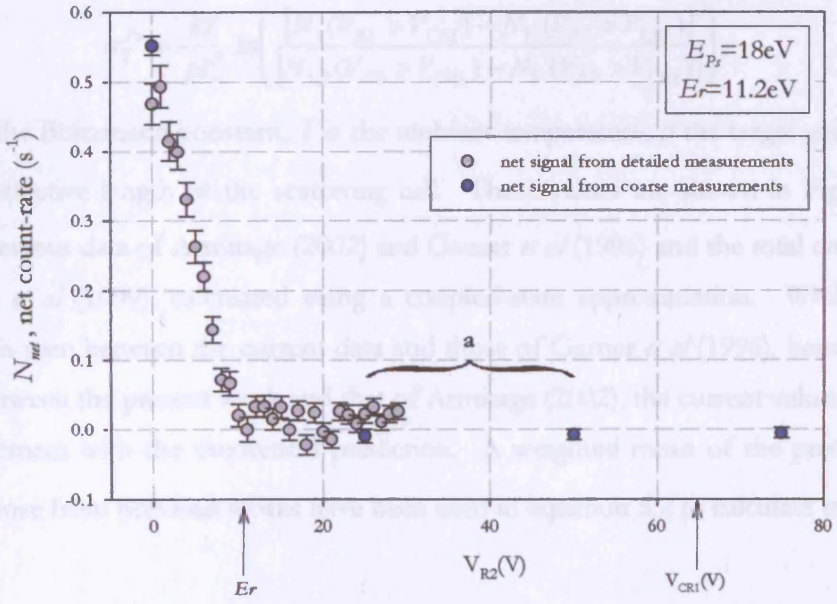

Figure 5.8 Summary of the net positron signals shown previously in Figures 5.6.

The total number of positrons from positronium break-up, N_+, has been obtained from the net count-rates, N_{net}, over the coarse energy range, as follows:

$$N_+ = N_{net}(0) - N_{net}(a), \tag{5.3}$$

where the values in parentheses indicate the potential applied at R2 and $N_{net}(a)$ is the weighted mean values of the data points in the flat region, indicated in Figure 5.8.

Determination of $N_{Ps(scatt)}$

Comparison of the signal obtained with and without gas in cell 2 gives a measure of the number of positronium atoms scattered from the target, $N_{Ps(scatt)}$. This quantity is determined from measurements made with $V_{R2}>V_{CR1}$ to ensure that no positrons from the break-up of positronium in the region of CR1 are included in the measurements. The number of positronium atoms scattered by the gas in cell 2, $N_{Ps(scatt)}$, can be expressed as:

$$N_{Ps(scatt)} = \left| N_{net}(V_{R2} > V_{CR1}) \right|. \tag{5.4}$$

Determination of the total positronium-helium cross-section

To check for consistency of the above procedure, values of the total positronium-helium cross-section, σ_T^{Ps}, have been obtained using the method described in §4.3. From measurements of the intensity of the positronium beam at a potential $V_{R2}>V_{CR1}$ both with ($N_{1,2}$) and without (N_1) gas in the scattering cell, σ_T^{Ps} has been determined using the Beer-Lambert law:

$$\sigma_T^{Ps} = \frac{kT}{pl_+^S} \ln\left(\frac{\left[N_1(V_{R2} > V_{CR1}) - N_V(V_{R2} > V_{CR1})\right]}{\left[N_{1,2}(V_{R2} > V_{CR1}) - N_V(V_{R2} > V_{CR1})\right]} \right), \tag{5.5}$$

where k is the Boltzmann constant, T is the ambient temperature, p the target gas pressure and l_+^S is the effective length of the scattering cell. These values are shown in Figure 5.9 along with the previous data of Armitage (2002) and Garner *et al* (1996) and the total cross-section of Blackwood *et al* (1999), calculated using a coupled-state approximation. Whilst reasonable agreement is seen between the current data and those of Garner *et al* (1996), better consistency is found between the present work and that of Armitage (2002), the current values also being in broad agreement with the theoretical prediction. A weighted mean of the present values of σ_T^{Ps} and those from previous works have been used in equation 5.2 to calculate σ_{BU}.

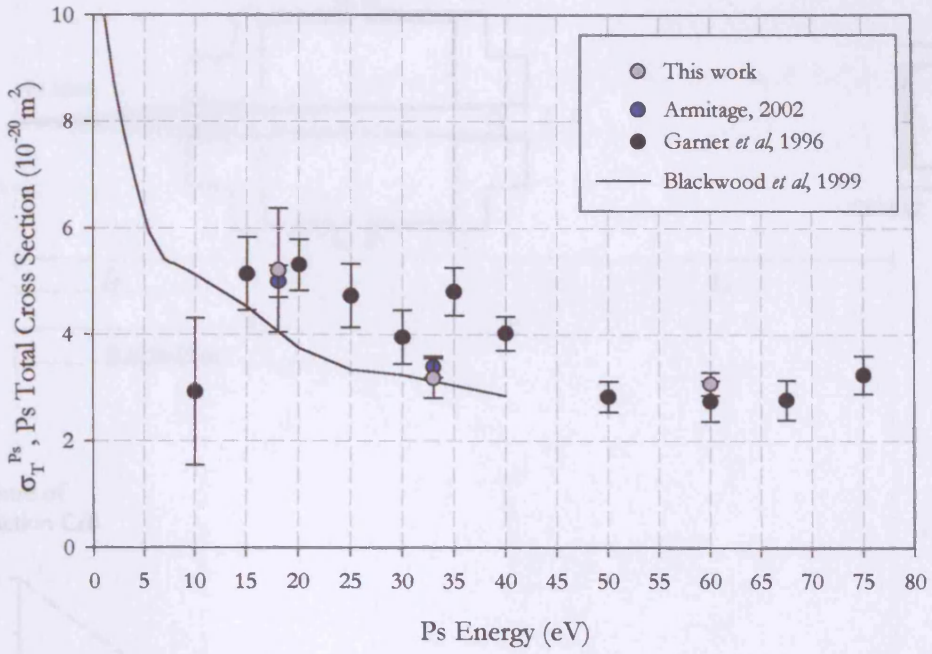

Figure 5.9 Experimentally determined values of the positronium-helium total cross-section along with the corresponding calculation of Blackwood *et al* (1999).

Determination of the Survival Factor, S

Figure 5.10 shows a schematic diagram of the scattering cell region of the experimental arrangement with a graphical representation of the variation of the fraction of positronium atoms which survive in-flight decay as a function of the flight length to CEMA2.

As illustrated in Figure 5.10, due to the finite lifetime of positronium, more positronium atoms are available to break-up within the scattering cell than are detected at CEMA2. In order to correct for this effect, which would lead to an over-estimation of the cross-section, a survival factor, S, is determined, whereby S is the ratio of the fraction of the incident positronium beam that survives to be detected at CEMA2 to the fraction which is available to break-up within the scattering cell, i.e.:

$$S = \frac{S(CEMA2)}{< S(ScatteringCell) >}. \qquad 5.6$$

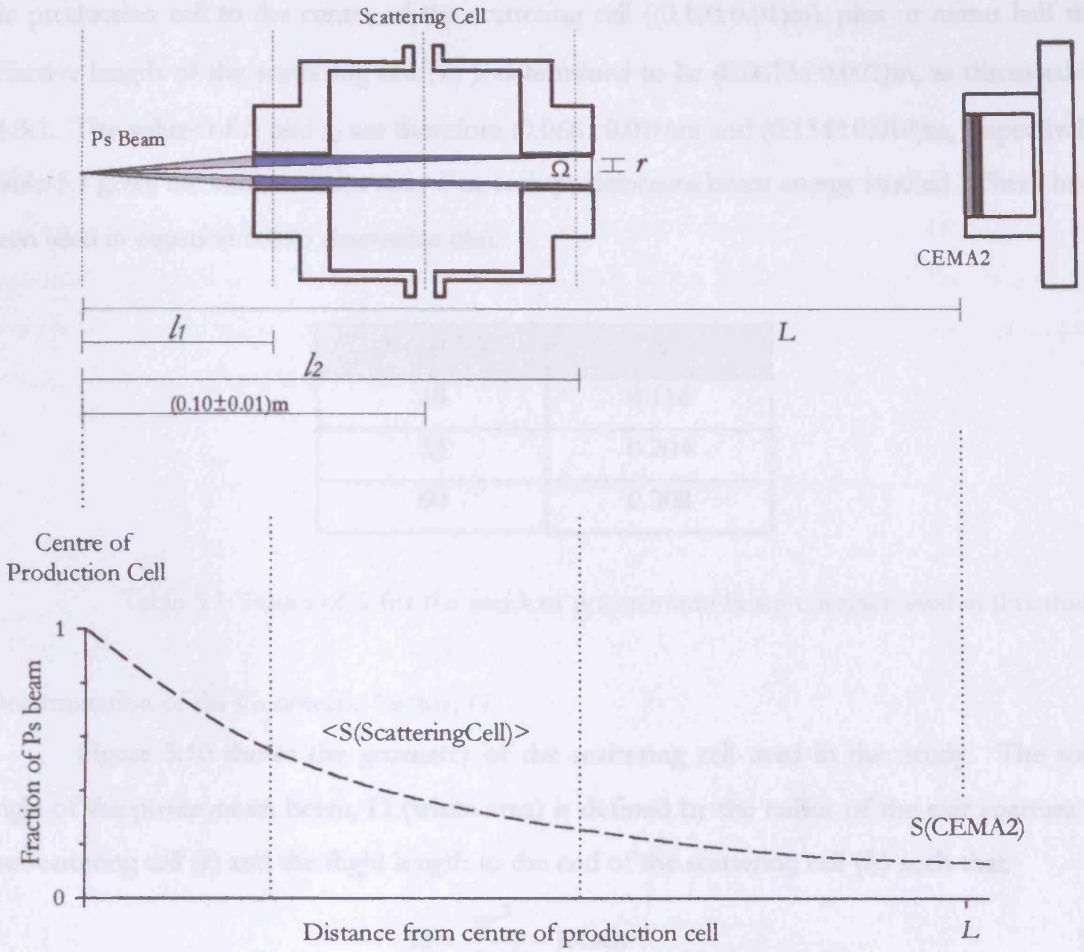

Figure 5.10 Geometry of the scattering cell and graphical representation of the fraction of positronium atoms which survive in-flight annihilation from the centre of the production cell to the detector.

Here, *S(CEMA2)* is the fraction of the positronium beam (of energy, E_{Ps}) which survives to reach the detector at a given flight length (L) and is given by:

$$S(CEMA2) = \exp\left(\frac{-1}{\tau} L \sqrt{\frac{m}{eE_{Ps}}}\right), \qquad 5.7$$

where τ is the ortho-positronium lifetime of 142ns, m is the electron/positron mass and L has been measured to be (0.64±0.05)m in this study. An average value of the fraction of positronium atoms that survive to break-up within the scattering cell, $<S(ScatteringCell)>$, has been calculated according to:

$$<S(ScatteringCell)> = \frac{1}{(l_2 - l_1)} \int_{l_1}^{l_2} \exp\left(\frac{-1}{\tau} x \sqrt{\frac{m}{E_{Ps}}}\right) dx, \qquad 5.8$$

where l_1 and l_2 are defined in Figure 5.10 and correspond to the upper and lower limits of the positronium flight length through the scattering cell, given by the distance from the middle of

the production cell to the centre of the scattering cell ((0.10±0.01)m), plus or minus half the effective length of the scattering cell (l_+^S), determined to be (0.0675±0.002)m, as discussed in §4.3.1. The values of l_1 and l_2 are therefore (0.066±0.010)m and (0.134±0.010)m, respectively. Table 5.1 gives the values of the ratio S at each positronium beam energy studied. These have been used in equation 5.2 to determine σ_{BU}.

E_{Ps} (eV)	S
18	0.116
33	0.204
60	0.308

Table 5.1 Values of S for the incident positronium beam energies used in this study.

Determination of the Geometric Factor, G

Figure 5.10 shows the geometry of the scattering cell used in this study. The solid angle of the positronium beam, Ω (white area) is defined by the radius of the exit aperture of the scattering cell (r) and the flight length to the end of the scattering cell (l_2) such that:

$$\Omega = \frac{\pi r^2}{(l_2)^2} = 1.4 msr . \qquad 5.9$$

However, as in Armitage *et al* (2002), positronium atoms may enter the cell outside this solid angle, as shown by the blue region in Figure 5.10 and upon break-up give rise to a positron, which will be confined by the magnetic field and detected at CEMA2. In order to correct for this effect, which would otherwise lead to an over-estimate of the break-up cross-section, a geometric factor (G, in equation 5.2) has been determined and is given by the ratio of Ω to the average solid angle of the positronium beam along the cell, $<\Omega_{Ps}>$, obtained by integrating over the length of the scattering cell, i.e.:

$$<\Omega_{Ps}> = \frac{\pi r^2}{(l_2 - l_1)} \int_{l_1}^{l_2} \frac{1}{x^2} dx = 3.2 msr . \qquad 5.10$$

Thus, G is evaluated as:

$$G = \frac{\Omega}{<\Omega_{Ps}>} = 0.44 . \qquad 5.11$$

Detection Efficiency

The detection efficiency of CEMA2 for positronium atoms (ε_{Ps}) and positrons (ε_{+}) has been determined by Armitage (2002) through coincidence measurements between CEMA2 and a CsI detector. Two methods were used for determination of ε_{Ps}. Following the assumption that the impact velocity of the positronium atoms is the dominant factor in determining the detection efficiency, equivelocity positrons were used in the first method. In the second, the positronium beam at the required velocity was used directly. These two methods yielded results, which were consistent within errors and are shown in Figure 5.11.

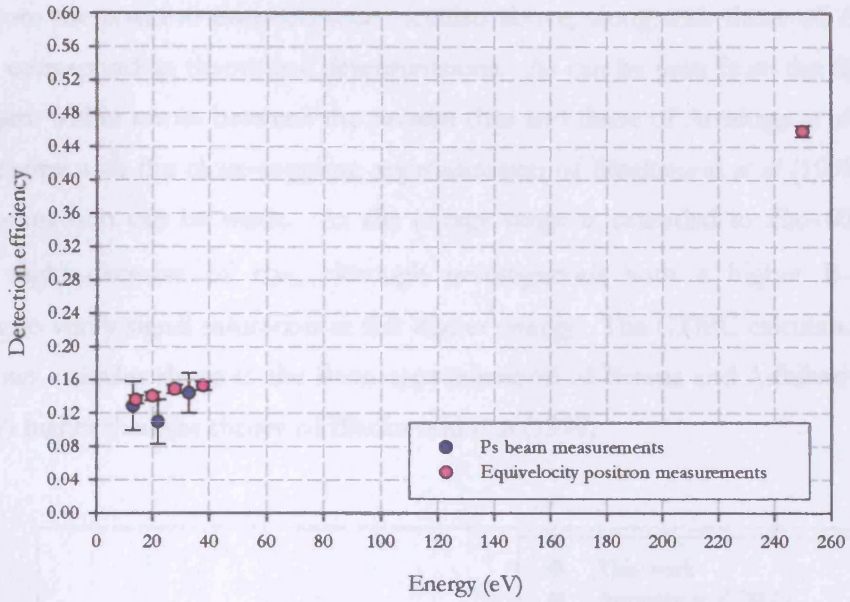

Figure 5.11 Experimentally determined values of the detection efficiency of CEMA2 to positrons and positronium atoms versus incident energy (Armitage, 2002).

Given the potential applied to the front of CEMA2 (-250V in this study), the range of impact energies of the incident positrons is 270-320V over which, ε_{+} is expected to be constant. Thus the value at 250V shown in Figure 5.11 (0.46 ± 0.01) has been used for ε_{+} in equation 5.2. For ε_{Ps} in the same equation, values have been extrapolated from the equivelocity positron measurements at low energies shown in the figure. These were used due to their greater statistical precision over those obtained via direct measurement of the positronium beam. Table 5.2 shows the ratio $\varepsilon_{Ps}/\varepsilon_{+}$ extracted from the data in Figure 5.11 and used in this work to calculate σ_{BU}. In so doing, it is assumed that the different potentials applied to R2 and R3 in this work with respect to Armitage *et al* (2002) affect identically ε_{+} and ε_{Ps}.

E_{Ps} (eV)	$\varepsilon_{Ps}/\varepsilon_{+}$
18	0.30±0.01
33	0.33±0.01
60	0.35±0.01

Table 5.2 Values of detection efficiency at each positronium energy investigated.

Results

Figure 5.12 shows the present results of the absolute break-up cross-section, σ_{BU}, obtained from the positron measurements detailed above, along with those of Armitage *et al* (2002) and corresponding theoretical determinations. As can be seen from the figure, there is fair agreement within errors between the present data and those of Armitage *et al* (2002), both broadly agreeing with the close-coupling approximation of Blackwood *et al* (1999) at energies where a comparison can be made. As the energy range is extended to E_{Ps}=60eV, the data suggest a slight decrease of σ_{BU}, although investigations with a higher **B**-field remain outstanding to verify signal saturation at this higher energy. The CTMC calculation of Sarkadi (2003) follows a similar shape to the Born approximation of Biswas and Adhikari (1999), both being ~40% higher than the theory of Blackwood *et al* (1999).

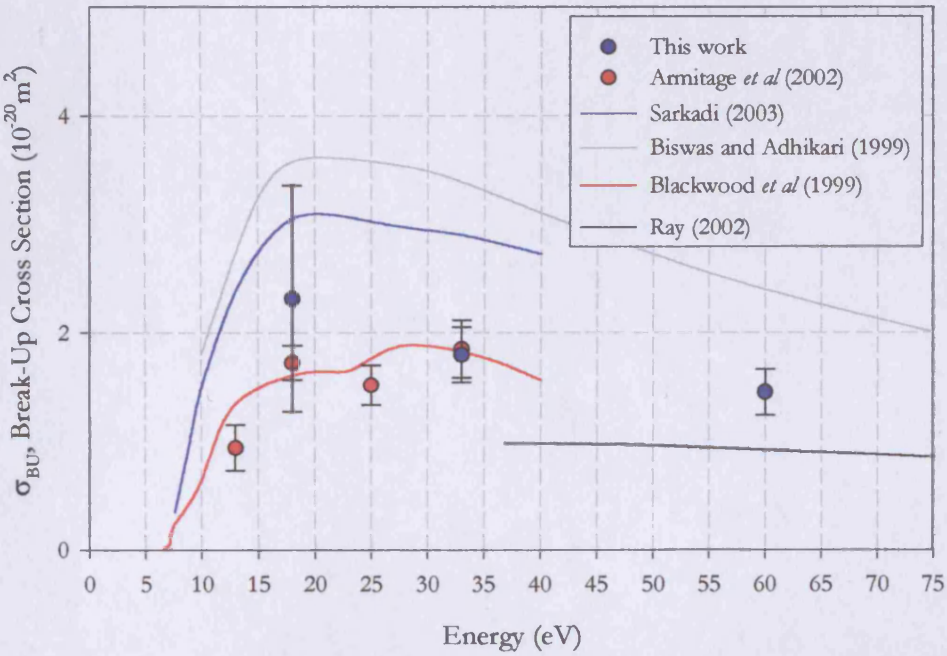

Figure 5.12 Experimental and theoretical values of the break-up cross-section of positronium in collision with helium atoms: experimental values obtained by detection of positrons.

The break-up cross-section of Sarkadi (2003) is larger than the measured data by a factor of between 1.3 and 1.6 over the energy range, exceeded further by the calculation of Biswas and Adhikari (1999). The calculation of Ray (2002), who used the Coulomb-Born approximation, is a factor of ~0.6 lower than the experimental data.

Following the determination of σ_{BU}, the longitudinal energy distributions shown in Figure 5.7 may be set on an absolute scale by normalising the area under the curve to σ_{BU} at each incident positronium energy. This method of normalisation introduces additional uncertainties due to the calculation of the area and the uncertainty in the value of σ_{BU} itself. The resultant distributions are shown in Figure 5.13 plotted in terms of the differential break-up cross-section versus E_+(eV), as before. The present results for the longitudinal energy distributions at E_{Ps}=18eV and 33eV are compared with the absolute values obtained by Armitage *et al* (2002) using the time-of-flight detection system where good agreement is found in the shape of the energy distributions and position of the peak. The position of the peak for E_{Ps}=18eV occurs at ~$0.45E_r$, suggesting that positrons are released within an angle of ~25° with respect to the beam axis, whilst at E_{Ps}=33eV, the peak is shifted only slightly from half of the residual energy to ~$0.48E_r$ implying an angular spread of ~16°. Also shown are the results at E_{Ps}=60eV. The distribution at this energy would be expected to exhibit a peak closer to $E_r/2$ than seen at the lower positronium energies, as Armitage *et al* (2002) found that the peak became more prominent and exhibited less of a shift from $E_r/2$ as the positronium energy increased. However, measurements at E_{Ps}=60eV suggest a broad peak somewhat below $0.5E_r$. Once again, measurements at higher **B**-field are required at this energy to rule out this shift as a systematic failure in confining higher energy positrons emitted at large angles within the cell. Also shown in the figure is the CTMC calculation of Sarkadi (2003) and the Impulse Approximation of Starrett *et al* (2005). Although the calculation of Starrett *et al* (2005) lies ~50% lower than that of Sarkadi (2003) around the peak position at both E_{Ps}=18 and 33eV, it can be seen that both calculations reproduce the shape of the experimental data fairly well, with a peak positioned just below half the residual energy, signalling the occurrence of Electron Loss to the Continuum.

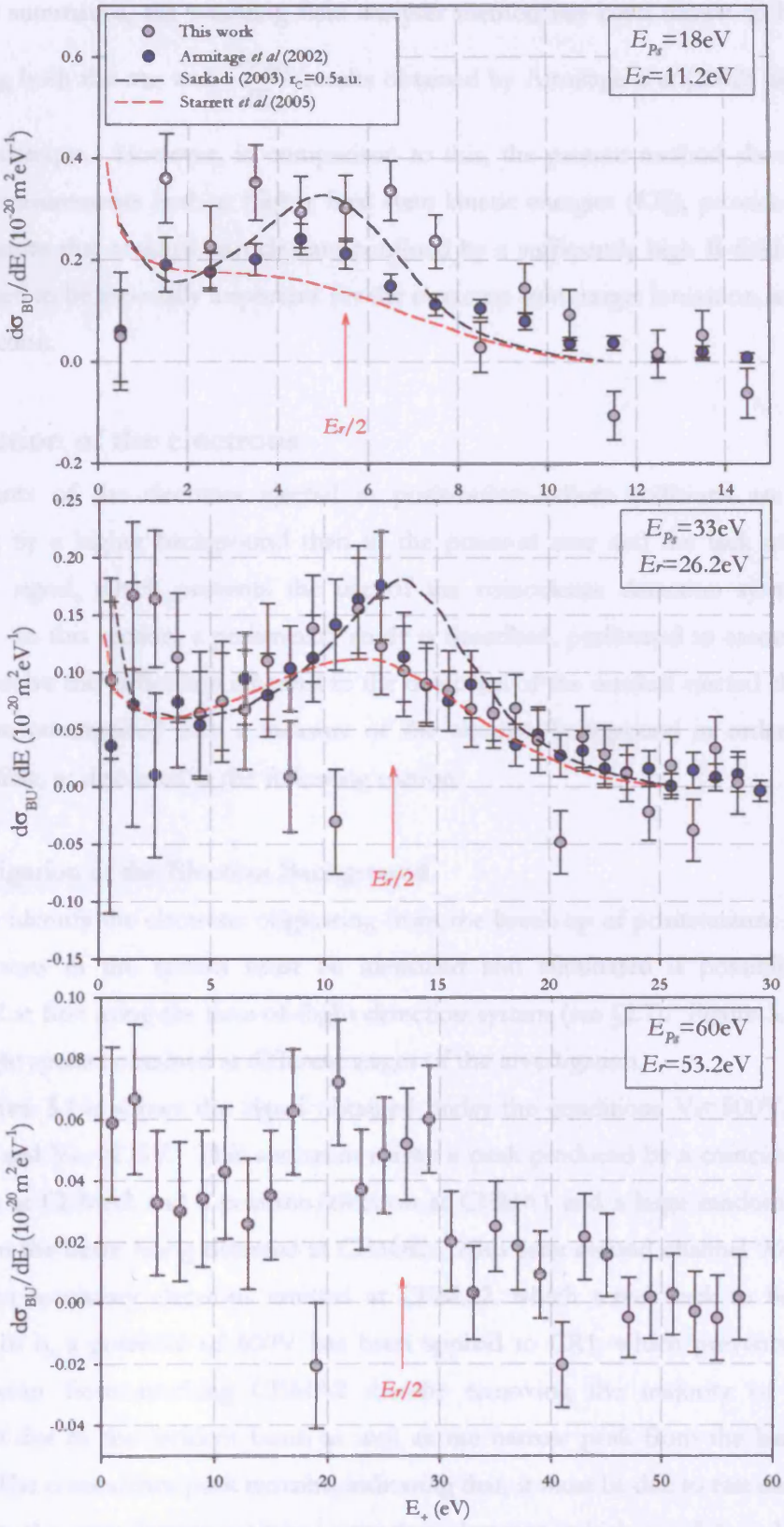

Figure 5.13 Experimentally and theoretically determined values of the absolute differential cross-sections of positrons ejected from the break-up of 18, 33 and 60eV positronium.

To summarise, the retarding field analyser method has been shown to be capable of reproducing both the σ_{BU} and $\frac{d\sigma_{BU}}{dE_+}$ results obtained by Armitage *et al* (2002) using the time-of-flight technique. However, in comparison to this, the present method should lend itself better to measurements both at higher final state kinetic energies (KE_f), provided that care is taken to ensure that residual particles are confined by a sufficiently high **B**-field and at lower KE_f, expected to be especially important for the electrons from target ionisation, as discussed in the next section.

II. Detection of the electrons

Measurements of the electrons ejected in positronium-helium collisions are made more challenging by a higher background than in the positron case and the lack of a correlated gamma-ray signal, which prevents the use of the coincidence detection system employed previously. In this section, a preliminary study is described, performed to assess and, at least partially, resolve the difficulties inherent to the detection of the residual ejected electrons. The investigation commenced with a measure of the electron background in order to reduce it where possible, as discussed in the following section.

II.1 Investigation of the Electron Background

In order to identify the electrons originating from the break-up of positronium, the source of other electrons in the system must be identified and eliminated if possible. This was investigated at first using the time-of-flight detection system (see §2.7). Figure 5.14 shows the time-of-flight spectra obtained at different stages of the investigation.

Figure 5.14a shows the signal obtained under the conditions V_S=500V, V_{M2}=38.6V, V_{F2}=265V and V_{R3}=275V. This spectrum shows a peak produced by a coincidence between an electron at CEMA2 and a positron/electron at CEMA1 and a large random background, arising from the beam being detected at CEMA2. Also seen around channel 960 is a narrow peak due to secondary electrons emitted at CEMA2, which travel back to be detected at CEMA1. In b, a potential of 600V has been applied to CR1, which prevents the primary positron beam from reaching CEMA2 thereby removing the majority of the random background due to the incident beam as well as the narrow peak from the backward-going electrons. The coincidence peak remains, indicating that, it must be due to fast electrons which scatter from the remoderator emitting secondary electrons, which are detected by CEMA1. Applying a negative potential to R2 (-30V applied in c) reduces further the background, indicating some contribution from low energy secondary electrons. Increasing the magnitude

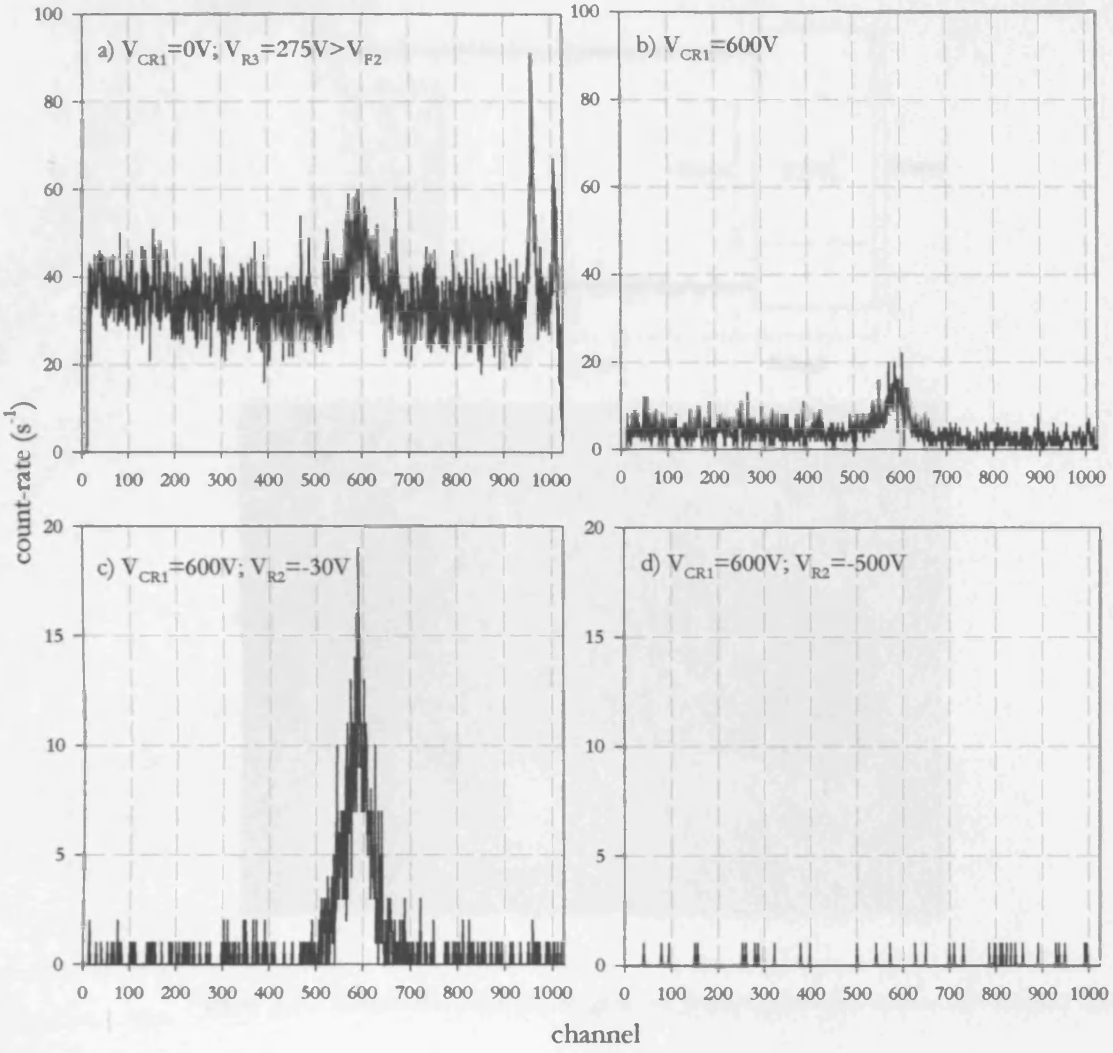

Figure 5.14 Investigation of the electron background.

of the potential applied here allows determination of the longitudinal energy of the electrons which are detected: in d, the potential applied to R2 is -500V, by which point the coincidence peak no longer appears, indicating that the approximate energy of the fast electrons is close to that of the primary positron beam and thus transported through the **E×B**. In order to stop these electrons before they enter the scattering cell, an additional grid has been put in place after CR1: this grid is 95% transmission copper, as is CR1, and is referred to hereafter as CR2.

In order to determine the break-up cross-section from the detection of electrons, some further modifications had to be made to the experimental apparatus. In order to reflect the positrons from the break-up of positronium exiting the scattering cell without creating any additional secondary electrons upon impact on the grids before CEMA2, a retarding field analyser devoid of grids was constructed. It consisted of a set of nine brass discs of internal diameter 22mm, as shown in Figure 5.15. Care was taken to ensure that the positronium beam

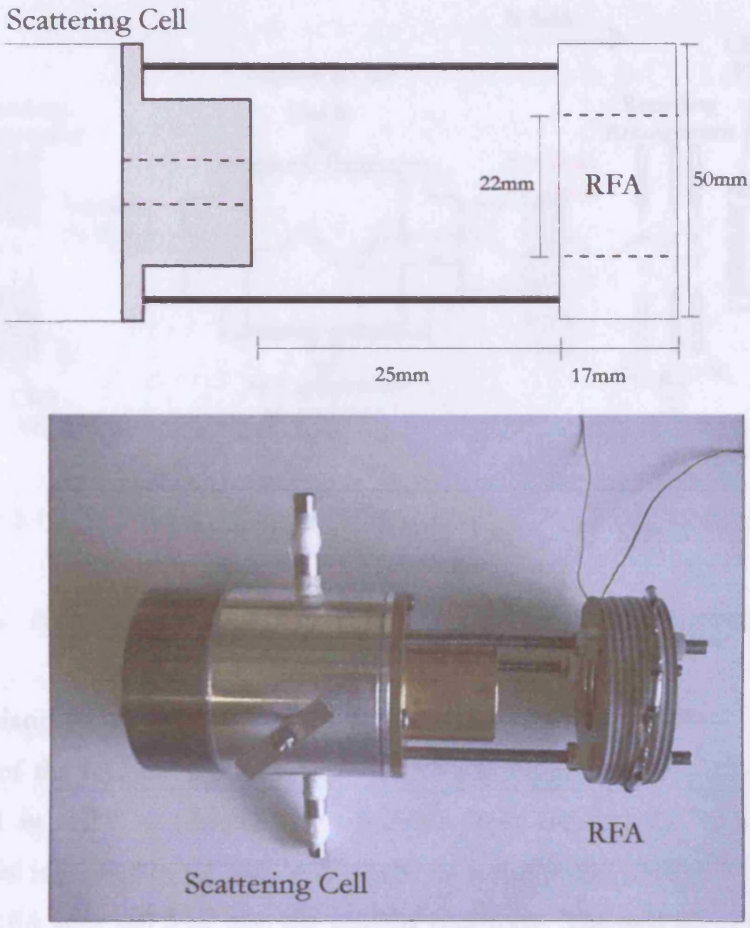

Figure 5.15 Schematic and photographic representations of the developed RFA.

exiting the cell would pass through the arrangement without being intercepted. These discs were separated by PTFE spacers for electrical isolation and enclosed within an earth mesh. A potential was applied to the central disc and a series of eight resistors reduced the potential symmetrically in even steps to ground at either end, minimising fringing of the **E**-field and thus **E**×**B** effects.

II.2 Experimental Method

Figure 5.16 shows a schematic diagram of the positronium scattering region. As discussed in §I.1, molecular hydrogen at a pressure of 10μmHg was used as the positronium beam production gas in this study. The incident positronium beam enters the scattering cell and may break-up on the target gas, which again was helium at a pressure in the range 0-7μmHg (see §I.1).

Electrons released from the fragmentation of positronium are confined to helical trajectories in the **B**-field, with a Larmor radius which depends on their kinetic energy and

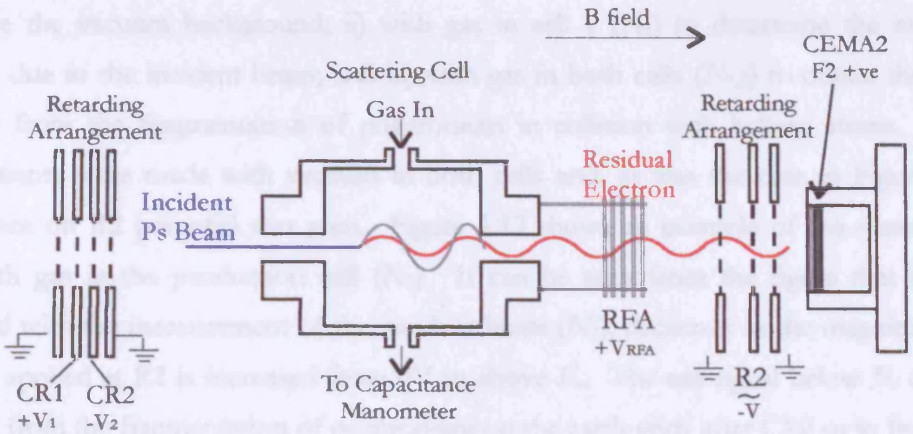

Figure 5.16 Potentials applied to electrostatic elements during electron measurements.

emittance angle. As in the case of positrons, a **B**-field of 15.7mT was used for the electron measurements.

The polarity of the potentials applied to the various electrostatic elements for the measurements of the residual electrons are indicated in Figure 5.16. A positive potential is applied to CR1 in order to prevent any positrons from entering the scattering cell and a negative potential is applied to CR2 to repel electrons at this point, whilst a positive potential is applied to the RFA after cell 2 to stop the residual positrons. The grid R2 in front of CEMA2 is grounded when measuring the total flux of electrons and transmitted positronium atoms and negative when measuring the flux of transmitted positronium atoms. The yield of electrons from positronium fragmentation may then be obtained by subtraction. Discussed in the following sections are the measurements required in order to determine the yield of electrons from the break-up of positronium. All errors on the count-rates shown include the uncertainty in the pressure (±0.5%) and in the beam flux (±0.5%). As stated in §5.1, in the absence of a correlated gamma-ray signal, the electron data were obtained using only the single counts from CEMA2, which were recorded using a multi-channel scaler (MCS, see §2.7). Clearly, this resulted in a much worse signal to background ratio, as described below. Measurements have, once again, been made over two ranges of V_{R2}: (i) for the determination of the energy distribution of electrons, detailed measurements have been made of electrons with energies below the residual energy, whilst (ii) a larger energy range has been investigated to calculate the integrated break-up cross-section.

II.3 Results

In order to measure the longitudinal energy distribution of the electrons from the fragmentation of positronium, a variable negative potential was applied to the grid R2 as shown in Figure 5.16. As in §I.2, measurements were made: i) with vacuum in both cells (N_V) to

determine the vacuum background; ii) with gas in cell 1 (N_1) to determine the number of electrons due to the incident beam; and iii) with gas in both cells ($N_{1,2}$) to obtain the residual electrons from the fragmentation of positronium in collision with helium atoms. Initially, measurements were made with vacuum in both cells and, as was the case in Figure 5.2, no dependence on R2 potential was seen. Figure 5.17 shows an example of the measurements made with gas in the production cell (N_1). It can be seen from the figure that the signal associated with the measurement of the incident beam (N_1), decreases as the magnitude of the potential applied at R2 is increased from 0V to above E_r. The net signal below E_r comprises electrons from the fragmentation of positronium on the earth grids after CR2 or in front of R2, or on the apertures of the scattering cell (cell 2). Above E_r, the signal becomes constant and arises from the incident positronium beam and electrons due to break-up of positronium at CR2. As the potential at R2 is decreased from -80 to -120V, the count-rate is seen to decrease further. In the case of the positron measurements (see §I.2), such a decrease was seen as the potential applied at R2 was increased to above that at CR1, as positrons released from the break-up of positronium at CR1 were repelled. In the electron measurements, however, positronium may also break-up at CR2 and the electron released will be accelerated towards CEMA2 by the negative potential at CR2, being stopped once $|V_{R2}|>|V_{CR2}|+E_r$. The magnitudes of the potential applied to R2, CR1 and CR2 were increased with increasing E_{Ps}. Above $|V_{R2}|=|V_{CR2}|+E_r$, the count-rate is due to the incident positronium beam and the vacuum background.

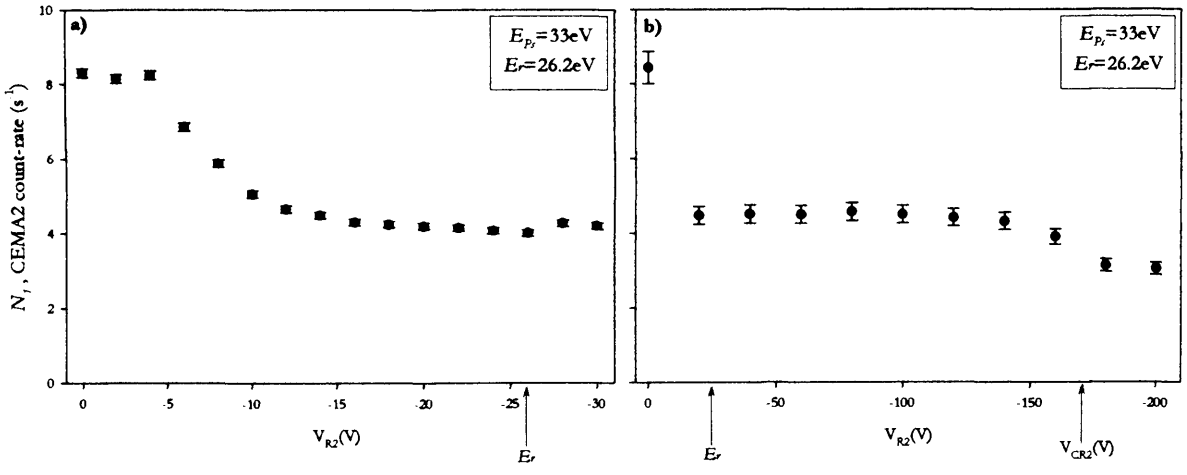

Figure 5.17 An example of electron measurements with gas in the production cell: a) detailed measurements; b) larger energy range and step.

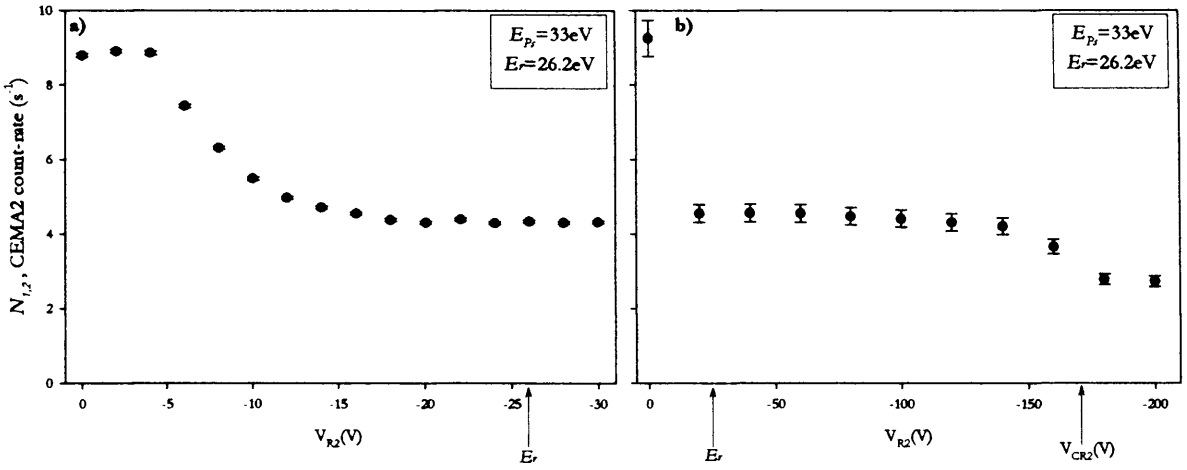

Figure 5.18 An example of electron measurements with gas in both cells: a) detailed measurements; b) larger energy range and step.

Figure 5.18 shows results obtained with gas in both cells ($N_{1,2}$) where it can be seen that the presence of gas in cell 2 gives rise to an increase in the electron count-rate at V_{R2}=0V of only ~6%. Once again, a decrease in the count-rate is apparent as the magnitude of V_{R2} is increased from 0V to above E_r. The signal below E_r comprises the positronium beam transmitted through the scattering cell and electrons from positronium breaking-up at the earth grid after CR2 and that before R2, plus additional electrons from the break-up of positronium in collision with helium atoms in the scattering cell and those from electron impact ionisation, as will be discussed later. As seen previously in Figure 5.17, the count-rate in Figure 5.18 decreases further when $|V_{R2}| > |V_{CR2}|$, where electrons accelerated by the potential at CR2 are stopped at R2. At this point, the signal is due to the transmitted positronium beam and the vacuum background only.

Figure 5.19 shows the net signal ($N_{net}=N_{1,2}-N_1$) obtained for both the detailed and coarse energy step measurements. The two sets of data indicate a net positive signal of similar magnitude, corresponding to electrons arising from positronium collisions with helium in cell 2. Corresponding data to those shown in Figure 5.19 have also been obtained at E_{P_s}=18 and 60eV and although some net positive signal has been determined, they do not warrant further analysis. Therefore, in the following sections, the energy distribution of electrons and the break-up cross-section will only be determined at E_{P_s}=33eV.

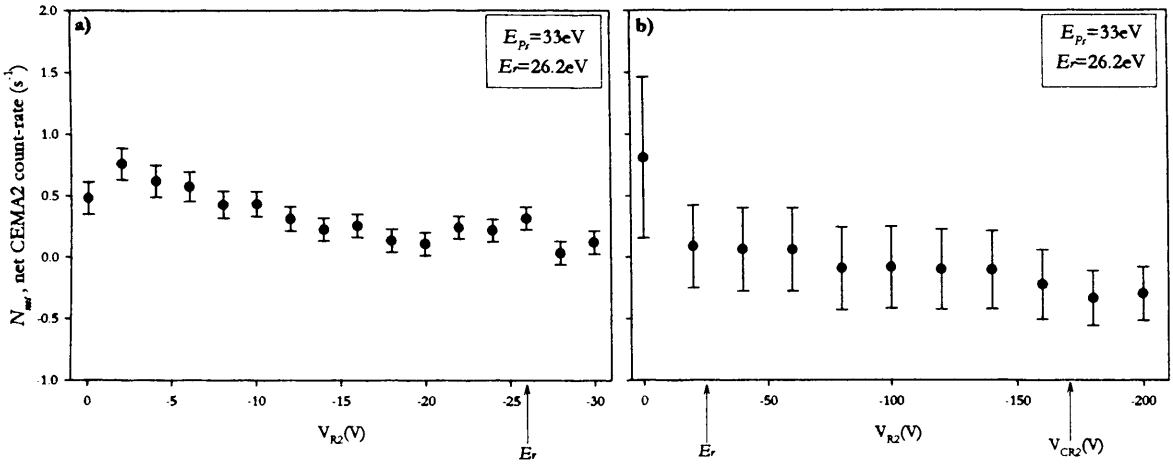

Figure 5.19 An example of the net electron signal obtained from a) detailed and b) coarse measurements.

II.4 Analysis

II.4.1 Integrated Cross-Section for the Break-Up of Positronium

As stated in §I.3.2, the experimentally determined absolute break-up cross-section of positronium atoms (Armitage *et al*, 2002) at a given energy, E_{Ps}, may be expressed as:

$$\sigma_{BU}(E_{Ps}) = \frac{N_-^{Ps}}{N_{Ps(scatt)}} \sigma_T^{Ps} SG\left(\frac{\varepsilon_{Ps}}{\varepsilon_-}\right), \qquad 5.12$$

where N_-^{Ps} is the net number of electrons released from the break-up of positronium in collision with helium atoms; $N_{Ps(scatt)}$ is the number of scattered positronium atoms; σ_T^{Ps} is the total cross-section for positronium scattering; $(\varepsilon_{Ps}/\varepsilon_-)$ is the ratio of the efficiencies for positronium atom and electron detection by CEMA2; S corrects for the in-flight decay of positronium atoms; and G is a geometric factor pertinent to the scattering cell, as described in detail in §I.3.2.

Determination of N

In order to determine the total number of electrons from the break-up of positronium, the net signals shown previously in Figure 5.19 have been used. These data appear once again below, where the detailed and coarse energy step measurements are shown together and found to be consistent.

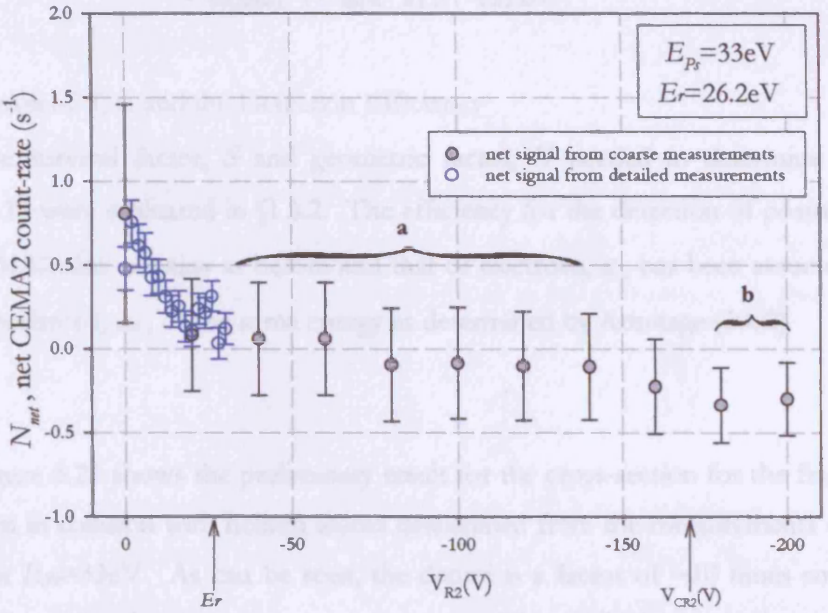

Figure 5.20 Net electron signal from detailed and coarse energy step measurements.

As the potential at R2 is increased, the net signal falls below zero, ultimately giving a measure of the number of positronium atoms scattered from the beam, $N_{Ps(scatt)}$. These net data shall now be used to determine the integrated break-up cross-section. The labels **a** and **b** in the figure correspond to data points used below.

The number of electrons from events from the gas in cell 2, is given by the net number of electrons detected at V_{R2}=0V minus the average number in the region above E_r, indicated by **a** in the figure, i.e.:

$$N_{-} = N_{net}(0) - N_{net}(a). \qquad 5.13$$

Due to the consistency between the data from the detailed and coarse measurements, the small energy step measurements at V_{R2}=0 and -2V have been included in the weighted mean value of $N_{net}(0)$ and those at V_{R2}=-28 and -30V in $N_{net}(a)$. The possibility that electrons emitted from the break-up of positronium in the region of CR2 might give rise to secondary electrons from ionisation of helium (Sorokin *et al*, 2004) has been considered and is estimated to give rise to a contribution less than 5% and has thus been neglected.

Determination of $N_{Ps(scatt)}$

As discussed in §I.3.2, the number of positronium atoms scattered by the gas in cell 2, $N_{Ps(scatt)}$, may be obtained from the signals with and without gas in cell 2. This quantity is determined from measurements made at $|V_{R2}| > |V_{CR2}|$ to ensure that no electrons from the break-up of positronium in the region of CR2 are included in the measurements. The number of positronium atoms scattered by the gas in cell 2, $N_{Ps(scatt)}$, is then:

$$N_{Ps(scatt)} = N_{net}(|V_{R2}| > |V_{CR2}|). \quad 5.14$$

Determination of S, G and the Detection Efficiency

The survival factor, S and geometric factor, G needed to determine $\sigma_{BU}(E)$ using equation 5.12 were evaluated in §I.3.2. The efficiency for the detection of positronium atoms, ε_{Ps}, by CEMA2 also remains as before and that of electrons, ε_-, has been assumed to be equal to that of positrons, ε_+, of the same energy as determined by Armitage (2002).

Results

Figure 5.21 shows the preliminary result for the cross-section for the fragmentation of positronium in collision with helium atoms determined from the measurements of the residual electrons at E_{Ps}=33eV. As can be seen, the datum is a factor of ~10 times smaller than the corresponding value from positron measurements. This might be partly due to the detection efficiency of the CEMA2 to electrons having been taken to be the same as that of the positrons. This might not be entirely correct, but it is deemed unlikely to explain the observed order of magnitude discrepancy. A more plausible origin of the discrepancy might be that the total cross-section for electrons exceeds that of positrons by up to a factor of 10^2 in the energy range of interest. As a consequence, the detection efficiency of the low energy electrons will be strongly suppressed by scattering within cell 2 in comparison with that for equivelocity

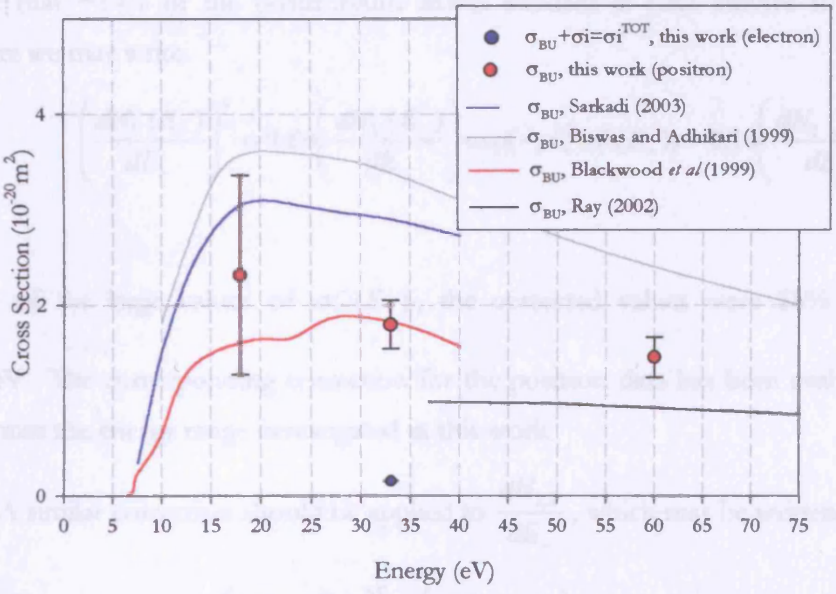

Figure 5.21 Experimental and theoretical values of the break-up cross-section of positronium in collision with helium atoms: red data points obtained from positron detection; blue data point obtained from electron detection.

positrons. In the following section, we proceed to evaluate this effect and thus assess the validity of the above hypothesis.

II.4.2 Energy Distribution of Electrons

In order to correct the number of electrons with energy E_- for attenuation by helium in cell 2, the number of electrons with energy E_- is first obtained by differentiating the detailed measurements made without (N_1) and with ($N_{1,2}$) gas in cell 2 shown in Figures 5.17 and 5.18, respectively, i.e.:

$$\frac{dN_1}{dE_-} \quad \text{and} \quad \frac{dN_{1,2}}{dE_-}. \tag{5.15}$$

If all electrons from positronium break-up at surfaces originate before cell 2, then we must consider the attenuation of N_1 in the presence of gas in cell 2. The count-rate obtained with gas in the production cell only must be corrected at each energy according to:

$$\left(\frac{dN_1(E_-)}{dE_-}\right)^c = \left(\frac{dN_1(E_-)}{dE_-}\right)\exp(-\rho l_+^S \sigma_T^-(E_-)), \tag{5.16}$$

where ρ is the gas number density in the scattering cell during measurements of the transmitted beam, l_+^S is the effective length of the scattering cell ((6.75±0.02)cm, see §4.3.1) and $\sigma_T^-(E_-)$ is the electron total cross-section from helium (Kauppila and Stein, 1990). However, to allow for electrons from positronium breaking-up upon impact on the grids near CEMA2, we must consider that ~14% of the positronium atoms incident at CR1 survive to reach CEMA2. Therefore we may write:

$$\left(\frac{dN_1(E_-)}{dE_-}\right)^c = 0.86\left(\frac{dN_1(E_-)}{dE_-}\right)\exp(-\rho l_+^S \sigma_T^-(E_-)) + 0.14\left(\frac{dN_1(E_-)}{dE_-}\right). \tag{5.17}$$

Because of the large values of $\sigma_T^-(E_-)$, the corrected values were 55% of $\frac{dN_1(E_-)}{dE_-}$ at E_{P_s}=33eV. The corresponding correction for the positron data has been evaluated to be only 1-9% across the energy range investigated in this work.

A similar correction should be applied to $\frac{dN_{1,2}}{dE_-}$, which may be written as:

$$\left(\frac{dN_{1,2}(E_-)}{dE_-}\right)^c = \left(\frac{dN_{1,2}(E_-)}{dE_-}\right)\exp(\rho l_+^{'S} \sigma_T^-(E_-)), \tag{5.18}$$

where, as above, ρ is the gas number density in the scattering cell during measurements of the transmitted beam, and $\sigma_T^-(E_-)$ is the electron total cross-section from helium. The cell length,

l_+^S, has been determined by calculating the distance along the scattering cell at which half the positronium atoms have broken up i.e. where half the electrons are emitted. This calculation is similar to that shown previously in §4.2, whereby l_{Ps} was determined. Due to the fact that positronium has an equal probability of breaking-up at any point within the cell, we are once again required to consider the variation in the solid angle, the fraction of positronium atoms which decay in-flight at differing points along the scattering cell and the fraction of positronium atoms which scatter along the cell.

The flux of positronium atoms N_{Ps} can be written as a function of the flight length through the scattering cell, x, as:

$$N_{Ps}(x) = N_{Ps}(0)\exp(-\rho x \sigma_T^{Ps}), \tag{5.19}$$

which may be differentiated to give the fraction within an element of length dx such that:

$$N_{Ps}'(x) = -\rho\sigma_T^{Ps} N_{Ps}(0)\exp(-\rho x \sigma_T^{Ps}). \tag{5.20}$$

The solid angle can be expressed as:

$$\Omega(x) = \frac{\pi r^2}{(D+x)^2}, \tag{5.21}$$

where r is the radius of the exit aperture of cell 2, D is the distance from the centre of the production cell to the entrance aperture of the scattering cell and x is the scattering point within the cell, where $0 \le x \le l_+^S$. By taking into account the fraction of positronium atoms $F(x)$ with kinetic energy, E_{Ps}, which survive in-flight decay along the scattering cell as given by equation 4.6, the number of scattered positronium atoms is thus:

$$N_{Ps(scatt)} = \int_0^{l_+^S} \Omega(x)F(x)N_{Ps}'(x)dx = -\rho\sigma_T^{Ps}\pi r^2 N_{Ps}(0)\int_0^{l_+^S} \frac{1}{(D+x)^2}\exp\left(\frac{-16.79(D+x)}{E_{Ps}^{\frac{1}{2}}}\right)\exp\left(-\rho x\sigma_T^{Ps}\right)dx, \tag{5.22}$$

which can be rearranged to give:

$$N_{Ps(scatt)} = -\rho\sigma_T^{Ps}\pi r^2 N_{Ps}(0)\int_0^{l_+^S} \frac{1}{(D+x)^2}\exp(-xB+C)dx, \tag{5.23}$$

where:

$$B = \left(\frac{16.79}{E_{Ps}^{\frac{1}{2}}} + \rho\sigma_T^{Ps}\right) \quad \text{and} \quad C = \left(\frac{16.79D}{E_{Ps}^{\frac{1}{2}}}\right). \tag{5.24}$$

In order to find the point in the cell where half the positronium atoms are scattered, the integral $N_{Ps(scatt)}$ may be evaluated numerically (as in equation 4.13) using:

$$N_{Ps(scatt)} = \int_0^{l_+^S} g(x)dx = \sum_{x=0}^{l_+^S} g(x)\Delta x \qquad 5.25$$

from 0 to l_+^S for incrementally decreasing values of Δx, until convergence is found and hence the value of x at which half the positronium atoms have scattered was determined for each energy studied. From this point in the cell ($l_+^{'S}$), the attenuation of the residual electrons at each energy has been determined and corrected for using equation 5.18. The corrected values were a factor of 1.7 times the measured data. In the case of the positron measurements, this correction would typically amount to an increase in $\frac{dN_{1,2}}{dE_+}$ of only between 1-8%.

Following these corrections, the yield of electrons from positronium break-up on helium in the scattering cell and from positronium impact on the gas has been determined by subtracting the corrected signal due to the incident beam from the signal from the transmitted beam i.e.:

$$\left(\frac{dN_-(E_-)}{dE_-}\right)^c = \left(\frac{dN_{1,2}(E_-)}{dE_-}\right)^c - \left(\frac{dN_1(E_-)}{dE_-}\right)^c. \qquad 5.26$$

Figure 5.22 shows the results for $\left(\frac{dN_-(E_-)}{dE_-}\right)^c$ at E_{Ps}=33eV. The arrow indicates $E_r/2$ where the residual energy of the system, E_r = E_{Ps} - 6.8eV, 6.8eV being the positronium binding energy.

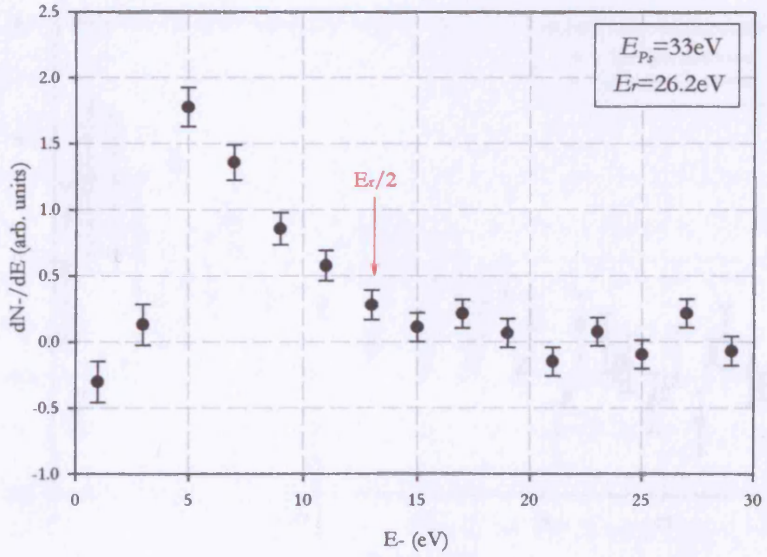

Figure 5.22 Results of $\left(\frac{dN_-(E_-)}{dE_-}\right)^c$ for E_{Ps}=33eV.

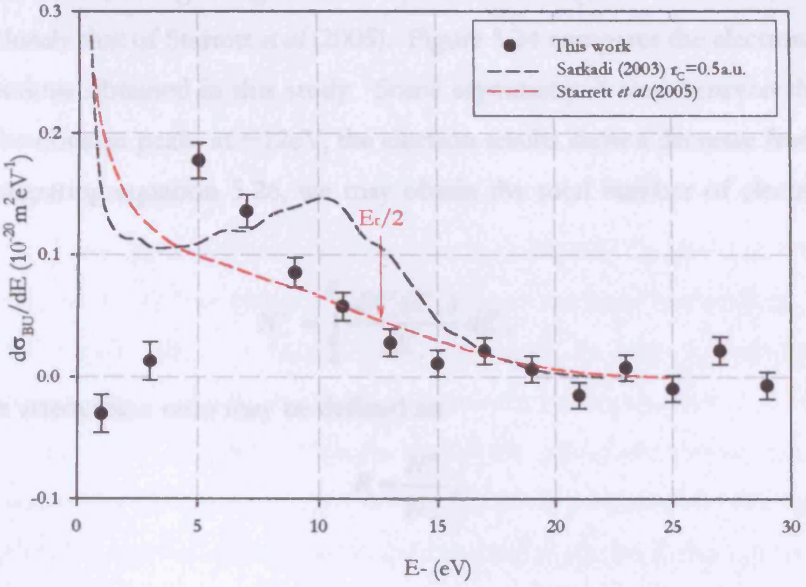

Figure 5.23 Energy distribution of electrons from 33eV positronium in collision with helium. Experimental data have been scaled to allow shape comparison.

Figure 5.23 compares the electron energy distribution measured in this study with the calculations of Sarkadi (2003) and Starrett *et al* (2005). In order to evaluate the similarity of the shape of the distributions, the experimental data have been normalised to the calculations at 19eV. The increase of the differential cross-section at low energies seen in both calculations is also apparent in the experimental results, as is the decrease to zero by 20eV. The fact that the data at the lowest two energies appear low is probably owing to the scattering of low energy

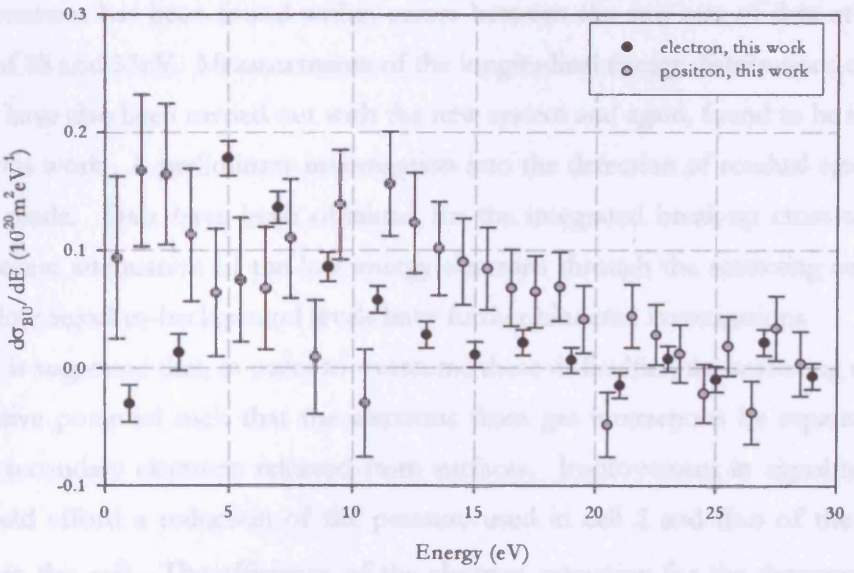

Figure 5.24 Comparison of energy distributions of residual positrons and electrons for E_{Ps}=33eV.

electrons in cell 2 and, disregarding these two points, the shape of the distribution appears to follow more closely that of Starrett *et al* (2005). Figure 5.24 compares the electron and positron energy distributions obtained in this study. Some asymmetry is seen between the two: whilst the positron distribution peaks at ~12eV, the electron results show a decrease from above 5eV.

By integrating equation 5.26, we may obtain the total number of electrons from gas events i.e.:

$$N_-^c = \int_0^{E_r} \frac{dN_-^c(E_-)}{dE_-} dE, \qquad 5.27$$

from which an attenuation ratio may be defined as:

$$R = \frac{N_-^c}{N_-}, \qquad 5.28$$

where:

$$N_- = N_{1,2}(0) - N_1(0) \qquad 5.29$$

and $N_1(0)$ and $N_{1,2}(0)$ are the values at V_{R2}=0V. This attenuation ratio has been determined to have an average value of 21±6 for the data obtained at E_{P_i}=33eV and thus of the right order of magnitude to account for the discrepancy between $\sigma_{BU}(e^+)$ and $\sigma_{BU}(e^-)$ discerned with reference to Figure 5.21.

III. Conclusions

The absolute break-up cross-section for positronium in collision with helium atoms has been measured at 18, 33 and 60eV using an alternative method to that used by Armitage *et al* (2002). Good agreement has been found within errors between the two sets of data at the common energies of 18 and 33eV. Measurements of the longitudinal energy distributions of the residual positrons have also been carried out with the new system and again, found to be in accord with the previous work. A preliminary investigation into the detection of residual ejected electrons has been made. Data have been obtained for the integrated break-up cross-section, which indicate severe attenuation of the low energy electrons through the scattering cell below 5eV. The very low signal-to-background levels have further hindered investigations.

It is suggested that, in order to overcome these difficulties, the scattering cell be floated to a negative potential such that the electrons from gas interactions be separated in energy from the secondary electrons released from surfaces. Improvement in signal-to-background levels would afford a reduction of the pressure used in cell 2 and thus of the scattering of electrons in this cell. The efficiency of the electron extraction for the determination of σ_{BU} could then be tested by inserting an accelerator within cell 2 of similar construction to the RFA illustrated in Figure 5.15.

Chapter 6
Conclusions and Future Work

6.1 Summary and Conclusions

The energy range over which a beam of positronium atoms may be produced by the charge-exchange reaction of a positron beam in a gaseous target has been extended to 250eV by the use of molecular nitrogen as the production gas. The longitudinal energy distribution has been measured, thereby confirming that the beam is dominantly comprised of ground-state atoms. The work of Laricchia *et al* (2002) identified a double peak structure in the positronium formation cross-section of xenon, which has recently been confirmed by Marler *et al* (2005). Laricchia *et al* (2002) suggested the origin of the structure might be formation of Ps*, implying that 50-100% of the positronium beam produced at 40eV may be due to Ps*. Motivated by these studies, in this work the positronium beam produced from xenon has been investigated. The dominant quantum state of the positronium beam has been determined to be n=1, although its yield was lower than expected. This might be due to quenching of positronium in interactions with the production gas itself or to a broader differential positronium formation cross-section.

The total cross-section for positronium scattering from molecular hydrogen, molecular nitrogen and xenon has been determined indirectly and then measured directly. Good agreement is seen between the two methods. The positronium total cross-sections (σ_T^{Ps}) have been compared with the corresponding total cross-sections for equivelocity positrons and electrons ($\sigma_T^{\pm}$). Measurements of σ_T^{Ps} from xenon have been found surprisingly to be only ~20% larger than that from argon around the peak and it is suggested that this system warrants further investigation.

The absolute cross-section for the break-up of positronium in collision with helium atoms has been determined using an alternative method to that employed by Armitage *et al* (2002). Initial investigation of the reliability of the system proved encouraging and enabled the energy range of measurements of residual positrons to be extended. Results for the differential- and integrated break-up cross-section are presented at 18, 33 and 60eV. A preliminary study has been made into the detection of the corresponding ejected electrons. Due to the susceptibility of the method to background, the study proved challenging. Nevertheless, following the reduction of the background levels and modifications to the experimental arrangement, a net positive signal has been detected at positronium energies of 18, 33 and 60eV. Due to large statistical uncertainties, only those at 33eV have warranted further analysis in this work. The energy distribution of the electrons detected at this energy

has been determined and compared to the calculations of Sarkadi (2003) and Starrett *et al* (2005) as well as the corresponding positron data. A value for the integrated break-up cross-section (σ_{BU}) has been calculated from the data at E_{Ps}=33eV, indicating severe attenuation of the low energy electrons by helium in the scattering cell.

6.2 Suggestions for Future Work

The behaviour of the positronium total cross-section from xenon with respect to its closeness to that from argon may prompt further investigation. Measurements may be made from krypton to investigate whether a relationship between the positronium- and electron total cross-sections remains. The uncertainty on the positronium cross-section at the lowest energies may be reduced by the improvement of the energy resolution of the positronium beam itself. It is anticipated that the development of rare gas solid moderators may be continued with the use of neon, which yields a much improved energy distribution in comparison with that from argon.

The investigation into the detection of electrons ejected from positronium-helium collisions presented in this thesis is currently being extended. A new scattering cell has been designed and employed, such that low energy electrons may be accelerated from within the cell by applying a negative bias, thereby shifting the spectrum of residual electrons with respect to those from the incident positronium beam and background. This is enabling more accurate determination of the net signal from the residual electrons. In addition, the use of a lower gas pressure in the scattering cell is necessary to lessen the attenuation of the transmitted electron beam and further reduce the uncertainty on the net signal. It is important that the extension of this study also include an investigation into the behaviour of the signal with the confining **B**-field to ensure that all residual electrons (or positrons) are extracted from the scattering cell. It is envisaged that taking these steps will enable the longitudinal energy distribution of the residual electrons to be determined as well as a more accurate determination of the integrated cross-section. A study of target ionisation remains outstanding. An investigation into positronium fragmentation in collision with a heavier target atom, such as xenon, would be worthwhile following the recent work of Starrett *et al* (2005). These authors reported that the asymmetry seen at lower energies in the longitudinal energy distributions of the residual positrons and electrons from helium should be much less pronounced in the case of xenon.

References

Adachi S, Chiba M, Hirose T, Nagayama S, Nakamitsu Y, Sato T and Yamada T, 1990 *Physical Review Letters* **65** 2634

Adkins G S, 1983 *Physical Review A* **27** 1 530

Adkins G S, Alalhuddin A A and Schalm K E, 1992 *Physical Review A* **45** 7774

Al-Ramadhan A H and Gidley D W, 1994 *Physical Review Letters* **72** 1632

Andersen C D, 1932a *The Physical Review* **41** 405

Anderson C D, 1932b *Science* **76** 238

Andersen C D, 1933 *Physical Review* **43** 491

Armitage S, Leslie D E, Garner A J and Laricchia G, 2002 *Physical Review Letters* **89** 173402-1

Armitage S, 2002 PhD Thesis University College London

Armitage S, Beale J, Leslie D E and Laricchia G, 2005 *Nuclear Instruments and Methods in Physics Research B* **233** 88

Asai S, Orito O and Shinohara N, 1995 *Physics Letters B* **357** 475

Basu A, Sinha P K and Ghosh A S, 2001 *Physical Review A* **63** 052503

Bellotti E, Corti M, Fiorini E, Liguori C, Pullia A, Sarracino A, Sverzellati P and Zanotti L, 1983 *Physics Letters* **124B** 435

Biswas P K and Adhikari S K, 1999 *Physical Review A* **59** 363

Biswas P K and Adhikari S K, 2000 *Journal of Physics B: Atomic Molecular and Optical Physics* **33** 1575

Biswas P K, Germano J S E and Frederico T, 2002 *Journal of Physics B: Atomic Molecular and Optical Physics* **35** L409

Blackett P M S and Occhialini G P S, 1933 *Proceedings of the Royal Society London A* **139** 699

Blackwood J E, Campbell C P, McAlinden M T and Walters H R J, 1999 *Physical Review A* **60** 4454

Blackwood J E, McAlinden M T and Walters H R J, 2002 *Journal of Physics B: Atomic Molecular and Optical Physics* **35** 2661

Bluhme H, Frandsen N P, Jacobsen F M, Knudsen H, Merrison J, Paludan K and Poulsen M R, 1998 *Journal of Physics B: Atomic Molecular and Optical Physics* **31** 4631

Bransden B H, 1969 in *"Case study in atomic collision"* eds. McDaniel and McDowell (North Holland) p171

Campbell C P, McAlinden M T, Kernoghan A A and Walters H R J, 1998 *Nuclear Instruments and Methods in Physics Research B* **143** 41

Chang T, Li Q. Wang Y and Li Y, 1982 *"Positron Annihilation"* eds. P. Coleman, S. C. Sharman and L. M. Diana (North Holland: Amsterdam) p32

Chang T, Li Q. Wang Y and Li Y, 1985 *"Positron Annihilation"* eds. P. C. Jain, R. M. Singru and K. P. Gopinathan (Singapore: World Scientific) p212

Charlton M, 1985 *Reports on Progress in Physics* **48** 737

Charlton M and Humberston J W, 2001 in *'Positron Physics'* Cambridge University Press

Coleman P G, 2002 *Nuclear Instruments and Methods in Physics Research B* **192** 83

Coleman P G, Rayner S, Jacobsen F M, Charlton M and West R N, 1994 *Journal of Physics B: Atomic Molecular and Optical Physics* **27** 981

Czernin J and Phelps M E, 2002 *Annual Review of Medicine* **53** 89

Dababneh M S, Kauppila W E, Downing J P, Laperriere F, Pol V, Smart J H and Stein T S, 1980 *Physical Review A* **22** 1872

Dababneh M S, Hsieh Y F, Kauppila W E, Pol V, Smart J H and Stein T S, 1982 *Physical Review A* **26** 1252

Dale J M, Hulett L D and Pendyala S, 1980 *Surface Science Analysis* **2** 199

Davies S A, 1987 PhD Thesis University College London

Deb N C, Crothers D S F and Fromme D, 1990 *Journal of Physics B: Atomic Molecular and Optical Physics* **23** L483

DeBenedetti S, Cowan C E and Konneker W R, 1949 *Physical Review Letters* **76** 440

Deutsch M, 1951 *Physical Review Letters* **82** 455

Dirac P A M, 1930a *Proceeding of the Royal Society A* **126** 360

Dirac P A M, 1930b *Proceedings of the Cambridge Philosophical Society* **26** 361

Dugdale S B, Alam M A, Fretwell H M, Biasini M and Wilson D, 1994 *Journal of Physics: Condensed Matter* **6** L435

Dupasquier A, 1981 in *POS81* p510

Dupasquier A and Zecca A, 1985 *Rivista Del Nuova Cimento* **8** 2276

Fatuzzo M, Melia F and Rafelski J, 2000 *The Astrophysical Journal* **549** 293

Fulton T and Martin P C, 1954 *Physical Review* **95** 811

Garner A J, Laricchia G and Özen A, 1996 *Journal of Physics B: Atomic Molecular and Optical Physics* **29** 5961

Garner A, 1997 PhD Thesis University College London

Garner A J, Özen A and Laricchia G, 2000 *Journal of Physics B: Atomic Molecular and Optical Physics* **33** 1149

Greaves R G and Surko C M, 1996 *Canadian Journal of Physics* **74** 445

Gullikson E M and Mills A P Jr., 1986 *Physical Review Letters* **57** 376

Hautojärvi P, 1979 *Positron in Solids, Topics in Current Physics No.12* (Springer, Berlin)

Heyland G R, Charlton M, Griffith T C and Wright G L, 1982 *Canadian Journal of Physics* **60** 503

Hodges C H, 1970 *Physical Review Letters* **25** 284

Hoffman, K R, Dababneh M S, Hsieh Y-F, Kaupplia W E, Pol, V, Smart, J H and Stein T S, 1982 *Physical Review A* **25** 1393

Humberston J W, Van Reeth P and Laricchia G, 2001 in *"New Directions in Antimatter Chemistry and Physics"*, eds. C. M. Surko and F. A. Gianturco (Kluwer Academic Publishers) p303

Hutchins S M, Coleman P G, Stone R J and West R N, 1986 *Journal of Physics E: Scientific Instrumentation* **19** 282

Kauppila W E, Stein T S and Jesion G, 1976 *Physical Review Letters* **36** 580

Kauppila W E, Stein T S, Smart J H, Dababneh M S, Ho Y K and Pol V, 1981 *Physical Revoew A* **24** 725

Kauppilla W E and Stein T S, 1990 *Comparison of Positron and Electron Scattering by Gases* Academic Press Inc.

Khatri R, Charlton M, Sferlazzo P, Lynn K G, Mills A P Jr. and Roellig L O, 1990 *Applied Physics Letters* **57** 2374

Khriplovich I B and Yelkhovsky A S, 1990 *Physics Letters B* **246** 520

Kinzer R L, Milne P A, Kurfess J D, Strickman M S, Johnson W N and Purcell W R, 2001 *The Astrophysical Journal* **599** 282

Klemperer O, 1934 *Proceedings of the Cambridge Philosophical Society* **30** 347

Knudsen H and Reading J F, 1992 *Physics Reports* **212** 107

Kögel G, Schodlbauer D, Triftshäuser W and Winter J, 1988 *Physical Review Letters* **60** 1550

Kruit P and Read F H, 1983 *Journal of Physics E: Scientific Instrumentation* **16** 313

Kwan Ch K, Hsieh Y-F, Kauppila W E, Smith S J, Stein T S, Uddin M N and Dababneh M S, 1989 *Physical Review A* **39** 2752

Laricchia G, Charlton M, Davies S A, Beling C D and Griffith T C, 1987 *Journal of Physics B: Atomic Molecular and Optical Physics* **20** L99

Laricchia G, Charlton M, Davies S A and Griffith T C, 1988 *Journal of Physics E: Scientific Instrumentation* **21** 886

Laricchia G and Zafar N, 1992 *Solid State Phenomena* **28 & 29** 347

Laricchia G, 1993 *Positronium Beams and Surfaces* in *Advances with Positron Spectroscopy of Solids and Surfaces* p.401

Laricchia G, 2002 in *"The Physics of Electronic and Atomic Collisions"* (Rinton Press, New York) p329

Laricchia G, Van Reeth P, Szłuińska M and Moxom J, 2002 *Journal of Physics B: Atomic Molecular and Optical Physics* **35** 2525

Laricchia G, Armitage S, Leslie D E, Szłuińska M and Van Reeth P, 2003 *Radiation Physics and Chemistry* **68** 21

Leslie D E, Armitage S and Laricchia G, 2002 *Journal of Physics B: Atomic Molecular and Optical Physics* **35** 4819

Leventhal M, 1992 *American Journal of Physics* **60** 856

Lynn K G, Frieze W E and Schultz P J, 1984 *Physical Review Letters* **52** 1137

Mandal P, Guha S and Sil N, 1979 *Journal of Physics B: Atomic Molecular and Optical Physics* **12** 2913

Marler J P, Sullivan J P and Surko C M, 2005 *Physical Review A* **71** 022701

McAlinden M T and Walters H R J, 1994 *Hyperfine Interactions* **89** 407

McAlinden M T, MacDonald F G R S and Walters H R J, 1996 *Canadian Journal of Physics* **74** 434

Mills A P Jr., Platzman P M and Brown B L, 1978 *Physical Review Letters* **41** 1076

Mills A P Jr., 1983 in "*Positron Solid-State Physics*" eds. Brandt W. and Dupasquier A. (North-Holland) p432

Mills A P Jr. and Gullikson E M, 1986 *Applied Physics Letters* **49** 1121

Mitroy J and Ivanov I A, 2002 *Physical Review A* **65** 012509

Mohorovicic S, 1934 *Astronomische Nachrichten* **235** 94

Moxom J, Laricchia G and Charlton M, 1996 *Journal of Physics B: Atomic Molecular and Optical Physics* **26** L367

Murray C A and Mills A P Jr., 1980 *Solid State Communications* **34** 789

Nagashima Y, Hyodo T, Fujiwara K and Ichimura A, 1998 *Journal of Physics B: Atomic Molecular and Optical Physics* **31** 329

Ott B, 2003 *Contemporary Physics* **44** 1

Özen A, Garner A J and Laricchia G, 2000 *Nuclear Instruments and Methods in Physics Research B* **171** 172

Özen A, 2000 PhD Thesis University College London

Palathingal J C, Asoka-Kumar P, Lynn K G, Posada Y and Wu X Y, 1991 *Physical Review Letters* **67** 3491

Paludan K, Laricchia G, Ashley P, Kara V, Moxom J, Bluhme H, Knudsen H, Mikkelsen U, Møller S P, Uggerhøj E and Morenzoni E, 1997 *Journal of Physics B: Atomic Molecular and Optical Physics* **30** L581

Perkins A and Carbotte J P, 1970 *Physical Review* **1** 101

Petkov M P, Lynn K G, Roellig L O and Troev T D, 1997 *Applied Surface Science* **116** 13

Raith W, 1997 in *'Photonic, Electronic and Atomic Collisions'* eds. F Aumayr and H Winter (World Scientific) p.341

Ramsauer C, 1921 *Annalen der Physik* (Leipzig) **64** 513

Ramsauer C, 1923 *Annalen der Physik* (Leipzig) **72** 345

Ramsauer C and Kollath R., 1929 *Annalen der Physik* (Leipzig) **3** 536

Ray H, 2002 *Journal of Physics B: Atomic Molecular and Optical Physics* **35** 3365

Ruark A E, 1945 *Physical Review Letters* **68** 278

Saito F, Nagashima Y, Hyodo T, 2003 *Journal of Physics B: Atomic Molecular and Optical Physics* **36** 4191

Sarkadi L, 2003 *Physical Review A* **68** 032706

Schultz P J and Lynn K G, 1988 *Reviews of Modern Physics* **60** 701

Shearer J W and Deutsch M, 1949 *Physical Review* **76** 462

Skalsey M, Engbrecht J J, Bitchell R K, Vallery R S and Gidley D W, 1998 *Physical Review Letters* **80** 3237

Skalsey M, Engbrecht J J, Nakamura C M, Vallery R S, Gidley D W, 2003 *Physical Review A* **61** 022504

Sorokin A A, Beigman I L, Bobashev S V, Richter A and Vainshtein L A, 2004 *Journal of Physics B: Atomic Molecular and Optical Physics* **37** 3215

Starrett C, McAlinden M T and Walters H R J, 2005 in press

Stein T S, Kauppila W E, Pol V, Smart J H and Jesion G 1978 *Physical Review A* **17** 1600

Stein T S, Dababneh M S, Kauppila W E, Kwan Ch K and Wan Y J, 1987 in *'Atomic Physics with Positrons'* eds. Humberston J W and Armour E A G (Plenum Press) **169** 251

Sueoka O and Mori S, 1986 *Journal of Physics B: Atomic Molecular and Optical Physics* **19** 4035

Szłuińska M, Van Reeth P and Laricchia G, 2002 *Nuclear Instruments and Methods in Physics Research B* **192** 215

Tong B Y, 1972 *Physical Review B* **5** 1436

Townsend J S and Bailey V A, 1922 *Philosophical Magazine* **43** 593

Van Reeth P, Humberston J W, Laricchia G and Dunn J T, 2000 *Journal of Physics B: Atomic Molecular and Optical Physics* **33** L669

Venables J A and Smith B L, 1977 in *'Rare Gas Solids'* (Academic Press) chapter 10

West R N, 1973 *Advances in Physics* **22** 263

Weyl H, 1931 *Gruppentheorie und Quantenmechanik 2nd Edition* 234

Wheeler J A, 1946 *Ann. N Y Acad. Sci.* **48** 219

Yang C N, 1950 *Physical Review* **77** 242

Zafar N, Laricchia G, Charlton M, Griffith T C, 1991 *Journal of Physics B: Atomic Molecular and Optical Physics* **24** 4661

Zhou S, Li H, Kauppila W E, Kwan C K and Stein T S, 1997 *Physical Review A* **55** 361

Appendix A

Full fitting equation for the determination of |W|+C

As stated in chapter 3, the channel in a time-of-flight spectrum at which the positron peak appears, $ch_+(E)$, is given by:

$$ch_+(E) = ch_0 - t_+(E)/t_{ch}, \qquad A.1$$

where ch_0 is the channel at which the time-zero (t_0) occurs and $t_+(E)$ is the time between the CEMA1 and CEMA2 pulses, which may be expressed as:

$$t_+(E) = t_c - t_{e^-} + t_{e^+} + t_r . \qquad A.2$$

These times are defined schematically in Figure 3.2 and are defined mathematically in turn below.

t_c is the time taken for a positron of constant velocity ($v_{e+} = \sqrt{2E_+/m}$, m is the mass of the positron) to travel from the earth grid of the CEMA1 configuration to R1, the distance between the two represented by D and, therefore:

$$t_c = \left(\frac{m}{2eE_+}\right)^{1/2} D, \qquad A.3$$

where the positron kinetic energy, E_+, is given by the remoderator potential, V_M and the workfunction and contact potential, $|W|+C$ such that:

$$E_+ = eV_M + |W| + C . \qquad A.4$$

The time for secondary electrons released by positron impact at CEMA1 to be accelerated to the plates is given by:

$$t_{e^-} = d_1\left(\frac{2m}{e}\right)^{1/2} \Delta V^{-1/2} , \qquad A.5$$

where d_1 is the separation of the remoderator and channel plates and ΔV is the potential difference between them. The time for a remoderated positron to be accelerated to the earth grid of the CEMA1 configuration is:

$$t_{e+} = d_2\left(\frac{2m}{e}\right)^{1/2} \frac{\left((V_M + |W| + C)^{1/2} - (|W| + C)^{1/2}\right)}{V_M} , \qquad A.6$$

where d_2 is the distance between the remoderator and earth grid.

t_r is the time taken for positrons to be accelerated through the grids in front of CEMA2 and is given by:

$$t_r = t_{R1} - t_{R2} - t_{R3}. \qquad A.7$$

Here, t_{R1} is the time taken for a positron to be accelerated from R1 to R2. The potentials applied to these grids are given by V_{R1} and V_{R2}, respectively and the potential difference, by $\Delta V_{1,2}$. The distance between the two grids is given by d_3, and therefore:

$$t_{R1} = \frac{d_3}{\Delta V_{1,2}}\left(\frac{2m}{e}\right)^{1/2}\left((V_M + |W| + C + V_{R2})^{1/2} - (V_M + |W| + C + V_{R1})^{1/2}\right). \qquad A.8$$

Similarly, the time taken to be accelerated from R2 to R3 (V_{R2} and V_{R3}, respectively) may be written in terms of the potential difference between the grids $\Delta V_{2,3}$ and their separation d_4, i.e.:

$$t_{R2} = \frac{d_4}{\Delta V_{2,3}}\left(\frac{2m}{e}\right)^{1/2}\left((V_M + |W| + C + V_{R3})^{1/2} - (V_M + |W| + C + V_{R2})^{1/2}\right). \qquad A.9$$

Finally, the time taken for a positron to be accelerated from R3 and the front of the channel plates at CEMA2 (V_{R3} and V_F, respectively) is given by:

$$t_{R3} = \frac{d_5}{\Delta V_{3,F}}\left(\frac{2m}{e}\right)^{1/2}\left((V_M + |W| + C + V_F)^{1/2} - (V_M + |W| + C + V_{R3})^{1/2}\right), \qquad A.10$$

where $\Delta V_{3,F}$ is the potential difference between them and their separation is given by d_5.

Appendix B

Published Works

Armitage S, Leslie D E, Garner A J and Laricchia G, 2002 'Fragmentation of Positronium in Collision with He Atoms' *Physical Review Letters* **89** 173402-1

Leslie D E, Armitage S and Laricchia G, 2002 'Production of collimated positronium from molecular nitrogen' *Journal of Physics B: Atomic Molecular and Optical Physics* **35** 4819

Laricchia G, Armitage S, Leslie D E, Szłuińska M and Van Reeth P, 2003 'Positron and positronium interactions with atoms and molecules' *Radiation Physics and Chemistry* **68** 21

Laricchia G, Armitage S and Leslie D E, 2004 'Positronium induced collisions' *Nuclear Instruments and Methods in Physics Research B* **221** 60

Armitage S, Beale J, Leslie D E and Laricchia G, 2005 'Production and scattering of a positronium beam' *Nuclear Instruments and Methods in Physics Research B* **233** 88

Fragmentation of Positronium in Collision with He Atoms

S. Armitage, D. E. Leslie, A. J. Garner, and G. Laricchia*
Department of Physics and Astronomy, University College London, Gower Street, London, WCIE 6BT

 0031-9007/02/89(17)/173402(4)$20.00

173402-2

173402-3

173402-4

INSTITUTE OF PHYSICS PUBLISHING JOURNAL OF PHYSICS B: ATOMIC, MOLECULAR AND OPTICAL PHYSICS

J. Phys. B: At. Mol. Opt. Phys. 35 (2002) 4819–4827 PII: S0953-4075(02)38926-0

Production of collimated positronium from molecular nitrogen

D E Leslie, S Armitage and G Laricchia[1]

0953-4075/02/234819+09$30.00

PERGAMON

Available online at www.sciencedirect.com

SCIENCE DIRECT®

Radiation Physics and Chemistry 68 (2003) 21–31

Radiation Physics and Chemistry

www.elsevier.com/locate/radphyschem

Positron and positronium interactions with atoms and molecules

G. Laricchia*, S. Armitage, D.E. Leslie, M. Szłuińska, P. Van Reeth

0969-806X/03/$ - see front matter
doi:10.1016/S0969-806X(03)00248-2

Available online at www.sciencedirect.com
SCIENCE DIRECT®
Nuclear Instruments and Methods in Physics Research B 221 (2004) 60–68
NIM B
Beam Interactions with Materials & Atoms
www.elsevier.com/locate/nimb

Positronium induced collisions

G. Laricchia *, S. Armitage, D.E. Leslie

doi:10.1016/j.nimb.2004.03.032

Available online at www.sciencedirect.com
SCIENCE DIRECT®
Nuclear Instruments and Methods in Physics Research B 233 (2005) 88–94
NIM B
Beam Interactions with Materials & Atoms
www.elsevier.com/locate/nimb

Production and scattering of a positronium beam

S. Armitage, J. Beale, D. Leslie, G. Laricchia *

0168-583X/$ - see front matter © 2005 Published by Elsevier B.V.
doi:10.1016/j.nimb.2005.03.090